

GEOLOGICA ULTRAIECTINA

Mededelingen van het  
Instituut voor Aardwetenschappen der  
Rijksuniversiteit te Utrecht

No. 52

EVIDENCE FOR SMALL SCALE STRUCTURE  
OF THE UPPER MANTLE

HANNEKE PAULSSEN

GEOLOGICA ULTRAIECTINA

Mededelingen van het  
Instituut voor Aardwetenschappen der  
Rijksuniversiteit te Utrecht

No. 52

EVIDENCE FOR SMALL SCALE STRUCTURE  
OF THE UPPER MANTLE

HANNEKE PAULSSEN

X. X. 20

ISBN: 90-9002211-2

**EVIDENCE FOR SMALL SCALE STRUCTURE  
OF THE UPPER MANTLE**

**EVIDENTIE VOOR KLEINSCHALIGE STRUCTUUR  
VAN DE BOVENMANTEL**

(met een samenvatting in het Nederlands)

**PROEFSCHRIFT**

**TER VERKRIJGING VAN DE GRAAD VAN DOCTOR AAN  
DE RIJKSUNIVERSITEIT TE UTRECHT OP GEZAG VAN  
DE RECTOR MAGNIFICUS PROF. DR. J.A. VAN GINKEL  
VOLGENS BESLUIT VAN HET COLLEGE VAN DEKANEN  
IN HET OPENBAAR TE VERDEDIGEN OP MAANDAG  
13 JUNI 1988 DES NAMIDDAGS TE 2.30 UUR**

**DOOR**

**JOHANNA ANTOINETTE MARIA PAULSSEN**

**GEBOREN OP 16 JANUARI 1958 TE ROTTERDAM**

PROMOTOR: PROF. DR. A.M.H. NOLET

*Aan mijn ouders*

*“Explain all that,” said the Mock Turtle.  
“No, no! The adventures first,” said the Gryphon in an impatient tone:  
“explanations take such a dreadful time.”*

*From: Alice’s Adventures in Wonderland by Lewis Carroll.*

*The research described in this  
thesis was carried out at the:*

*Department of Theoretical Geophysics,  
Institute of Earth Sciences,  
University of Utrecht,  
Budapestlaan 4, P.O. Box 80.021,  
3508 TA Utrecht,  
The Netherlands.*

# Contents

## Chapter 1

Introduction and summary .....	9
References .....	11

## Chapter 2

The NARS array .....	13
2.1 The NARS system response .....	13
2.2 Station configuration and operation of the network .....	15
2.3 Adequacy of broad-band seismograms for body wave studies .....	17
References .....	19

## Chapter 3

The WKBJ method .....	21
3.1 WKBJ theory .....	21
3.2 The WKBJ seismogram .....	23
3.3 Examples .....	28
3.4 Conclusions .....	34
References .....	34

## Chapter 4

Lateral heterogeneity of Europe's upper mantle .....	35
4.1 Introduction .....	35
4.2 Data .....	36
4.3 Method .....	38
4.4 The influence of source parameters in studies of body-wave modelling .....	40
4.5 Determination of the S-wave velocity structure .....	42
4.6 Determination of the P-wave velocity structure .....	52
4.7 Conclusion .....	61
References .....	61

## Chapter 5

Seismological evidence on the upper mantle discontinuities .....	65
5.1 An overview .....	65
5.1.1 Travel time and waveform analyses .....	66
5.1.2 Reflected and converted phases .....	66
5.2 Evidence for a sharp 670-km discontinuity .....	68
5.2.1 Introduction .....	69



## Contents

5.2.2 Data selection and method of analysis .....	71
5.2.3 Observations of P-to-S converted phases from the 670-km discontinuity .....	73
5.2.4 Observations of P-to-S converted phases from the 400-km discontinuity .....	84
5.2.5 Interpretation .....	85
5.2.6 Discussion .....	88
References .....	89
 <i>Chapter 6</i>	
The upper mantle .....	93
6.1 Petrology of the upper mantle .....	93
6.1.1 Important phase transformations .....	93
6.1.2 Are the upper and lower mantle chemically distinct? .....	94
6.1.3 Compositional models of the upper mantle .....	96
6.2 Geodynamics of the upper mantle .....	98
6.2.1 Whole-mantle or layered convection? .....	98
6.2.2 Geodynamical models of the upper mantle .....	102
6.3 In conclusion .....	103
References .....	104
 <i>Samenvatting</i> .....	
<i>Acknowledgements</i> .....	107
<i>Curriculum Vitae</i> .....	108
	109

## Chapter 1

### Introduction and summary

Seismological research has provided a major contribution to our present knowledge of the structure of the Earth. In the 1930's, the radially symmetric seismic velocity distribution was established, showing regions of different seismic character (crust, upper mantle, transition zone, lower mantle, inner and outer core). The interpretation of the seismological findings in terms of the compositional, thermal, and geodynamical constitution of the Earth has, since then, been an important subject in solid Earth geophysics. Presently, there are still major outstanding questions in this field that require high resolution seismological data for their solution. The research of this thesis must be seen in this context: it addresses two aspects that concern the detailed structure of the upper mantle. One is related to the fine structure of the sharp seismic velocity increases ('discontinuities') at depths of about 400 and 670 km, marking the upper and lower boundary of the transition zone. The other concerns the degree of lateral (seismic velocity) heterogeneity in the upper mantle. In the following, a brief outline is presented of the discussion about the nature of the upper mantle discontinuities, and of several aspects associated with upper mantle lateral heterogeneity.

A change in gradient of the first arrival travel time curve near 20° led to the discovery of the 20°, or 400-km discontinuity. After the first seismological observations of this 20° discontinuity, the transition was explained by a phase transformation (see Nolet & Wortel, 1988, for a brief review). Although chemical changes in the transition region have been proposed more often (e.g. Anderson, 1968; Press, 1968), the first more detailed interpretation of the 400-km discontinuity as being of chemical nature was made by Bass & Anderson (1984) and Anderson & Bass (1984). They suggested that this boundary marks the transition from olivine-rich material (pyrolite) to more eclogite-rich material (piclogite). This latter composition would better fit the seismic velocities in the transition zone and the sharpness of the 400-km discontinuity, but their arguments have been disputed by others. Weidner (1985) and Bina & Wood (1987) showed that the olivine- $\beta$ -spinel phase

transformation in a pyrolytic composition could explain the seismic observations, and that a chemical change at a depth of about 400 km need not be invoked.

First evidence for the presence of the 670-km discontinuity was obtained in the 1960's (e.g. Niazi & Anderson, 1965; Johnson, 1967; Green & Hales, 1968). Since then, seismic observations of refracted and reflected phases at this boundary have increased substantially, but, as with the 400-km discontinuity, there is still a debate about its nature. Experimental studies have shown that phase transformations in systems of the two most abundant constituents of the mantle, olivine and pyroxene, occur at pressure and temperature conditions similar to those in the Earth at a depth of about 650 km (e.g. Liu, 1977; Yagi et al., 1979). These results seem to point to a phase transition interpretation. However, the sharpness of this discontinuity, as suggested by seismological studies, would favour the hypothesis of a chemical boundary.

As is clear from the foregoing, there is presently no general agreement about the nature of the two upper mantle discontinuities.

Since the late 1960's, it is well established that there are regional variations in the upper mantle structure. Surface wave studies, in particular, have provided a significant contribution to this knowledge, as Knopoff (1972) showed that a tectonic regionalization could be made on the basis of the dispersion of surface waves. In more recent surface wave studies, advanced processing techniques are employed to optimize the seismic velocity information acquired from the data. The NARS array in western Europe (chapter 2) has provided suitable data for several of such investigations. Using higher mode surface waves, Dost (1987) determined the shear wave velocity and density distribution of the western European Platform and Scandinavian Shield, and showed that these regions have different shear velocities to a depth of 400 km. Nolet & Scheffers (1988) used nonlinear waveform fitting of higher modes surface waves to find deep lateral variations under the NARS array itself. Snieder (1987) used scattered and direct surface waves to derive a three-dimensional model of the shear-wave velocity structure to a depth of 200 km beneath Europe.

Lateral variations in the upper mantle structure have also been inferred from body waves. After the first few regional body wave studies it was recognized that the upper mantle seismic velocity distribution varies from region to region (e.g. Archambeau et al., 1969). These regional models present relatively accurate velocity-depth profiles, but do not yield information about the horizontal scale over which the variations occur. Tomography provides a technique to map these lateral variations, and tomographic studies of P delay times, have resulted in three-dimensional representations of the upper mantle (for Europe e.g.: Babuska et al. 1984; Spakman et al., 1988).

All of these results lack, however, the resolution to verify different hypotheses proposed for the structure and evolution of the upper mantle. Ringwood & Irifune (1988) consider the major element composition of the mantle to be uniform on a large scale (>100 km), while differentiation at mid-ocean ridges and subduction at trenches cause medium-

scale heterogeneity (5-100 km). Jordan (1975) assumes that the seismic velocity variations in the upper mantle are essentially correlated with age. Vlaar (1983) considers the implications of subhorizontal subduction of young oceanic lithosphere, which will have its imprint on the local upper mantle structure with expected variations on a length scale of 100 km or less.

It is clear that detailed seismological evidence may contribute to an improved insight into the constitution of the Earth's upper mantle. Chapter 4 and 5 of this thesis present the results of two detailed body wave studies of the upper mantle that address the question of the degree of lateral heterogeneity and the fine structure of the upper mantle discontinuities, respectively. The data used for these studies are for the major part from stations of the NARS array in western Europe. A brief description of this seismic array is given in chapter 2. Another introductory chapter (chapter 3) discusses the merits and shortcomings of the WKBJ-technique (Chapman, 1978): a method to calculate synthetic seismograms, that has been employed extensively in this thesis.

Chapter 4 describes how the seismic velocity distribution of the upper mantle beneath Europe is investigated by body wave modelling of seismograms from earthquakes in the eastern Mediterranean recorded by stations of the NARS array. It is shown that the gross seismic velocity structure of the subcontinental European mantle can be described by a high velocity lid, a low velocity zone, and discontinuities at depths of about 420 and 650 km. The data, however, also present evidence for distinct small scale lateral heterogeneity to a depth of about 400 km, indicating that the upper mantle of this area may be less homogeneous than was generally assumed.

Evidence for a locally sharp 670-km discontinuity is inferred from waves that have undergone wavetype conversion at the upper mantle discontinuities. Chapter 5 presents the results of this study of P-to-S converted waves, for which not only NARS data have been used, but also short-period seismograms from the RSTN network in the United States. The results of this study may imply that the upper and lower mantle are chemically distinct.

In the last chapter of this thesis (chapter 6) an overview is given of our insights into the upper mantle structure. The implications of the seismological results are presented in the light of evidence from other fields and of hypotheses proposed for the upper mantle.

## References

- Anderson, D.L., Chemical inhomogeneity of the mantle, *Earth Planet. Sci. Lett.*, 5, 89-94, 1968.  
Anderson, D.L., and J.D. Bass, Mineralogy and composition of the upper mantle, *Geophys. Res. Lett.*, 11, 637-640, 1984.  
Archambeau, C.B.E., E.A. Flinn, and D.G. Lambert, Fine structure of the upper mantle, *J. Geophys. Res.*, 74, 5825-5865, 1969.  
Babuska, V., J. Plomerova, and J. Sileny, Spatial variations of P residuals and deep structure of the European lithosphere, *Geophys. J. R. astr. Soc.*, 79, 363-383, 1984.

- Bass, J.D., and D.L. Anderson, Composition of the upper mantle: geophysical tests of two petrological models, *Geophys. Res. Lett.*, *11*, 237-240, 1984.
- Bina, C.R., and B.J. Wood, Olivine-spinel transitions: experimental and thermodynamic constraints and implications for the nature of the 400-km discontinuity, *J. Geophys. Res.*, *92*, 4853-4866, 1987.
- Chapman, C.H., A new method for computing synthetic seismograms, *Geophys. J. R. astr. Soc.*, *54*, 481-518, 1978.
- Dost, B., *The NARS array, a seismic experiment in western Europe*, Ph.D. thesis, University of Utrecht, 117 pp., 1987.
- Green, R.W.E., and A.L. Hales, The travel times of P waves to 30° in the central United States and upper mantle structure, *Bull. Seism. Soc. Am.*, *58*, 267-289, 1968.
- Johnson, L.R., Array measurements of P velocities in the upper mantle, *J. Geophys. Res.*, *72*, 6309-6325, 1967.
- Jordan, T.H., The continental tectosphere, *Rev. Geophys. Space Phys.*, *13*, 1-12, 1975.
- Knopoff, L., Observations and inversion of surface-wave dispersion, *Tectonophysics*, *13*, 497-519, 1972.
- Liu, L.-G., Mineralogy and chemistry of the Earth's mantle above 1000 km, *Geophys. J. R. astr. Soc.*, *48*, 53-62, 1977.
- Niazi, M., and D.L. Anderson, Upper mantle structure of western North America from apparent velocities of P waves, *J. Geophys. Res.*, *70*, 4633-4640, 1965.
- Nolet, G., and B. Scheffers, Imaging with teleseismic data, in *Digital seismology and modelling of the lithosphere*, edited by G.F. Panza and G. Nolet, Plenum (in press), 1988.
- Nolet, G., and Wortel M.J.R., Structure of the upper mantle, acc. for publ. in *Encyclopedia of Geophysics*, edited by D. James, Van Nostrand Reinhold, 1988.
- Press, F., Density distribution in the Earth, *Science*, *160*, 1218-1221, 1968.
- Ringwood, A.E., and T. Irifune, Nature of the 650 km discontinuity: implications for mantle dynamics, *Nature*, *331*, 131-136, 1988.
- Snieder, R., *Surface wave scattering theory, with applications to forward and inverse problems in seismology*, Ph.D. thesis, University of Utrecht 175 pp., 1987.
- Spakman, W., M.J.R. Wortel, and N.J. Vlaar, The hellenic subduction zone: a tomographic image and its geodynamic implications, *Geophys. Res. Lett.*, *15*, 60-63, 1988.
- Vlaar, N.J., Thermal anomalies and magmatism due to lithospheric doubling, *Earth Planet. Sci. Lett.*, *65*, 322-330, 1983.
- Weidner, D.J., A Mineral physics test of a pyrolite mantle, *Geophys. Res. Lett.*, *12*, 417-420, 1985.
- Yagi, T., P.M. Bell, and H.-K. Mao, Phase relations in the system MgO-FeO-SiO<sub>2</sub> between 150 and 700 kbar at 1000° C, *Carnegie Inst. Washington Yearbook*, *78*, pp. 614-618, 1979.

## Chapter 2

### The NARS array

The Network of Autonomously Recording Stations (NARS) was primarily developed for dispersion measurements of higher mode surface waves across the western European Platform. However, for the NARS experiment in western Europe (1983-1987), the instruments were not only tuned for the recording of teleseismic surface waves (Dost, 1987), but also for an adequate registration of body waves (data on which this thesis is based).

#### 2.1 NARS SYSTEM RESPONSE

The system design of the NARS stations is displayed in fig. 2.1. The output of a vertical long-period Teledyne Geotech (SL 210) seismometer and two horizontal (SL 220) seismometers undergoes pre-amplification and electronic shaping before it is digitized in the Kinometrics PDR-2 digital event recorder. The internal clock of the PDR-2 is calibrated by a time signal receiver (tuned to the coded time signal emitted by the DCF-77 station in Frankfurt, FRG). The NARS array comprises 14 of these mobile, 3-component, digital seismic stations. The stations record in a triggered mode and write their data on high density cassette tapes.

For the NARS experiment in western Europe (Nolet & Vlaar, 1982; Dost et al., 1984; Nolet et al., 1985) the seismometers were adjusted to an eigenperiod of 12 s, and the shaping filter modified this response to that of a seismometer with a 100 s eigenperiod. The sampling period was set to 0.125 s, and a second-order low-pass Butterworth filter with a corner frequency of 1 Hz (in the event recorder) was applied as anti-alias filter. The NARS instrument response to velocity and the responses of the individual components of this set-up are shown in fig. 2.2. The total response to velocity is approximately flat in the 10 to 1000 mHz frequency band, making it essentially a 'broad-band' station.

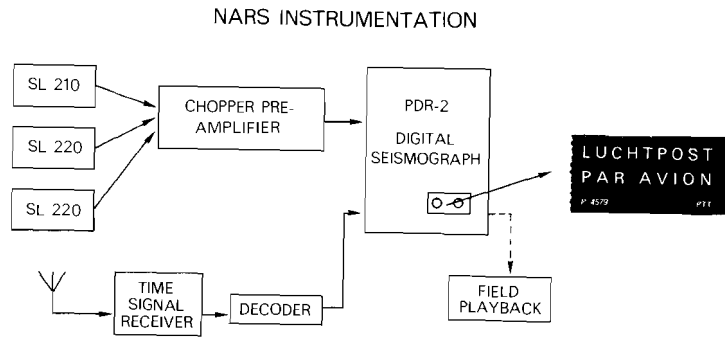


Figure 2.1. The NARS system design

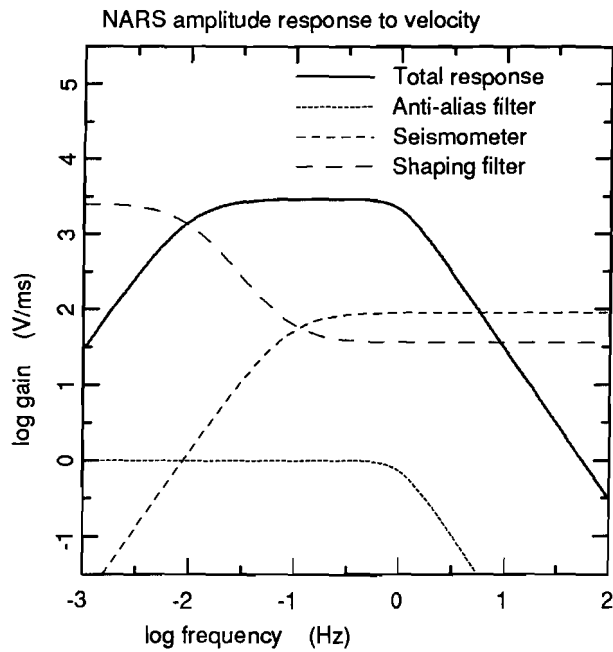


Figure 2.2. Instrument response of the NARS stations. The amplitude in V/ms is converted to counts/ms by the factor 104857.6 counts/Volt.

With the Fourier sign convention

$$F(\omega) = \int f(t) e^{i\omega t} d\omega$$

the transfer function to displacement is given by (Dost et al., 1984)

$$T(\omega) = \frac{-i A \omega^3}{D(\omega)}$$

The denominator  $D$  can be expressed as

$$D(\omega) = (-\omega^2 - 2i\omega\omega_s h_s + \omega_s^2) (-\omega^2 - 2i\omega\omega_a h_a + \omega_a^2)$$

with

$$\omega_s = 2\pi/100 \quad (\text{rad/s})$$

$$\omega_a = 2\pi \quad (\text{rad/s})$$

$$h_s = 1.0$$

$$h_a = 0.707$$

$$A = 1.23 \times 10^{10} \quad (\text{counts/ms})$$

Alternatively, the transfer function can be described in the form of a 4-pole recursive filter where

$$D(\omega) = (\omega + \omega_1)(\omega + \omega_2)(\omega + \omega_3)(\omega + \omega_4)$$

with poles

$$\omega_1 = 4.443 + 4.443i \quad (\text{rad/s})$$

$$\omega_2 = -4.443 + 4.443i \quad (\text{rad/s})$$

$$\omega_3 = 0.0628i \quad (\text{rad/s})$$

$$\omega_4 = 0.0628i \quad (\text{rad/s})$$

## 2.2 STATION CONFIGURATION AND OPERATION OF THE NETWORK

For the NARS project in western Europe, the stations have been installed in a configuration optimal for (higher-mode) surface wave dispersion measurements from Japanese earthquakes. The stations were therefore located in 6 different countries approximately along a great-circle that passes through the region of high seismic activity near Japan and the station spacing was about 200 km. Although the stations were preferably installed in observatories, the majority of the sites were installed in less well equipped places. In some cases these locations proved to be inadequate, and stations had to be replaced. Figure 2.3 shows the configuration of the NARS array, and table 2.1 presents the coordinates and the period of operation of the stations.



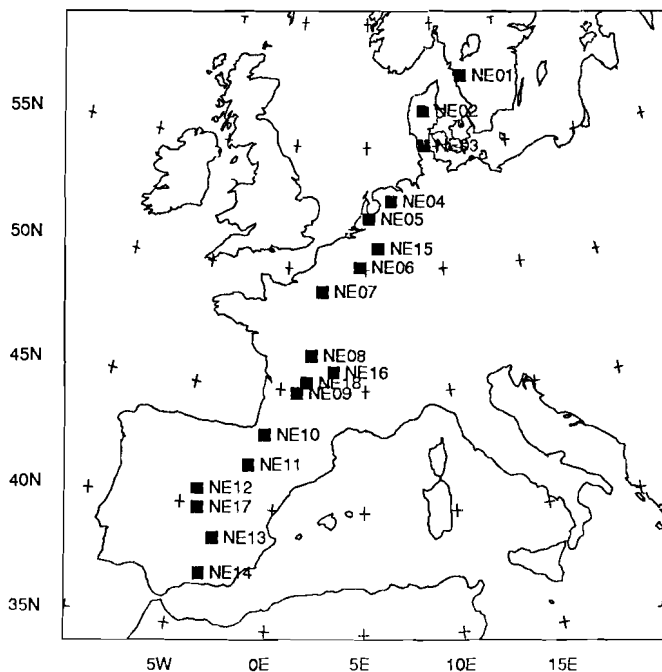
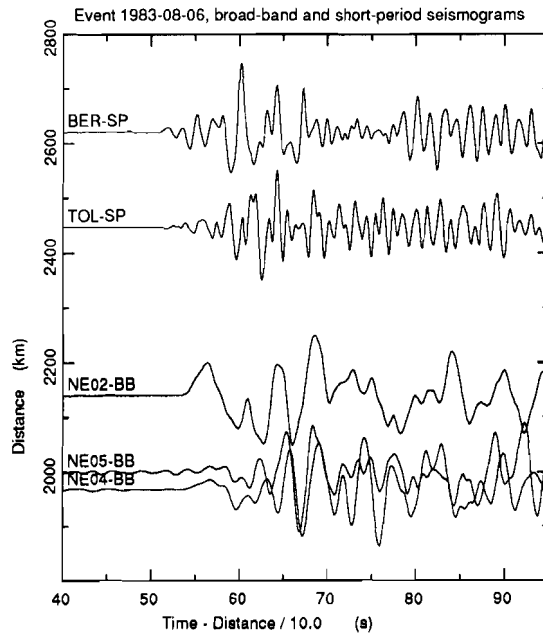


Figure 2.3. NARS station configuration.

Table 2.1: NARS station coordinates.				
Station		Coordinates	Elevation (m)	Period of operation
NE01	Gothenborg	57.801N 12.132E	55.0	Feb. 83 - Jan. 86
NE02	Monsted	56.459N 9.170E	60.0	Feb. 83 - Mar. 87
NE03	Logumkloster	55.045N 9.153E	25.0	Feb. 83 - Mar. 87
NE04	Witteveen	52.813N 6.668E	17.0	Jul. 82 - Feb. 88
NE05	Utrecht	52.088N 5.172E	2.0	Mar. 82 - Feb. 88 <sup>1</sup>
NE06	Dourbes	50.097N 4.595E	225.0	Jul. 82 - Feb. 87
NE07	Villiers-Adam	49.074N 2.232E	70.0	Nov. 83 - Jun. 87
NE08	Aigurande	46.420N 1.730E	360.0	Nov. 82 - Dec. 84
NE09	Les Eyzies	44.852N 0.981E	160.0	Nov. 82 - Feb. 86
NE10	Arette	43.086N 0.699W	480.0	Nov. 82 - May 87
NE11	La Almunia	41.477N 1.372W	370.0	May 83 - Nov. 83
NE11	Ainzon	41.814N 1.517W	440.0	Nov. 83 - Dec. 87
NE12	Valle de los Caidos	40.642N 4.155W	1280.0	May 83 - Feb. 85
NE13	Puertollano	38.685N 4.091W	700.0	May 83
NE14	Granada	37.190N 3.595W	774.0	May 83
NE15	Valkenburg	50.867N 5.785E	100.0	Jun. 84
NE16	Clermont Ferrand	45.763N 3.103E	80.0	Nov. 84 - Jun. 87
NE17	Toledo	39.881N 4.049W	480.0	Feb. 85
NE18	Rejaudoux	45.304N 1.516E	410.0	Feb. 86 - Jun. 87

<sup>1</sup> Station closed between Jun. 1984 and Jan. 1986

The task of the local station managers (mostly volunteers) primarily consisted of



*Figure 2.4.* Broad-band NARS, and short-period DWSSN P-wave arrivals on the vertical component of an event in the Aegean Sea (Date: 1983-08-06,  $T_0$ : 15:43:51.9, Coord: 40.14N, 24.74E, Depth: 2 km,  $m_b$ : 6.0).

changing cassette tapes at least once every two weeks and checking the operation of the station. The cassette tapes were sent to Utrecht, where the data were processed and converted to a format consistent with that of the GDSN (Global Digital Seismograph Network) event tapes.

### 2.3 ADEQUACY OF BROAD-BAND SEISMOGRAMS FOR BODY WAVE STUDIES

This thesis presents the results of two types body wave studies of the upper mantle. I found that the broad frequency response of the instruments was ideally suited for these purposes, enabling P and S phases to be modelled using the same data set (chapter 4), and yielding high-frequency information from the upper mantle discontinuities (chapter 5) that would not be available from conventional long-period instruments.

For the study of the upper mantle seismic velocity structure beneath Europe seismograms have been used with epicentral distances in the range of  $15^\circ$  to  $25^\circ$ . In this

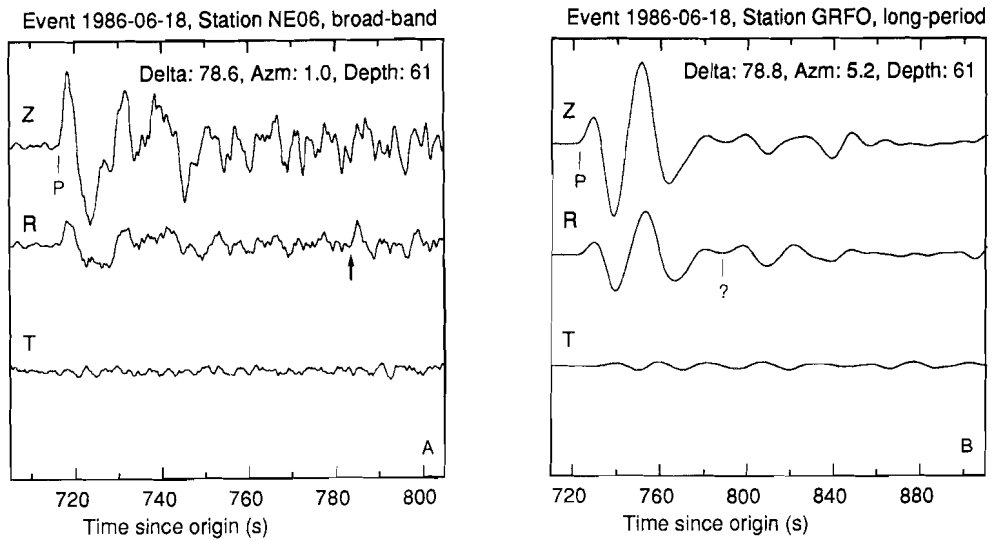


*Figure 2.5.* Broad-band (a) and long-period (b) seismograms of an event from the Aleutian Islands (Date: 1986-06-18,  $T_0$ : 08:05:16.0, Coord.: 51.66N 176.96W, Depth: 61 km,  $m_b$ : 5.7). The three components are marked by Z (vertical), R (radial) and T (transverse). The epicentral distance and backward azimuth to the stations NE06 (a), and GRFO (b) are given in the figures. Indicated with the arrow in (a) is a possible P-to-S converted phase from the 670-km discontinuity; the corresponding location has been indicated by the question mark in figure (b).

distance range, multiple arrivals from the low velocity zone and sharp velocity gradients beneath it produce a complex signal. Identification of the different arrivals is necessary to obtain at least the travel time information of the phases. In chapter 4 (section 2, see fig. 3) it is shown that an unambiguous interpretation of the S-wave arrivals is not possible on the basis of long-period seismograms, and Ingate et al. (1986) demonstrated that this hampers a detailed interpretation in terms of the upper mantle velocity structure. On the other hand, one might try to model the (higher-frequency) P phases using short-period seismograms (maximum amplification at 1 Hz). Figure 2.4 shows the P-wave arrivals on the vertical component of two short-period and three broad-band (NARS) stations. The data are for the same event as for the (S-wave) example shown in chapter 4 (fig. 3; P phases have not been recorded by station NE12, which is located near to station TOL, because triggering occurred on the S-wave arrivals). It is clear from fig. 2.4 that the long-period energy is absent on the short-period seismograms. Furthermore, these data show more 'ringing' with a dominant period of about 1.5 s. This is probably due to shallow crustal reverberations and wavetype conversions at the near-receiver structure. This high-frequency signal tends to mask the upper mantle arrivals; low-pass filtering might in this case facilitate the interpretation by enhancement the low-frequency content.

Fig 2.5 has been included to show the difference between the broad-band and long-period seismograms for the interpretation of P-to-S converted phases from the upper mantle. Note the difference in time scale between fig. (a) and (b) by a factor of 2. The arrow in fig. 2.5(a) points to the onset of a possible P-to-S conversion from the 670-km discontinuity on a seismogram of NARS station NE06. Figure (b) shows the long-period seismogram of the same event recorded in station GRFO (with only slightly different epicentral distance and backward azimuth compared to NE06). The question mark indicates the corresponding location for the P-to-S converted phase on the long-period seismogram of GRFO. It is evident that these low-amplitude phases are difficult to identify on long-period seismograms, due to the lack of characteristic high-frequency signal from the source time function. Moreover, when identified, it does not allow a detailed interpretation in terms of the width of the 670-km discontinuity.

In conclusion, many of the inferences that are presented in these thesis, could not have been made if the instrument response of the NARS stations were peaked at a certain dominant frequency.

## References

- Dost, B., *The NARS array, a seismic experiment in western Europe*, Ph.D. thesis, University of Utrecht, 117 pp., 1987.
- Dost, B., A. van Wettum, and G. Nolet, The NARS array, *Geol. Mijnbouw*, 63, 318-386, 1984.
- Ingate, S.F., J. Ha, and K.J. Muirhead, Limitations of waveform modelling of long-period seismograms, *Geophys. J. R. astr. Soc.*, 86, 57-61, 1986.
- Nolet, G., and N.J. Vlaar, The NARS project: probing the Earth's interior with a large seismic antenna, *Terra Cognita*, 2, 17-25, 1982.
- Nolet, G., B. Dost, and H. Paulssen, Intermediate wavelength seismology and the NARS experiment, *Ann. Geophys.*, 4, 305-314, 1985.

## Chapter 3

### The WKBJ method

In the last two decades synthetic seismograms have provided a valuable tool for the interpretation and inversion of seismic data. Many different techniques have been developed to calculate theoretical seismograms in horizontally stratified media, and, more recently, also for laterally inhomogeneous media. For practical reasons, all methods involve approximations. The WKBJ method (Chapman, 1978) is a technique where the high-frequency seismic signal is approximated for a medium consisting of vertically inhomogeneous layers. I have used the method extensively in this thesis, especially in chapter 4, because it efficiently and adequately calculates body wave seismograms for a large number of signals. In some cases, however, the technique introduces errors that are inherent to the approximations involved. This chapter intends to investigate the conditions for its validity and the cases where it breaks down. For a more elaborate description of the WKBJ seismogram method, particularly for the derivation of the elastodynamic solution, one should refer to Chapman (1978), Dey-Sarkar & Chapman (1978), or the review article by Chapman & Orcutt (1985).

#### 3.1 WKBJ THEORY

In its most general sense, the WKB theory provides an approximate solution to a linear differential equation whose highest derivative is multiplied by a small parameter. It is named after Wentzel, Kramer, and Brillouin, who rediscovered the theory and made it accessible for general use. In seismology, it is generally called WKBJ theory, because Jeffreys (but also Rayleigh) contributed to its early development. The WKBJ theory in seismology is concerned with the solution of the wave equation for high frequencies, and in the following, an outline is presented for the solution of a general (2-D) scalar wave equation in the frequency-space domain. Its generalization to the frequency-slowness domain (the WKBJ seismogram) is briefly summarized in the next section.

We start from the 2-D ( $\mathbf{x} = (x, z)^T$ ) scalar wave equation in the frequency domain:

$$\nabla^2 \phi + \omega^2 v^{-2}(z) \phi = 0 \quad (1)$$

The physical meaning of  $\phi$  and  $v(z)$  is not important at this point, but these variables could be interpreted as the pressure and the acoustic velocity, respectively. To find the approximate solutions for equation (1) from WKB theory, it is required that  $\omega$  is large. Trial solutions are of the form

$$\phi(\omega, \mathbf{x}) = \phi_o(\omega) \sum_{n=0}^{\infty} \frac{A^{(n)}(\mathbf{x})}{(-i\omega)^n} e^{i\omega T(\mathbf{x})} \quad (2)$$

Substitution of this expansion in (1) and requiring that the coefficients of terms of order  $\omega^2$  sum to zero yields the eikonal equation

$$(\nabla T)^2 - v^{-2}(z) = 0 \quad (3)$$

We define  $\mathbf{p} = \nabla T$  for real solutions of  $\nabla T$ . The slowness vector,  $\mathbf{p} = (p, q)^T$ , is perpendicular to 'wavefronts' of constant  $t = T(\mathbf{x})$ . The amplitude coefficients  $A^{(n)}(\mathbf{x})$  can be obtained by setting the sum of terms of each power of  $\omega$  equal to zero.

At high frequencies, only the leading term of the WKB asymptotic expansion will be important, giving the *WKB approximation*

$$\phi(\omega, \mathbf{x}) = \phi_o(\omega) A^{(0)}(\mathbf{x}) e^{i\omega T(\mathbf{x})} \quad (4)$$

or in the time domain

$$\phi(t, \mathbf{x}) = A^{(0)}(\mathbf{x}) \phi_o[t - T(\mathbf{x})] \quad (5)$$

the well-known solution from geometrical ray theory for the propagation of a pulse  $\phi_o$  with amplitude variation ('geometrical spreading')  $A^{(0)}(\mathbf{x})$  and travel time  $T(\mathbf{x})$ .

For the two-point boundary value problem, it will be found that often several solutions for  $T(\mathbf{x})$  and  $A^{(n)}(\mathbf{x})$  exist. Therefore, in the zeroth-order WKB approximation, we can write

$$\phi(\omega, \mathbf{x}) = \phi_o(\omega) \sum_{j=1}^{rays} A_j^{(0)}(\mathbf{x}) e^{i\omega T_j(\mathbf{x})} \quad (6)$$

where 'rays' represents the number of solutions.

It is important to note that the zeroth-order approximation is only valid if the velocity distribution is continuous. Or, more generally, in order to determine the  $n$ th term in the asymptotic expansion, it is necessary that the  $n$ th derivative of the model parameter is continuous. Thus, the WKB approximation breaks down if a discontinuity in  $v(z)$  is encountered. The solution is then propagated across the interface using Snell's law and the appropriate reflection and transmission coefficients.

Furthermore, it is essential to understand that we actually have two families of non-decaying solutions, as from equation (3)

$$p^2 + q^2 = v^{-2}(z)$$

or

$$q(p, z) = \pm \sqrt{v^{-2}(z) - p^2} \quad (7)$$

Waves traveling downward ( $q > 0$ ) and waves traveling upward ( $q < 0$ ) are coupled at  $q(p, z) = 0$ , where  $p = v^{-1}(z)$ . However, exactly at the branch point for  $q = 0$ , the turning point of the ray, the WKB expansion breaks down. This problem can mathematically be overcome by connecting the oscillatory behaviour above the turning point (real phase function) to the exponentially decaying behaviour below it (imaginary phase function) by locally applying the Langer approximation (see e.g. Chapman, 1974).

### 3.2 THE WKB SEISMOGRAM

#### GENERALIZATION OF GEOMETRICAL RAY THEORY

The generalization of the geometrical ray theory described in the previous section to the *WKB seismogram* involves an extra Fourier transform of one of the spatial coordinates to the slowness domain. The essential point of the WKB seismogram is the order of the back transformation: the solution in the frequency-slowness domain is first transformed to the time domain before the transformation to the spatial coordinate is applied.

The Fourier transform with respect to the  $x$  coordinate is defined as:

$$\phi(\omega, p, z) = \left[ -\frac{i\omega}{2\pi} \right]^{1/2} \int_{-\infty}^{\infty} \phi(\omega, x, z) e^{-i\omega p x} dx \quad (8a)$$

and the inverse:

$$\phi(\omega, x, z) = \left[ \frac{i\omega}{2\pi} \right]^{1/2} \int_{-\infty}^{\infty} \phi(\omega, p, z) e^{i\omega p x} dp \quad (8b)$$

The zeroth-order term of the WKB asymptotic expansion in the frequency-slowness domain can be written as

$$\phi(\omega, p, z) = \phi_o(\omega) \sum_{j=1}^{rays} A_j^{(0)}(\mathbf{x}) e^{i\omega \tau_j(p, z)} \quad (9)$$

Using the transformation (8a), it can be shown that the phase functions  $T(\mathbf{x})$  of eq. (6) and  $\tau(p, z)$  of eq. (9) for a certain slowness  $p$  are related by (Dey-Sarkar & Chapman, 1978)

$$\tau(p, z) = T(x(p), z) - x(p) p \quad (10)$$

The inverse transform to the time domain can be solved analytically, and the inverse slowness transform then becomes (Dey-Sarkar & Chapman, 1978)

$$\phi(t, \mathbf{x}) = \frac{-1}{\pi\sqrt{2}} \phi_o(t) * \partial_t \operatorname{Im} \left[ \Lambda(t) * \int_{-\infty}^{\infty} A^{(0)}(p, z) \delta(t - \theta(p, \mathbf{x})) dp \right] \quad (11)$$

where

$$\Lambda(t) = \lambda(t) + i \bar{\lambda}(t)$$

with  $\lambda(t) = H(t) t^{-1/2}$  and  $\bar{\lambda}(t) = H(-t) (-t)^{-1/2}$ , the Hilbert transform of  $\lambda(t)$ ,  $H(t)$  the Heaviside function, and

$$\theta(p, \mathbf{x}) = \tau(p, z) + p x$$

Contributions to the integrand of (11) are obtained for  $t = \theta(p, \mathbf{x})$ , giving

$$\phi(t, \mathbf{x}) = \frac{-1}{\pi\sqrt{2}} \phi_o(t) * \partial_t \operatorname{Im} \left[ \Lambda(t) * \sum_{t=\theta} \frac{A^{(0)}(p, z)}{|\partial_p \theta|} \right] \quad (12)$$

For all real  $t = \theta$ , the inverse transform is exact. However, for some slownesses  $p$ ,  $\tau(p, z)$  is complex, producing an exponentially decaying phase term (with a high decay for high  $\omega$ ). In the WKBJ seismogram method the inverse transform is evaluated only over a real  $p$  contour. In practice, the (real) slowness range is limited either by numerical truncation or by complex slowness values. This discontinuous behaviour of the amplitude terms causes end-point errors on the WKBJ seismograms, as will be shown in the next paragraph.

It should be noted that the most important contributions to the solution of eq. (12) are obtained for  $t = \theta$  with  $\partial_p \rightarrow 0$ , while singularities exist for  $\partial_p = 0$ . The physical interpretation of these results as applied to the seismological problem will be discussed in the following section.

#### SOLUTION FOR AN ELASTIC, LAYERED MEDIUM WITH A SOURCE TERM

Expressions (11) and (12) describe the wave propagation through an inhomogeneous medium without discontinuities, the solution of (1). To obtain the solution for more realistic seismological problems, we must calculate the displacement due to a point force in an (isotropic) elastic medium in which discontinuities are present. Solutions can be obtained from the elastic potentials ( $\phi$  in eq. (1) can be interpreted as the P-wave potential:  $\phi = \nabla \cdot \mathbf{u}_p$ , where  $\mathbf{u}_p$  represents the displacement), but when the models contains interfaces it is more convenient to represent and solve for the components of displacement and stress in the form of a vector, the displacement-stress vector. The zeroth-order term of the WKBJ expansion is then obtained in the same way as described in the foregoing, but the solution in terms of the displacement-stress vector involves more 'bookkeeping'. For laterally homogeneous media, we find the well-known results of P waves that propagate with a velocity  $\alpha(z)$  and that have a longitudinal polarization, and S waves, that can be separated into two perpendicular transverse SV and SH components, propagating with a velocity  $\beta(z)$ .



Interfaces are now easily incorporated by including the appropriate reflection and transmission coefficients of the rays. By the requirement of continuity of stress and displacement at each interface, the P and SV components combine to form a coupled system. The introduction of a point force  $\mathbf{f} = \mathbf{f}_o(t) \delta(\mathbf{x} - \mathbf{x}_o)$ , does not present problems in the WKBJ approximation. The solution of the now inhomogeneous wave equation (with a term  $\nabla \cdot \rho^{-1} \mathbf{f}_o$  on the r.h.s. of eq. (1)) is easily obtained at  $\mathbf{x}_o$ , and the general solution is obtained by propagating the solution to the receiver at  $\mathbf{x}$ . A moment tensor instead of a point force as source term is represented as  $\mathbf{m} = \nabla \cdot \mathbf{M}_o(t) \delta(\mathbf{x} - \mathbf{x}_o)$  (Chapman & Orcutt, 1985).

Following this procedure, and expanding the displacements and stresses to vector cylindrical harmonics, Chapman (1978) and Dey-Sarkar & Chapman (1978) showed that (to zeroth order) the WKBJ seismogram for P waves at  $\mathbf{x} = (x, z)^T$  due to an explosive point force is

$$\mathbf{u}(t, \mathbf{x}) = - \frac{\dot{f}(t)}{2^{5/2} x^{1/2} \pi^2 \alpha_o^2} * \text{Im} \left[ \Lambda(t) * \int_{-\infty}^{\infty} \frac{p^{1/2} R(p)}{(\rho \rho_o q q_o)^{1/2}} \begin{bmatrix} q \\ p \end{bmatrix} \delta(t - \theta) dp \right] \quad (13)$$

where  $\mathbf{u}$  represents the displacement,  $\dot{f}(t)$  the time derivative of the point force  $\mathbf{f}(t)$  at  $\mathbf{x}_o = (0, 0)^T$ , and the subscript  $o$  refers to the model parameters at the source.  $R(p)$  is the product of all reflection and transmission coefficients along the ray and includes factors of  $-i \text{sgn}(\omega)$  (zeroth-order Langer approximation) for each turning point. The slowness integral is evaluated at

$$\theta(p, x) = \tau(p) + p x \quad (14)$$

with phase function

$$\tau(p) = \int_{z_o}^z q(p, z') dz' \quad (15)$$

where the integral from  $z_o$  to  $z$  represents the ray integral over  $z$  between source and receiver. The travel time and phase function are related by (analogous to eq. (11))

$$\tau(p) = T(p) - x(p) p \quad (16)$$

The most important contribution to the integral in equation (13), for a slowly varying function  $R(p)$ , is obtained for  $\partial_p \theta(p, x) \rightarrow 0$  (see fig. 3.1(d-e)), or equivalently, for  $\tau'(p) + x \rightarrow 0$  (see fig. 3.1(b)). So, if we define  $X(p) = -\tau'(p)$ , then we obtain saddle points for  $p = p_x$  with  $x = X(p_x)$ . It is easily shown that the travel time function  $T(p_x)$  is equal to the theta function at the saddle point  $p_x$  (as indicated in fig. 3.1(d-e)). To remove the singularities in (13) for each ray geometrical arrival where  $\partial_p \theta = 0$ ,  $t$  is expanded around the saddle point  $p_x$ :

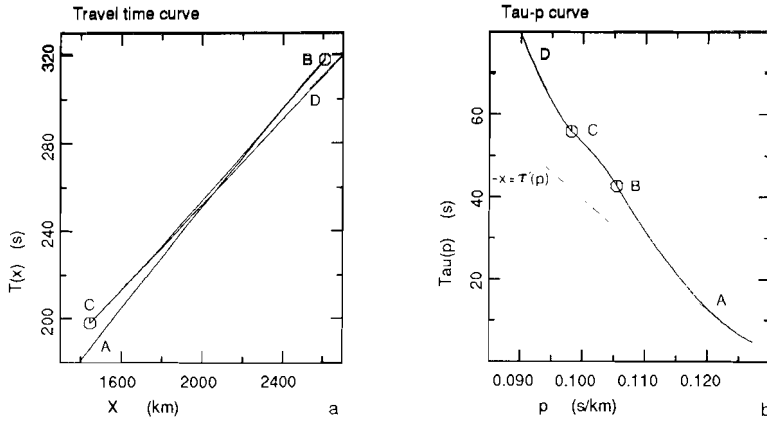


Figure 3.1. Travel time curve (a),  $\tau$ - $p$  curve (b),  $x$ - $p$  curve (c),  $\theta$ - $p$  curves for two different distances (d and e), and raypaths (f) for an upper mantle model with a triplication. The letters A-D indicate different branches or points on the travel time curve (a), and the corresponding points have been indicated on the other diagrams. Fig. (d) shows the  $\theta$ - $p$  curve for the distance at C. The travel times (at  $\partial_p \theta = 0$ ) are indicated by  $T_1$  and  $T_2$ , and the time corresponding to the maximum slowness by  $t_c$ . Fig. (e) shows the  $\theta$ - $p$  curve for a distance of 1805 km. The three ray geometrical travel times are indicated by  $T_1$ - $T_3$  (point C does not coincide with the curve at  $T_2$ ).

$$\begin{aligned}
 t = \theta(p, x) &\approx T(p_x) + 1/2 (p - p_x)^2 \partial_p^2 \theta \\
 &\approx T(p_x) - 1/2 (p - p_x)^2 X'(p_x)
 \end{aligned} \tag{17a}$$

For  $t > T(p_x)$  expression (13) can be evaluated for the two (real) roots  $p_i$  ( $i = 1, 2$ ) on either side of the saddle point, and the argument of the delta function can be approximated by

$$\begin{aligned}
 t - \theta &\approx (p - p_i) \partial_p \theta(p_i, x) \\
 &\approx (p - p_i) [x - X(p_i)]
 \end{aligned} \tag{17b}$$

Both roots contribute half of the geometrical amplitude of the solution at  $t = \theta$ .

#### EXAMPLE TO SHOW THE RELATIONS BETWEEN $p$ , $\tau$ , $X$ , $\theta$ , AND $T$

Figure 3.1 illustrates the relations between the different parameters for a triplication in the travel time curve as shown in (a). The  $\tau$ - $p$  curve (b) is directly calculated from integral (15), and classical ray theory provides the well-known relationship between  $x$  and  $p$  in a spherical or flat layered earth (fig. c). The distance  $X$  for the ray geometrical arrival with a slowness  $p$  can be determined from this diagram as is indicated. Figures (d) and (e) present  $\theta$ - $p$  curves (eq. (14)) for two different values of  $X$ . The travel times  $T_i(p_x)$  for different

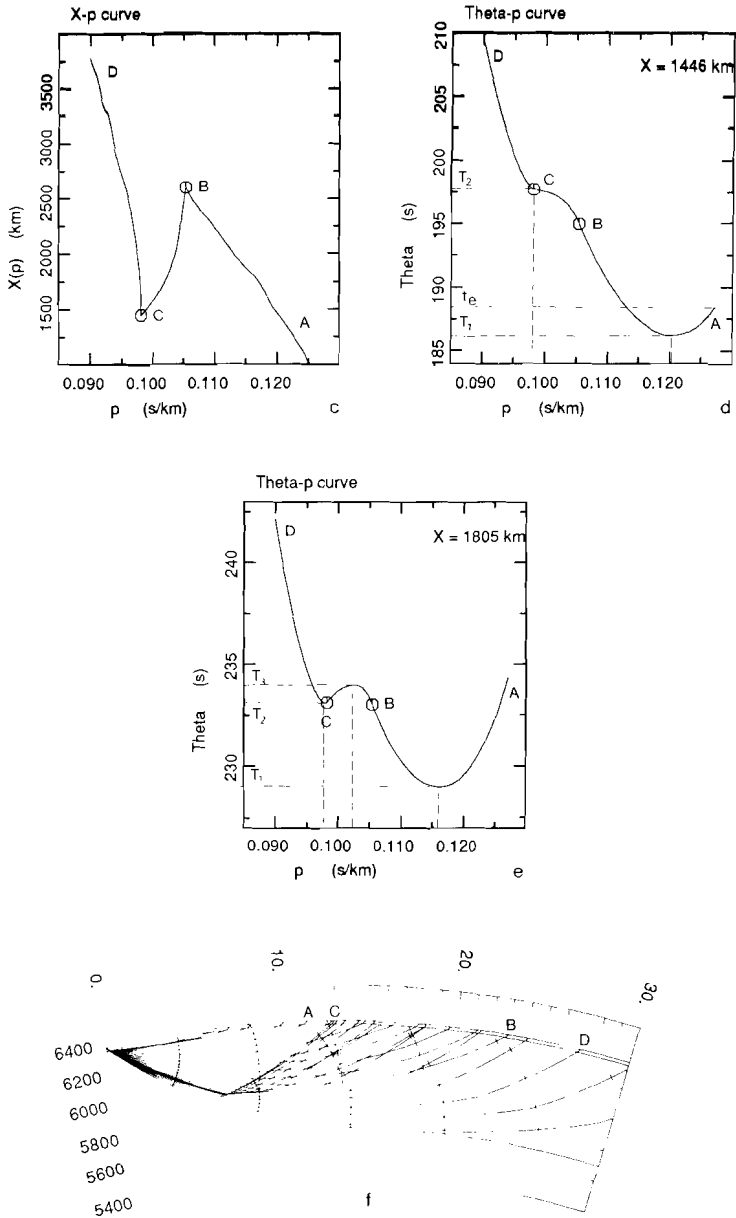


Figure 3.1. (continued)

branches of the travel time curve are indicated in figures (d) and (e). For completeness the raypaths through the model are shown in fig. (f).

## SMOOTHING

A straightforward way to approximate the singularities in expression (13) for the numerical computation of the seismogram is to smooth the signal in the time domain. The program used in chapter 4 convolves the time series with a boxcar window,  $B(t)$ , of length  $2\Delta t$ , where  $\Delta t$  is the sample interval.

$$B(t) = 1/2 [ H(t+1) - H(t-1) ]$$

where  $H(t)$  is the Heaviside function. The smoothed solution becomes

$$\mathbf{u}(t, \mathbf{x}) * \frac{B(t/\Delta t)}{\Delta t} = - \frac{\dot{f}(t)}{2^{5/2} x^{1/2} \pi^2 \alpha_o^2} * \text{Im} \left[ \Lambda(t) * \frac{1}{2\Delta t} \sum_{t=\theta \pm \Delta t} \int \frac{\rho^{1/2} R(p)}{(\rho\rho_o q q_o)^{1/2}} \begin{bmatrix} q \\ p \end{bmatrix} dp \right] \quad (17)$$

Thus, the integral is numerically evaluated over finite (real) slowness intervals corresponding to  $t = \theta(p, \mathbf{x}) \pm \Delta t$ . Smoothing has the important advantage that the results are not sensitive to small features in the model, allowing the model parameters to be linearly interpolated without generating unwanted effects.

## EARTH FLATTENING TRANSFORMATION

Although the WKBJ seismogram approach can be calculated for a medium with spherical symmetry as well as for a flat layered medium, it is convenient to use the same algorithm for both problems. The transformation of the spherical system to a plane layered system involves a simple transformation of the model parameters (see e.g. Aki & Richards, 1980, p. 463-465). It has been shown that this 'earth flattening transformation' is exact for the SH problem, but involves first order errors ( $O(\omega^{-1})$ ) for the P-SV problem; these are of the same order as for the WKBJ approximation.

## 3.3 EXAMPLES

In the previous sections it has been pointed out that the WKBJ seismogram is a zeroth-order, high-frequency approximation, for which the inverse transform is evaluated over a (limited) real  $p$  contour, and that the signal is smoothed in the time domain. The earth flattening transformation does not introduce extra errors to this approximate solution. In this section, the adequacy of the WKBJ method and its shortcomings will be illustrated by synthetic seismograms.

## TURNING RAYS CALCULATED FOR A LIMITED SLOWNESS INTERVAL

The WKBJ method accurately (and economically) calculates synthetic seismograms

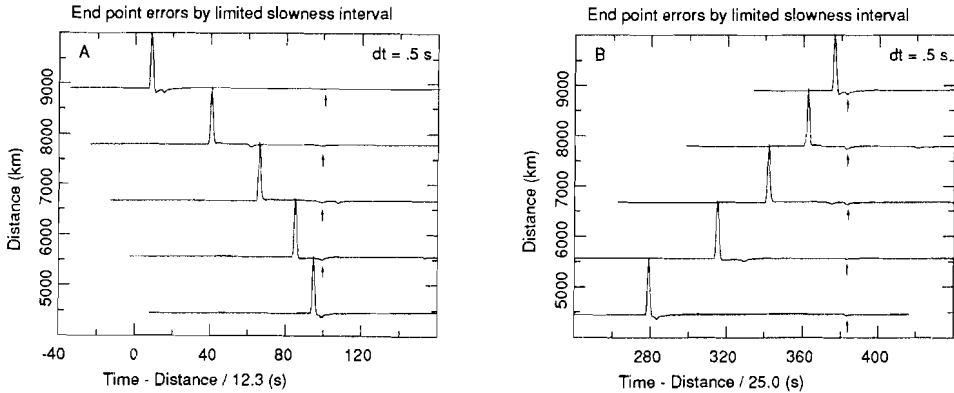


**Figure 3.2.** WKBJ seismograms of direct P phases with turning points in the lower mantle of model 1066B. End-point arrivals due to truncation of the slowness interval are indicated by the arrows, in fig. (a) for the maximum slowness and in fig. (b) for the minimum slowness.

for 'turning' rays. Expression (17) adequately describes the signal at  $t = T(p_x)$ , the time corresponding to the ray geometrical arrival at a distance  $x$ , for a smoothly varying function  $R(p)$ . However, so-called 'end-point arrivals' are also generated due to the evaluation of the slowness integral over a (numerically defined) limited slowness range. The discontinuous behaviour of the integrand in (17) at the end-point slownesses  $p_e$  causes end-point arrivals at

$$t_e = \theta(p_e, x) = T(p_e) + p [x - X(p_e)]$$

It can be shown that the amplitude of these arrivals decays as  $1/|x - X(p_e)|$  from  $X(p_e)$  for  $t_e > T(p_x)$ . Figure 3.2 presents the WKBJ seismograms for turning P waves in the lower mantle of model 1066B (Gilbert & Dziewonski, 1975). The time axes of fig. 3.2 (a) and (b) have been reduced with reduction velocities corresponding to the maximum and minimum slowness of the integrand, which makes the end-point arrivals line up vertically on the diagrams. These end-point errors can be confusing, but, in general, their amplitude is significantly smaller than that of the ray geometrical arrivals. Moreover, if the difference between the ray geometrical slowness and the end-point slowness is sufficiently large, then the end-point phase will arrive outside the time interval of interest. However, there may be cases that its effect is not negligible. A detailed interpretation of the synthetic seismograms can then be misleading if one is not aware of these (predictable) artefacts.

#### TRIPPLICATIONS OF THE TRAVEL TIME CURVE

Model 1066B has been used to compute synthetic seismograms of upper mantle P phases shown in fig. 3.3. The seismograms drawn with solid lines represent the synthetics

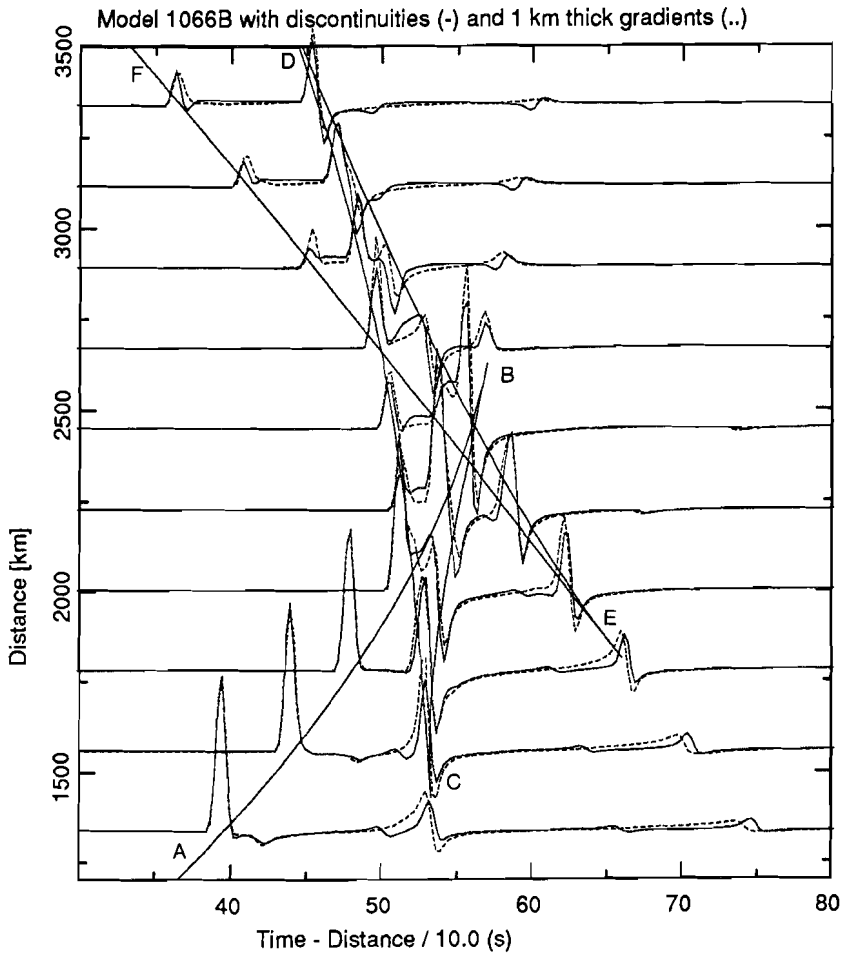


*Figure 3.3.* Synthetic seismograms of upper mantle P phases for model 1066B. The solid line marked with A-F indicates the travel time curve. The other solid lines represent the seismograms for the original model with first order discontinuities. The dashed lines represent the seismograms for the same model where the discontinuities have been replaced by velocity gradients extending over a width of 1 km.

of the original model with discontinuities in the velocity distribution at 420 and 671 km depth ('first order discontinuities'). The dashed lines represent the synthetics for the same model except that the discontinuities have been replaced by velocity gradients extending over a width of 1 km. Thus, for the seismograms computed for the original model it has been necessary to propagate the solution across the interfaces using the appropriate reflection and transmission coefficients, whereas for the 'gradient model' the seismograms could be calculated using the WKBJ approximation only. It is clear that both sets of

seismograms are very similar except for a few features, and these features point to essential aspects of the approximations in the WKBJ seismogram.

It should be noted that, although the WKBJ seismogram is a high-frequency approximation, it does not predict infinite amplitudes at caustics. This is a clear improvement over geometrical ray theory that gives singularities in the amplitudes at the points C and E of the gradient model due to a locally infinite geometrical spreading ( $(dx/dp)^{-1/2} = \infty$ ). However, the WKBJ seismogram does not provide a completely adequate solution for velocity gradients, because it does not model low-frequency reflections from gradient zones. This is inherent to the WKBJ approximation because the frequency and space dependence are separated in the solution. The relative amplitude of the solution at a depth  $z$  depends only on the model parameters at that depth (see, for instance, eq. (9)). Low-frequency reflections from gradient zones are therefore not modelled, even if higher-order terms are included in the solution. A way to overcome this problem practically is to model the gradient zone by a stack of thin layers and calculate the reflections from each interface (and include internally reflected phases for a better approximation). However, this is not an efficient method and preference should be given to an alternative technique (e.g. 'full wave method', Richards, 1973) to model reflected waves from gradient zones adequately at low frequencies. The difference between 'gradient reflections' and (ray theoretical) reflections from a first order discontinuity can be seen in the regions of pre-critical reflections (e.g. at  $x < 1800$  km for the 671-km transition). The amplitude of the pre-critical 'gradient reflection' decays faster than that of the first order discontinuity because of its (larger) geometrical spreading.

Another difference between the two sets of synthetic seismograms is that the diffracted phases from the 420-km discontinuity (the extension from B in the 2600 to 3500 km distance range) have a significantly larger amplitude for the sharp discontinuity than for the 1 km thick gradient. This observation points to one of the most important shortcomings of the WKBJ seismogram method: the interaction of waves with interfaces at finite frequencies is not properly accounted for. The solution for arrivals in the shadow zone is obtained by expanding the function  $\theta$  (eq. (17a)) around the saddle point  $p_d$ , the slowness corresponding to the grazing ray. The amplitude is then half of the geometrical value at the shadow edge, because one of the roots  $p_i$  is imaginary. For arrivals in the (deep) shadow, the WKBJ method just models the effects of Fresnel diffraction (using eq. (17b), yielding an amplitude decay of  $1/|x - X(p_d)|$ ). The method does not model the interaction of the wavefront with the interface at finite frequencies. The amplitudes of diffracted phases in the shadow zone for the model with the sharp discontinuities are therefore too large. Similar effects are expected for waves turning just above an interface, where the zeroth-order Langer approximation (a factor  $-i \operatorname{sgn}(\omega)$ ) is used to model the signal, but wave interaction with the discontinuity is not negligible.

The slightly larger amplitudes of the arrivals for the gradient model on the branch EF (turning phases below the 671-km transition) are most likely due to the fact that more energy is transmitted downward from shallower depths for this model than for the model

with the interfaces. These differences are not due to approximations in the method.

It can be concluded that, when modelling arrivals from a velocity structure with interfaces, one should be aware that amplitudes of diffracted phases are overestimated. A for most purposes less inconvenient shortcoming is that low-frequency energy reflected from gradient zones is not modelled by the WKBJ method.

#### LID AND LOW VELOCITY ZONE

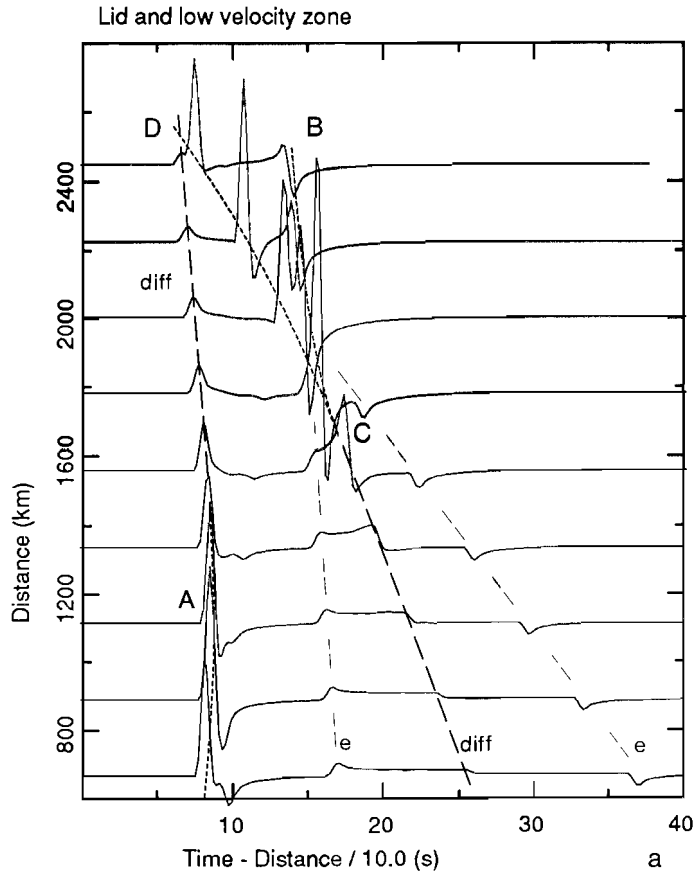


Figure 3.4. (a) Solid lines represent the WKBJ seismograms of P phases of the velocity structure shown in (b). The short dashed lines indicate the travel time curve. The thick long dashed lines mark the diffracted phases, and the thin long dashed lines mark end point arrivals. Fig. (c) shows the raypaths through the model.

Figure 3.4(a) shows the WKBJ seismograms of direct P phases for a model with a low velocity zone. The model and raypaths through the medium are presented in fig. 3.4 (b) and (c), respectively. Ray geometrical arrivals from the high velocity 'lid' (branch A) and



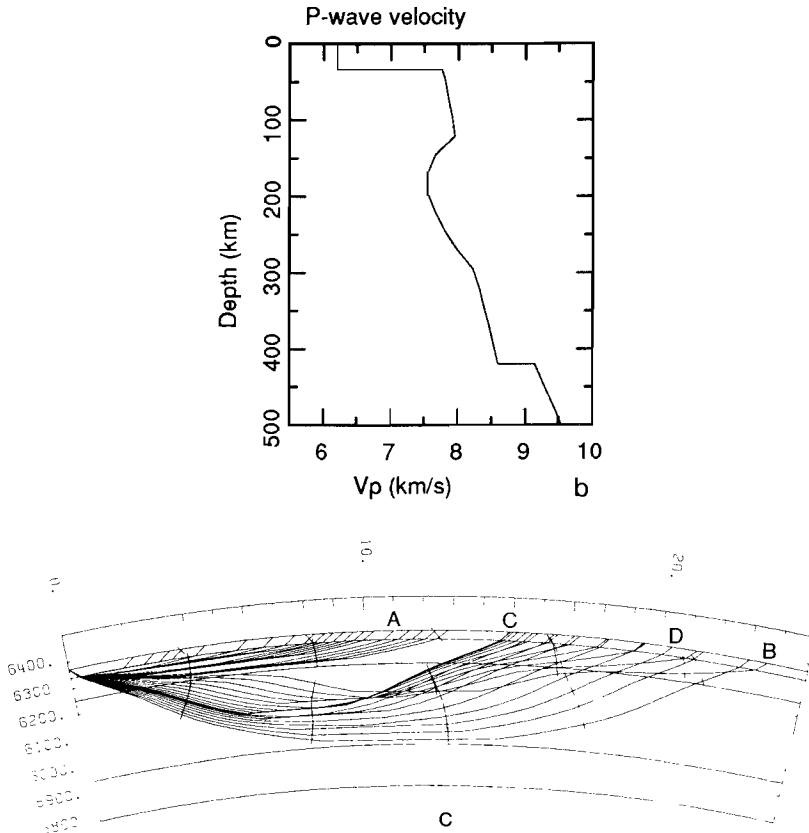


Figure 3.4. (Continued)

from the velocity structure below it (branch BC and CD) are easily recognized on fig. 3.4(a). Diffracted phases in the shadow zone from the caustic at B and from the lid (A) are also clear, whereas end-point arrivals evidently contaminate the signal after the first arrival in the 600-1800 km distance range. It has already been pointed out that the WKBJ method adequately calculates the high-frequency signal at caustics, but only models the effect of Fresnel diffraction in the shadow zone. These aspects have been inferred for the case of a triplication, but the same arguments apply for the shadow of a low velocity zone (at C).

Although it cannot be inferred from the seismograms displayed in fig. 3.4(a), it is expected that the amplitude of the diffracted phase from the base of the lid is too small, since the WKBJ method does not model the tunneling of low frequency energy at the base of the lid. This is, in essence, the same shortcoming as that for gradient zones discussed in the previous example. However, in this case it is not possible to approximate the low-frequency effects by adjusting the model. The WKBJ method is therefore inappropriate for calculating (non-ray-geometrical) signals from a lid-low-velocity structure. These phases

may, however, be important, especially for modelling upper mantle phases for a velocity distribution of a tectonic region (see e.g. chapter 4, fig. 15(a): the  $Pn$  phase at NE02). One should in such cases be aware of the shortcomings of the WKBJ technique, and not try to model these low-frequency arrivals, or use a more adequate technique for these problems.

### 3.4 CONCLUSIONS

Several examples of WKBJ seismograms for structures relevant to the upper mantle have been discussed in the previous section. It was shown that ray geometrical arrivals are properly calculated, but low-frequency effects from velocity gradients and wave interaction with interfaces are not modelled. The adequacy of the method for the majority of the arrivals, combined with the effectiveness of the computations (although not mentioned explicitly) makes this method a suitable technique for 'reconnaissance studies' of waveform data that are inverted to a velocity structure. These aspects, together with the fact that its shortcomings and artefacts are easily predicted, have led to the choice of this technique for the study of the upper mantle beneath Europe as presented in the next chapter. It should be emphasized that the technique has been used in the next chapter mainly as an aid to interpret the multiple upper mantle arrivals and to match their travel times. More detailed (amplitude) modelling is not justified considering the shortcomings of the WKBJ method, particularly for diffracted phases from low velocity zones and discontinuities.

### References

- Aki, K., and P.G. Richards, *Quantitative Seismology: Theory and Methods*, 932 pp., W.H. Freeman, San Francisco, 1980.
- Chapman, C.H., The turning point of elastodynamic waves, *Geophys. J. R. astr. Soc.*, 54, 613-621, 1974.
- Chapman, C.H., A new method for computing synthetic seismograms, *Geophys. J. R. astr. Soc.*, 54, 481-518, 1978.
- Chapman, C.H., and J.A. Orcutt, The computation of body wave synthetic seismograms in laterally homogeneous media, *Rev. of Geophys.*, 23, 105-163, 1985.
- Dey-Sarkar, S.K., and C.H. Chapman, A simple method for the computation of body wave seismograms, *Bull. Seism. Soc. Am.*, 68, 1577-1593, 1978.
- Gilbert, F., and A.M. Dziewonski, An application of normal mode theory to the retrieval of structural parameters and source mechanisms from seismic spectra, *Philos. Trans. R. Soc. London, Ser. A*, 278, 187-269, 1975.
- Richards, P.G., Calculation of body waves for caustics and tunnelling core phases, *Geophys. J. R. astr. Soc.*, 22, 453-472, 1973.

## Chapter 4

# Lateral heterogeneity of Europe's upper mantle

**Summary.** The upper mantle velocity structure beneath Europe is investigated by body-wave modelling of broad-band seismograms from earthquakes in the eastern Mediterranean recorded by stations in north-west Europe. The gross features of the *P*- and *S*-wave velocity distribution as inferred from the data show a high velocity lid, a low velocity zone, and two discontinuities at depths of approximately 420 and 650 km. The seismograms also present evidence for lateral heterogeneity of at least a few per cent (2.5 per cent for *P*, 4 per cent for *S*) to a depth of approximately 400 km. Many of the inferred velocity variations can be related to the tectonic setting of the region between source and receiver. Broad-band seismograms are essential for such detailed study of upper mantle structure using body-wave modelling.

### 1 Introduction

In recent years many studies have been carried out to investigate the lateral heterogeneity of the Earth's upper mantle. The objective is to gain better insight into the geodynamical processes occurring in the mantle and to obtain a better knowledge of its chemical composition. At present, large-scale heterogeneity in the seismic velocities up to a few per cent has been established to depths of about 400 km (e.g. Woodhouse & Dziewonski 1984; Grand & Helmberger 1985). But, in spite of the results produced by various studies, it is still impossible to discriminate between different concepts of the upper mantle such as suggested by Ringwood (1975), Anderson (1979, 1984), Jordan (1978), or Vlaar (1983) (see Nolet, Dost & Paulssen 1986 for a more detailed discussion on this subject). One of the important questions in this respect is to what (small) scale distinct lateral heterogeneity may be present.

Methods which have been used to investigate the upper mantle structure include fundamental and higher mode surface-wave analysis. These data have yielded the gross *S*-wave

This chapter is published as:

Paulssen, H., Lateral heterogeneity of Europe's upper mantle as inferred from modelling of broad-band body waves, *Geophys. J. R. astr. Soc.*, 91, 171-199, 1987.

velocity structure to a few hundred kilometres depth (e.g. Woodhouse & Dziewonski 1984; Nolet 1977; Cara, Nercessian & Nolet 1980; Dost 1986), but lack the resolution on a smaller scale, say less than 1000 km horizontally and 50 km vertically. Tomography, using *P* arrival times, points to lateral variations in the *P*-wave velocity structure in Europe which could be established within a horizontal length scale of 100 km (Spakman 1986a). However, the gradients of the velocity–depth function, and the depths of the discontinuities cannot be determined accurately with tomographic studies. This information is essential for a petrological interpretation of the upper mantle velocity variations. Relatively accurate velocity models are obtained by body-wave analysis of regional data, and many models representing the average upper mantle velocity structure of specific regions have been determined in the last decade (e.g. Burdick 1981; Walck 1984, 1985; Leven 1985). The variations among the models suggest a large degree of lateral heterogeneity, but the horizontal length scale on which this occurs cannot be estimated.

This paper presents the results of a waveform-fit analysis of upper mantle phases with ray-paths in Europe. It is not the first study which adopts the technique of body-wave modelling for a determination of the upper-mantle velocity structure, but there is an important difference with previous studies of this kind: the use of broad-band seismograms. Most previous studies have employed long-period data to infer the average velocity structure of the area (e.g. Helmberger & Engen 1974; Burdick & Helmberger 1978; Lyon-Caen 1986). As Ingate, Ha & Muirhead (1986) have pointed out, there is a severe limitation on the resolution which can be obtained by working with long-period seismograms. Only the gross features of the velocity structure can be resolved. The results of this study show that arrivals from strong velocity gradients and low velocity zones can be identified more accurately on broad-band seismograms, thus enhancing the resolution of the inferred velocity model.

The data which have been analysed are from earthquakes in the eastern Mediterranean recorded by NARS stations in north-west Europe (NARS: Network of Autonomously Recording Seismographs, cf. Nolet & Vlaar 1982, Dost, van Wettum & Nolet 1984). *P*- and *SH*-waveforms are modelled by trial and error using the WKB technique (Chapman 1978) to yield the upper mantle *P*- and *S*-wave velocity structure. The waveform fitting results show that the average velocity structure for the region between south-east and north-west Europe has a high velocity lid, a low velocity zone, and two discontinuities at depths of approximately 420 and 650 km. The data, however, also present evidence for lateral heterogeneity: it is not possible to model the seismograms with a single *P*- or *S*-wave velocity distribution, and different models must be assumed to match the arrival times of the phases on different seismograms. The degree of lateral heterogeneity of the area is roughly estimated by comparison of 1-D models which are thought representative of the average structure along the ray-paths. The results suggest that velocity variations of at least a few per cent to the depth of the 400-km discontinuity are present in the upper mantle beneath central Europe.

At present, it is not possible to perform a 3-D inversion by waveform analysis because of the sparseness of the available data. However, the results of this study indicate that modelling of broad-band seismograms, which are now becoming more widely available, allows a more detailed determination of upper mantle structure.

## 2 Data

The data which have been used in this study are both *P*- and *SH*-waves for events at distances of 15°–25°, recorded by broad-band stations of the NARS array. Events and stations are shown in Fig. 1, and Table 1 presents the event parameters as published by ISC, or PDE when the ISC data were not yet available (event 5-270). All events in the eastern

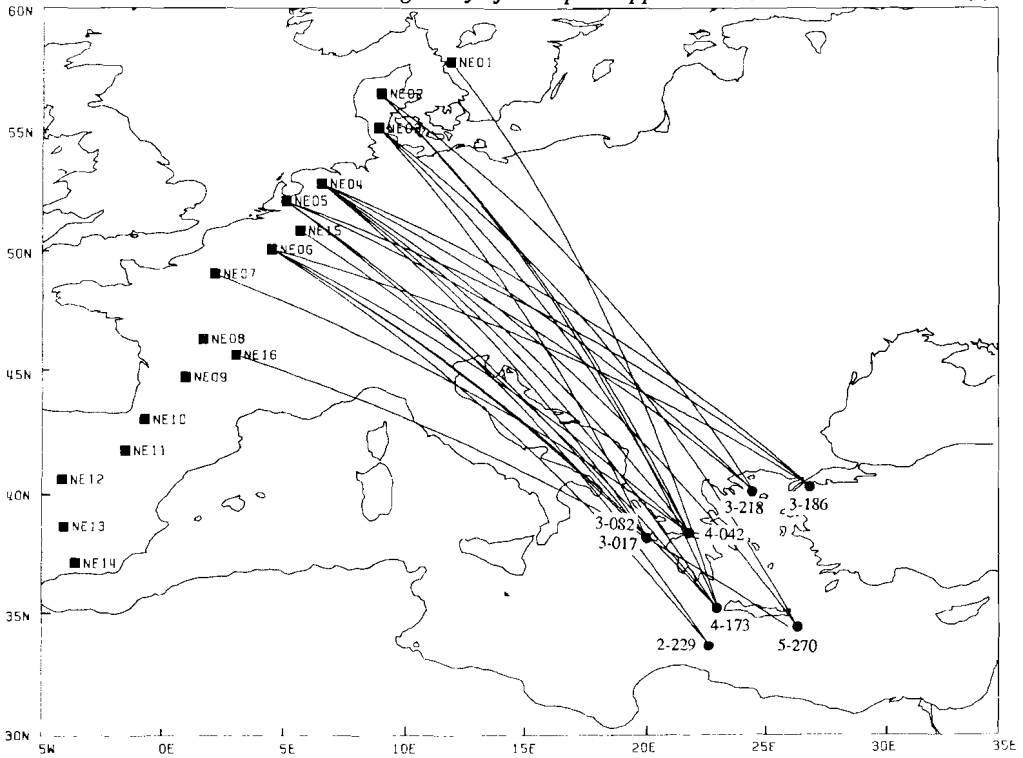


Figure 1. Locations of NARS stations and eastern Mediterranean events.

Mediterranean which triggered the recorders on body wave phases have been used. The study was restricted to the seismograms of stations NE01–NE16, because these data provided the densest sampling of the upper mantle between source and receiver region, thus allowing a detailed investigation of this part of the upper mantle.

An example of *P*- and *SH*-wave data for an event near Crete (event 4-173) is shown in Fig. 2. The observed variations in waveform of the wavetrains can be attributed to several effects. First, changes in epicentral distance can easily lead to large variations in the waveforms. Especially in the range of interest ( $15^{\circ}$ – $25^{\circ}$ ) interference of reflected and refracted waves can be severe. The radiation pattern of the source can also cause large changes in wave-

Table 1. Event parameters.

code	date	origin time	coordinates	depth	$m_b$
2-229	17 8 1982	22:22:20.0	33.71N 22.94E	1	6.1
3-017	17 1 1983	12:41:30.1	38.07N 20.25E	14	6.2
3-082	23 3 1983	23:51:05.5	38.23N 20.29E	13	5.6
3-186	5 7 1983	12:01:27.0	40.33N 27.12E	7	5.5
3-218	6 8 1983	15:43:51.9	40.14N 24.74E	2	6.0
4-042	11 2 1984	8:02:50.5	38.38N 22.08E	19	5.3
4-173	21 6 1984	10:43:40.5	35.31N 23.28E	25	5.8
5-270	27 9 1985	16:39:48.7	34.51N 26.60E	61	5.6

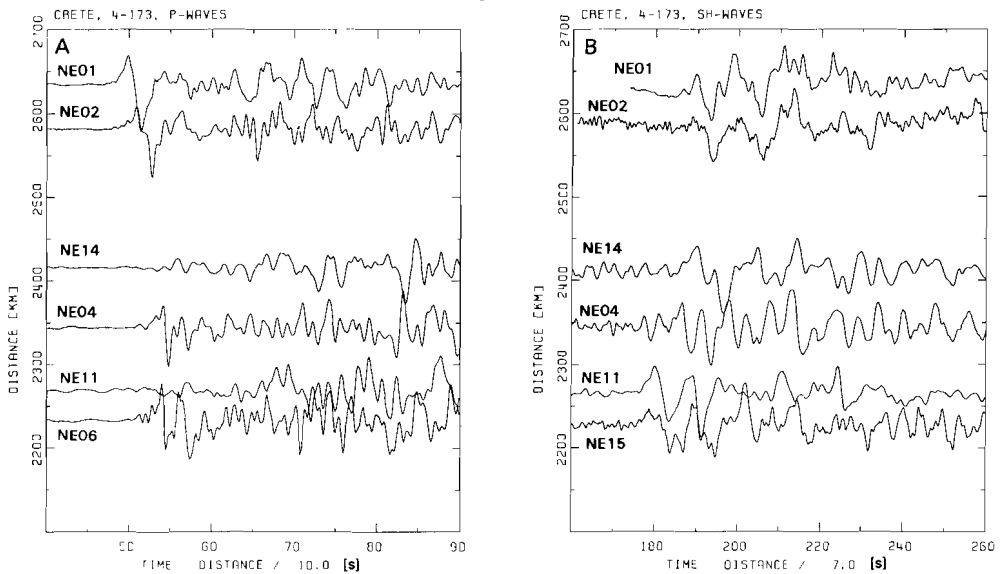


**Figure 2.** *P*-wave data on the vertical component (a), and *S*-wave data on the transverse component (b) of event 4-173. The reduced travel time in seconds is marked along the horizontal axis.

form signature, particularly for large differences in source azimuth. Finally, the structure below the stations may have a large effect on the recorded signals. It is of great importance that all these effects are correctly modelled or taken into account in order to obtain an unbiased estimate of the lateral heterogeneity of the region under study. A further discussion on this subject is given in Section 4.

Most previous studies of body-wave modelling have used long-period seismograms. As Ingate *et al.* (1986) have shown, only the gross velocity structure can be resolved from this kind of data. Fig. 3(a) shows four broad-band NARS and two long-period DWWSSN seismograms of an event in the Aegean Sea (event 3-218, see Table 1). The difference in frequency content of the seismograms of NE12 (NARS) and TOL (DWWSSN) can be seen from Fig. 3(b). The time separation for different branches of the *S*-wave travel-time curve varies typically between 0 and 20 s for epicentral distances between  $15^\circ$  and  $30^\circ$ . Thus, it is clear that separate arrivals generally cannot be recognized on long-period seismograms (see Fig. 3a). In contrast, broad-band seismograms, obtained from instruments with a flat frequency response to velocity between 0.01 and 1.0 Hz such as NARS instruments, are suitable for analysis of the wavetrain of upper mantle phases. Using this kind of data, travel times of most upper mantle phases can be determined relatively accurately and easily by synthetic modelling of the arrivals. Therefore, it is expected that a higher resolution of the upper mantle velocity structure can be obtained.

### 3 Method

In studies of body-wave modelling, the upper mantle velocity structure is determined by matching the wavetrains of upper mantle phases. The advantage over studies which use travel times of the first arrivals only is that travel-time information of later arrivals is also used, as well as amplitude information. In many cases the slowness of first and later arrivals can be determined by correlation of seismograms with different epicentral distances.

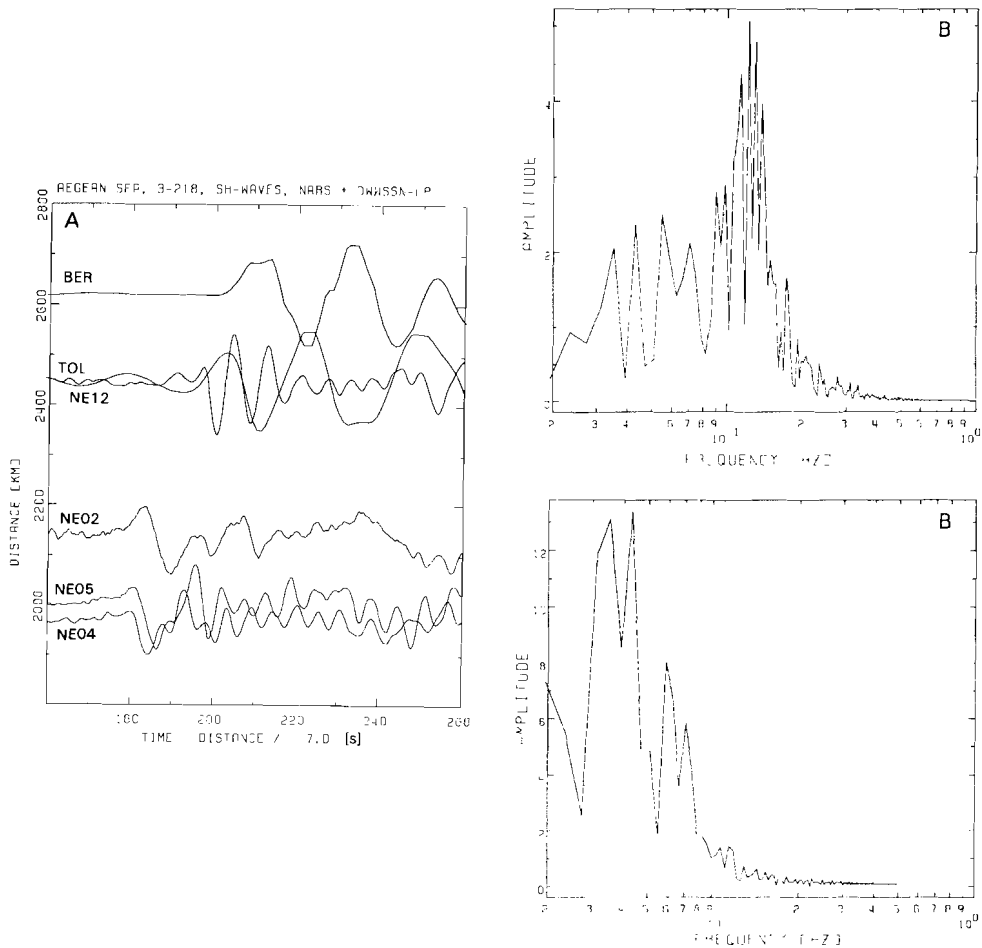


**Figure 3.** (a) Broad-band NARS, and long-period DWSSN *S*-wave data on the transverse component of event 3-218. The waveshape of the DWSSN long-period data is affected by clipping of the instrument. (b) Frequency content of the seismograms of NE12 (above) and TOL (below) for the time window shown in Fig. 3(a).

Practically, travel times are the easiest to model, although frequently one will not be able to identify the phases without the aid of synthetic seismograms and their travel-time curves. The travel-time branches of the direct (not surface reflected) waves are therefore indicated on the figures of Sections 5 and 6 which show data and synthetics.

The data are modelled by trial and error using the WKBJ method (Chapman 1978). Since the program we have available calculates seismograms for laterally homogeneous earth models it may seem inappropriate to use this technique for this application. However, because the horizontal velocity variations are likely to be several times smaller than the vertical variations (the data which are used sample a narrow region), it is assumed that effects due to lateral heterogeneity are of secondary importance, and need not be taken into account in a 'first-order approximation'. The method will therefore yield average models along the ray-paths, and the degree of heterogeneity is estimated by differences between the models obtained for different ray-paths, as far as they cannot be reconciled in a single model.

Features that are present in the data which cannot be modelled by the WKB method may sometimes be caused by shortcomings of the WKB technique, but the cases where the WKB method fails are known, and one can deal with these situations. For instance, it is known that diffracted rays are modelled with an amplitude which is slightly too large, it is awkward to model the low-frequency reflections from strong gradient zones, and tunnelling waves cannot be included in the synthetics (Grand & Helmberger 1984; Chapman & Orcutt 1985).

Using the WKB algorithm, Green's functions are computed for the  $P$ -,  $pP$ -, and  $sP$ -phases to model the  $P$ -wavetrains on the vertical component, and for  $S$ - and  $sS$ -phases to model the  $S$ -wavetrains on the transverse component. The radiation pattern given by a double couple solution is incorporated in the synthetics by multiplying the functions of each phase with the appropriate weights. For each event a clear  $P$ - and  $S$ -pulse was selected from the data. It is assumed that these wavelets represent the total effect of source time function, instrument response and attenuation for the  $P$ - and  $S$ -phases respectively. Green's functions are convolved with these pulses to produce the synthetic seismograms. This means that it is implicitly assumed that attenuation is the same for all  $S$  phases (including  $sS$ ), and for all  $P$  phases (including  $pP$  and  $sP$ ). This assumption is not ideal, but upper-mantle attenuation is not known accurately enough to be modelled with a high reliability. The results show that the approximation is adequate for modelling the most pronounced features of the seismograms. The consequences for the resolution of the models at discontinuities are discussed at the end of Sections 5 and 6.

Receiver structure effects have not been modelled because they make a relatively small contribution to the data. The first Moho reverberation near the receiver has a maximum amplitude of about 17 per cent of the direct wave for the most extreme case: reflections within the  $SH$ -system and a large velocity contrast across the Moho ( $3.40$ – $4.76$  km s<sup>-1</sup>). Signals of this amplitude which arrive in the tail of the wavetrain generally cannot be discerned. Constructive interference of Moho reverberations, generating a channelled crustal wave, may result in a high-amplitude, long-period wavetrain, but this phase arrives in the tail or outside the time window of interest.

Thus, only the most important phases which may be present in the data are modelled in this study. At this stage it does not seem justified to model all details of the seismograms since the structure of the Earth is not known accurately enough to estimate the relative importance of the many other contributions. As we will see, the modelling results appear to justify this assumption.

#### 4 The influence of source parameters in studies of body-wave modelling

It is important to estimate the effects which variations of the source parameters have on the synthetically calculated seismograms. The influence of the different parameters on the synthetics is illustrated by modelling four of the seismograms ( $SH$ -wave data) of the Crete event (4-173).

Synthetic seismograms of the  $S$ - and  $sS$ -phases on the transverse component calculated for the event parameters as published in the ISC bulletin (see Table 1), and in the PDE monthly bulletin ( $T_0$ : 10:43:42.1; event coord.: 35.360N, 23.238E; focal depth: 39 km; Fig. 4a) show the influence of the event location on the epicentral distance. The focal depth has its most pronounced effect on the (relative) travel times of the phases. The difference in origin time between the PDE and ISC determinations (1.6 s) is expressed by a shift in the travel times of the data which cannot be shown in this figure. Although the differences between the ISC and PDE locations for this earthquake were the largest of the events studied, these



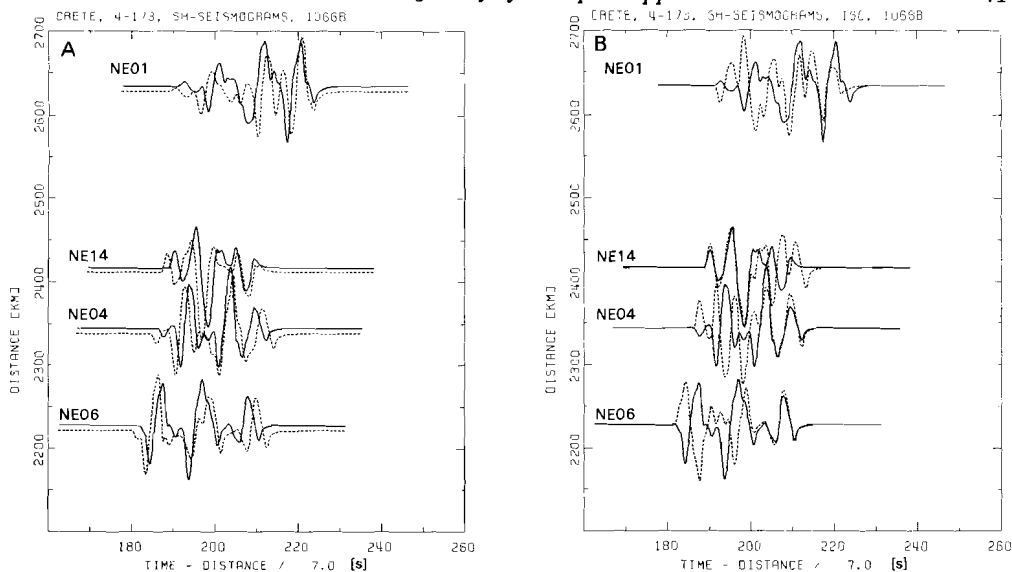


**Figure 4.** (a) Synthetic seismograms of event 4-173 calculated for ISC (solid line) and PDE (dashed line) event parameters. (b) Synthetic seismograms of event 4-173 calculated for the fault plane solution (solid line), and centroid moment tensor (dashed line).

results clearly show that one has to be careful not to use bulletin locations without further consideration. Differences in the event parameters such as these for the Crete event can already lead to significant changes in the derived velocity model. Therefore, it is necessary to discuss the effects of errors on the modelling results. The differences between the ISC and PDE locations and origin times have been taken as an estimate of uncertainty. Travel times and synthetics have been calculated for both sets, and it is observed that the arrival times of the first onsets differs by 0.5 s or less, which is approximately equal to the accuracy to which the  $P$ -wave data have been modelled, and much smaller than the differences in origin time. This is evidently due to the dependence in the origin time calculations on source location, especially focal depth. The event depth affects the time span between the direct and surface reflected phases, but for most shallow earthquakes it is not possible to identify the  $pP$ ,  $sP$ , and  $sS$  phases without the aid of synthetic seismograms. It is observed that the synthetics for ISC event parameters given an equal or better fit to the data than the 'PDE synthetics'. A correct estimation of the source depth appears most important for 10–15 km deep events, for which early surface reflected phases may interfere with later arriving direct phases. The ISC event depths of the earthquakes used in this study were thought accurate enough because of the good fit of the  $S$ – $sS$ - and  $P$ – $pP$ – $sP$ -waveforms.

Knowledge of the moment tensor is also of great importance in studies of waveform modelling. Fig. 4(b) shows the synthetic seismograms computed for the fault plane solution ('moderately well controlled'), and the best double couple solution of the (Harvard) centroid moment tensor as published in the ISC and PDE bulletins. Moment tensor solutions for smaller events ( $m_b < 6.0$ ) are generally not well constrained, and although differences between the fault plane solution, moment tensor solution and centroid moment tensor may be expected, due to the different approaches for the determination, completely different (best) double-couple solutions are frequently observed, sometimes resulting in polarity reversals of phases over a broad range of azimuths (see Fig. 4b). The moment tensor solution has a large effect on the  $sS/S$  (or  $pP/P$  and  $sP/P$ ) amplitude ratio on a single seismogram.

Thus, good knowledge of the radiation pattern is needed for a good amplitude fit of the phases which leave the source at different take-off angles. It is observed that the centroid moment tensor gives the best fit to the data for most of the earthquakes of this study, and this solution was used to model the data. In view of the uncertainties in the radiation pattern and other effects which might influence the amplitudes, modelling efforts were mainly concentrated on matching the travel times of the phases.

## 5 Determination of the *S*-wave velocity structure

The data which have been analysed cover a narrow region as can be seen from Fig. 1. The best fitting models to the seismograms are found by trial and error. Model 1066B (Gilbert & Dziewonski 1975) proved to be an adequate initial (reference) earth model for fitting the *S*-wave data. The travel times of the first arrivals of this model generally correspond within 2 or 3 s with the data. These travel-time anomalies could not be attributed to erroneous origin time determinations only, since there appeared to be no systematic positive or negative delay for each event. Also, no general trend could be observed for the travel time anomalies with epicentral distance. A unique model which would fit all the *SH* data for the region between south-eastern and north-western Europe could therefore not be obtained. Still, there are some features of the velocity structure valid for all paths. In the following I will show how these features of the upper mantle shear velocity structure are inferred from the data.

### SEISMOGRAMS WITH EPICENTRAL DISTANCES LESS THAN 20°

The larger part of the data set consists of seismograms with an epicentral distance between 15° and 20°. These data give the most detailed information of the upper mantle structure to the 400-km discontinuity. Interference of upper mantle phases can easily produce long and complicated wavetrains on which several arrivals may be recognized. For a structure without a low velocity zone (LVZ) the first arrival will be a refracted wave above the 400-km discontinuity. The second and third arrivals are then reflections from the 400- and 650-km discontinuity, respectively. This picture becomes more complicated when a LVZ is present. Then, the first arrival can be the *Sn*-phase, the phase travelling in the lid just above the LVZ. In the shadow of the LVZ, the *Sn*-phase is not present as a ray geometrical arrival, but may be observed as a diffracted phase. A later arrival is the phase which is refracted at the bottom of the LVZ, followed by the reflections of the two discontinuities. I mention only the two main discontinuities at this stage, because no evidence was found for other strong gradients or discontinuities.

Some seismograms clearly present evidence for a high velocity lid above a LVZ. On the seismograms with an epicentral distance less than 17° (1900 km) a precursory arrival can be observed (see Fig. 5) which is identified as the *Sn*-phase. Its amplitude decays very rapidly beyond 17°, which would indicate the start of a shadow zone. However, the three seismograms with an epicentral distance less than 1900 km, showing the *Sn*-phase, are all recorded in the same station (NE06). Unfortunately, there are no data from other stations in this distance range, but there is a seismogram from the same station at an epicentral distance of 18.7° (2060 km) which also shows the *Sn*-phase. One can explain this observation in two ways. It is possible that the *Sn*-phase is not observed in the other stations because the shadow zone starts at a smaller epicentral distance along the ray-paths to these stations. This would imply a smaller lid thickness for the structure along these ray-paths than for the ray-paths to station NE06. Another explanation is that the *Sn*-phase is not observed in the other

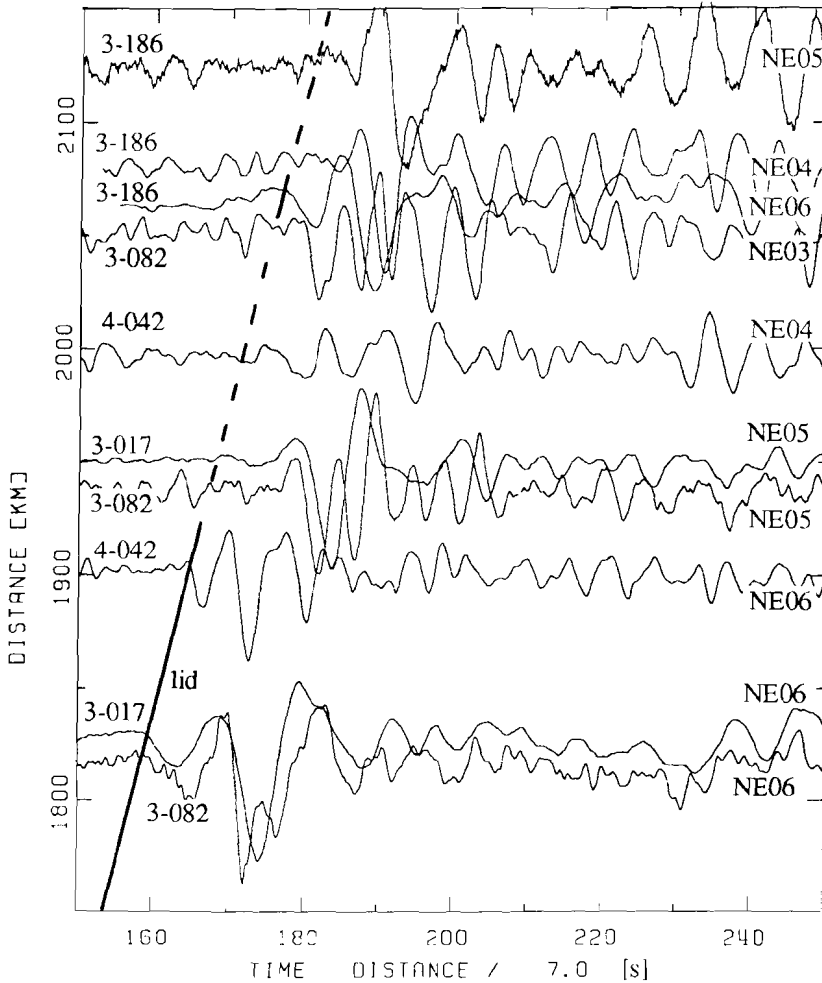


**Figure 5.** *S*-wave data on the transverse component of events in the eastern Mediterranean. The line is the predicted *Sn* arrival time (solid where observed, dashed where not).

stations because of scattering, which diminishes its amplitude. Both interpretations, however, are indicative of heterogeneity to depths of at least 120 km. This is the depth of the start of the LVZ determined for the observations of station NE06 for an average lid-velocity of  $4.4 \text{ km s}^{-1}$ . It is not possible to determine the velocity structure in the lid accurately because of the sparseness of the data and the variations that these data already show, but, to be compatible with these and following observations, average velocities must lie within the range  $4.4\text{--}4.7 \text{ km s}^{-1}$ . The maximum thickness of the lid can vary between 70 and 110 km, depending on the lid-velocities assumed.

Apart from the observations of the *Sn*-phase, the existence of a low velocity zone could also be established from arrivals from the underside of the low velocity zone, identified on seismograms with an epicentral distance larger than  $21^\circ$ . There are three events with such data. Fig. 6 shows the data for event 2-229, and the arrival from the gradient at the underside of the low-velocity zone can clearly be identified. The other two events have source depths of 25 and 61 km, respectively, and, because of the late arrival of the *sS*-phase, these

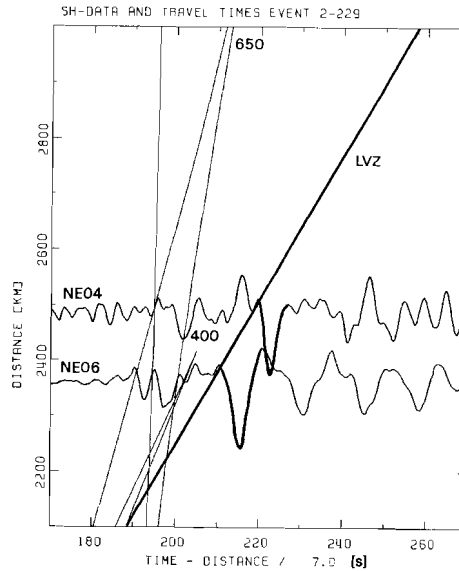
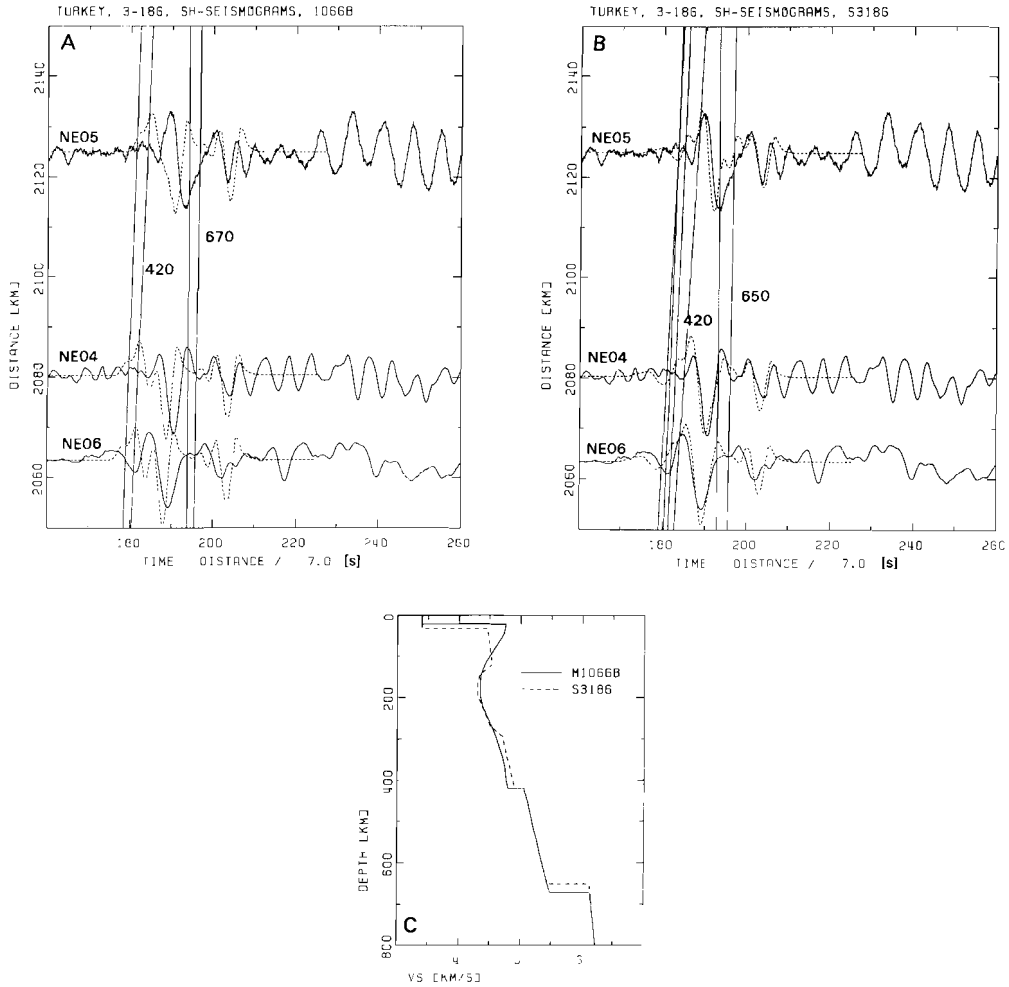


Figure 6. *SH*-wave data and travel-time curves of the *S*-phases of event 2-229.

are less clear examples (Fig. 12a, b, 13a, b). These seismograms provide a very good constraint on velocity structure of the lower gradient of the LVZ, but the actual minimum velocity in the LVZ cannot be determined from body-wave data.

The seismograms of event 3-186 show consistent waveshapes whose general features can be produced by a single model. The synthetics of model 1066B (Fig. 7a) for this event clearly show earlier arrivals from the 420-km discontinuity than observed in the data, while the reflection from the 670-km discontinuity is 1 or 2 s earlier in the data. A model which includes a lid (max. depth 120 km;  $\nu_s = 4.5 \text{ km s}^{-1}$ ), a LVZ (max. depth 300 km; min.  $\nu_s = 4.3 \text{ km s}^{-1}$ ), about 4 per cent higher velocities than model 1066B just below the LVZ, and two discontinuities at 420 and 650 km depth explains the data reasonably well (Fig. 7b). The velocity structure of the lid is not very well constrained. Its effect can be recognized by the first small negative onset, and it can be seen that this feature is not consistent between the data of NE06 and the two other stations. The early arrival from the 420-km discontinuity has been matched by an increase of the velocities below the LVZ by a constant value, but could also have been obtained by a decrease in depth of the discontinuity to about 360 km, or a combination of both effects.

When the synthetics of event 4-042 (Fig. 8a) are calculated for the same model, a reasonable fit is obtained except for the data of NE02. The amplitudes of most phases have not been modelled adequately, but the travel times generally agree within 2 s. A better fit to the data of NE02 can be obtained by a small change in the velocity structure of the lid and upper part of the LVZ (Fig. 8b), but this model clearly does not fit the seismograms of the other stations so well. The first negative onset of the seismogram of NE06 is interpreted as the *S<sub>n</sub>*-phase. It would require a decrease in the average velocity of the lid from 4.5 to  $4.4 \text{ km s}^{-1}$  to model this phase better. There is some indication that the reflection from the 650-km discontinuity is not matched adequately, but the phase is too weak or too contaminated by interference with other phases to justify any conclusive interpretation. The data at epicentral distances less than  $20^\circ$  do not constrain the structure below the 400-km discontinuity very well.



**Figure 7.** (a) *SH*-wave data of event 3-186 (solid line) and synthetics for model 1066B (dashed line); vertical lines represent the travel-time branches of the *S*-phases of the model. (b) Data and synthetics for model S3186. (c) Shear velocity models 1066B and S3186.

The phases of event 3-082, to the west of the two previous events, have their ray-paths for a large part beneath the Adriatic Sea. In contrast to the reasonable fit obtained for the seismograms of event 4-042, a bad fit is obtained for the data of event 3-082 using the same model that matches the data of event 3-186 (see Fig. 9a). Trial and error modelling leads to the conclusion that acceptable models require low velocities below the LVZ than the model for events 3-186 and 4-042. The subchannel velocities are then again in agreement with model 1066B in this depth range. The seismograms of NE05 and NE04 (NE04 is not shown here because it is at the same epicentral distance as NE05, and has a very similar waveshape) do not show an arrival from the bottom of the LVZ, or one coinciding with 400-km reflection (Fig. 9b). The large, broad, positive maximum on the seismogram of NE06 can only be achieved when the travel-time branches of the 400-km reflection and the arrival from the LVZ are closely separated in time (Fig. 9b). Thus, the data of these three (including NE04) stations indicate that at an epicentral distance larger than or equal to

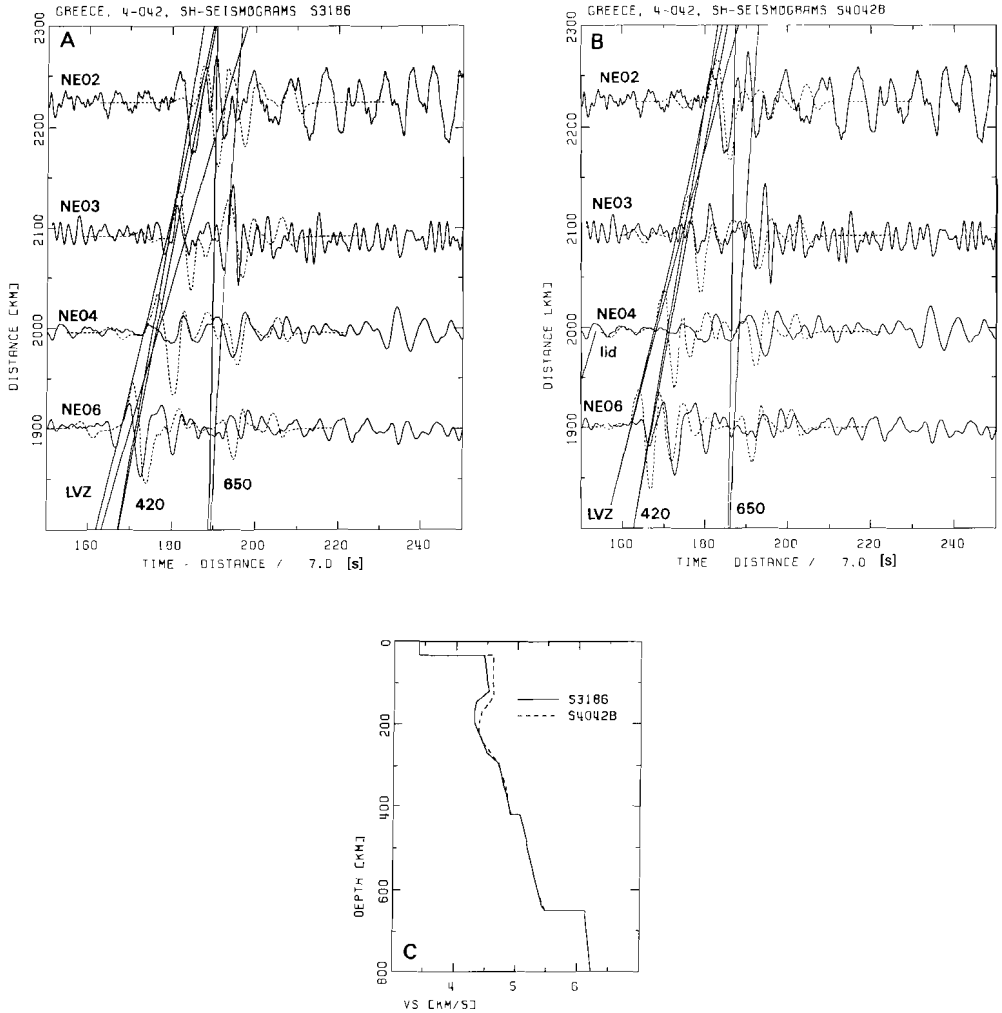


**Figure 8.** (a) *SH*-wave data of event 4-042 (solid line) and synthetics for model S3186 (dashed). (b) Data and synthetics for model S4042B. (c) Velocity models S3186 and S4042B.

1950 km the phase from the 400-km discontinuity should arrive as a first arrival. However, the data of NE03 can only be matched correctly when the phase from the LVZ arrives first (Fig. 9c). An earlier arrival of the phase from the LVZ can be achieved by an increase of the velocities in the lid and bottom side of the LVZ, while a late 400-km reflection, such as is observed, can either be explained by an increase in the depth of the discontinuity, or a decrease in the velocities below the LVZ. Unfortunately, the trade-off between these two possibilities cannot be resolved by the data of one seismogram only.

The data of event 3-017, whose hypocentre lies very close to that of event 3-082, are very well modelled by the velocity structure obtained for event 3-082 (Fig. 10), although a slightly higher average lid velocity ( $4.45 \text{ km s}^{-1}$  instead of  $4.40 \text{ km s}^{-1}$ ) is adopted which yields a better travel-time fit of the total signal. This particular event has been modelled using the fault plane solution instead of the centroid moment tensor, as the former gives a better *sS/sS* amplitude ratio for the data of station NE06.

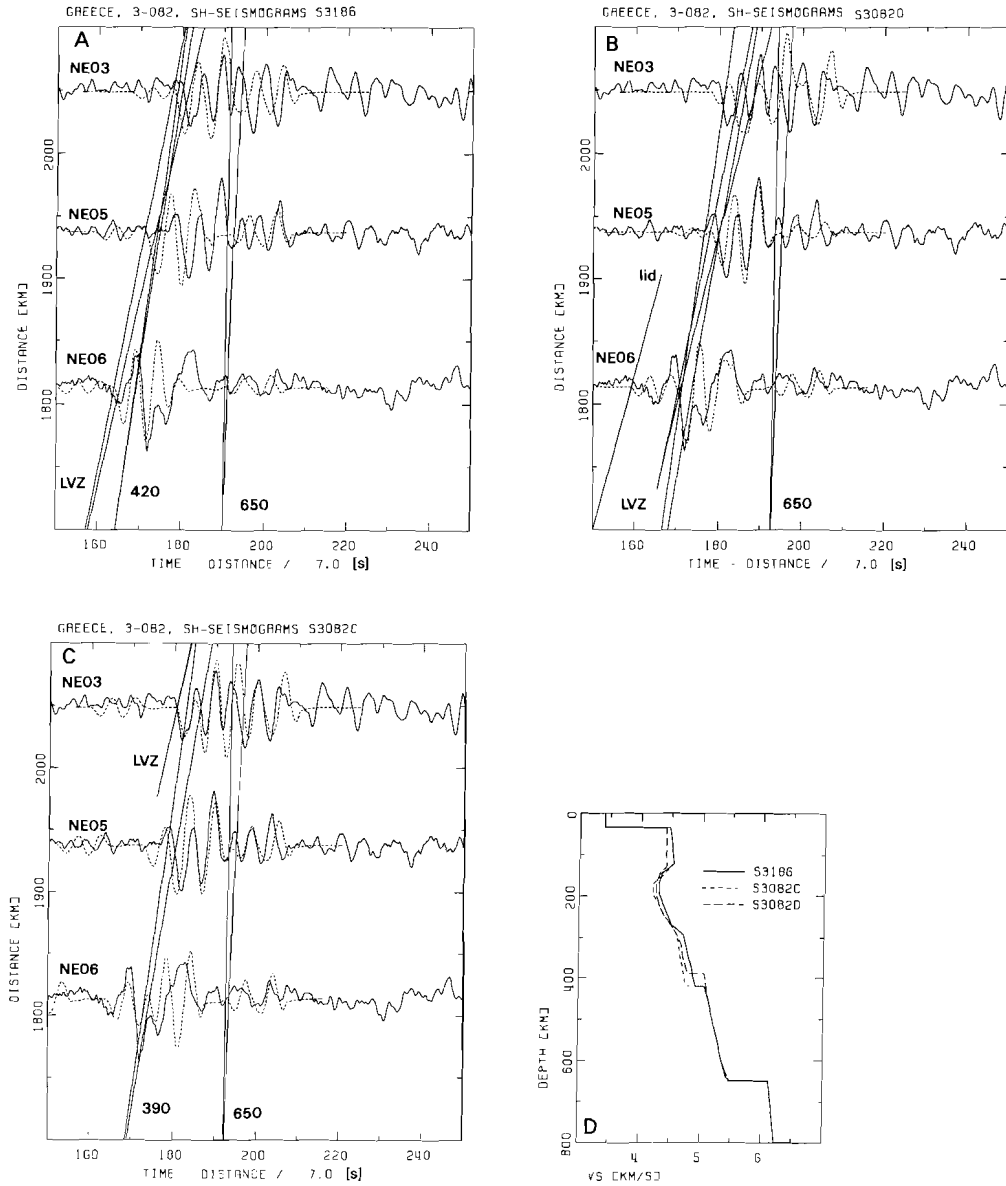


**Figure 9.** (a) *SH*-wave data of event 3-082 (solid line) and synthetics for model S3186 (dashed). (b) Data and synthetics for model S3082D. (c) Data and synthetics for model S3082C. (d) Velocity models S3186, S3082C, and S3082D.

The data of event 3-218 very clearly point to heterogeneity to depths of approximately 400 km. The main features of the data of stations NE04 and NE05 are reasonably well matched by a model which has practically the same velocity structure as the model which fits the data of station NE03 for event 3-082 (the model of Fig. 9c; see Fig. 11a). However, the synthetics of this model do not match the data of station NE02 at all. This seismogram requires a velocity model which is more similar to that which fits the data of event 3-186 (Fig. 11b).

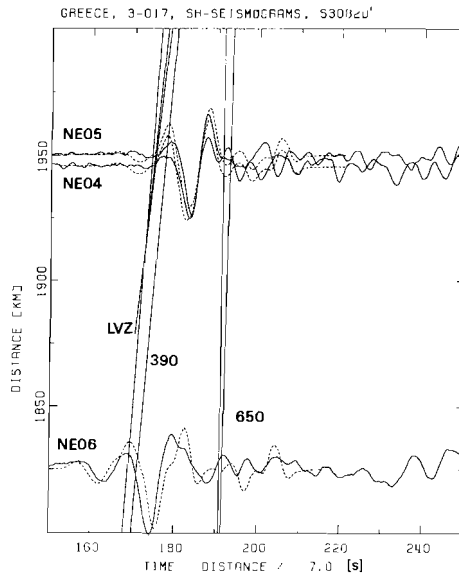


**Figure 10.** *SH*-wave data of event 3-017 (solid line) and synthetics for model S3082D with an average lid-velocity of  $4.45 \text{ km s}^{-1}$ .

#### SEISMOGRAMS WITH EPICENTRAL DISTANCES LARGER THAN $20^\circ$

Seismograms with an epicentral distance larger than  $20^\circ$  provide more information about the structure of the upper mantle beneath the 400-km discontinuity. Depending on the velocity structure and the epicentral distance, several of the following phases may be observed: refractions from the bottom of the LVZ, transition zone, and lower mantle, and reflections from the two discontinuities. Most upper-mantle shear wave velocity models show that the phase from the lower mantle is the first arrival for epicentral distances greater than  $25^\circ$ . Phases reflected from the 650-km discontinuity can be present to a distance of  $30^\circ$ , and from the 400-km discontinuity to  $27^\circ$ , which are the extreme values obtained for previous upper mantle models.

When synthetic seismograms of event 4-173 are calculated for the model of event 3-082 (for stations NE04, NE05, and NE06), it can be seen that this model does not fit the data very well (see Fig. 12a). The ray-paths of the phases to station NE04 for these two events differ little in azimuth, but the seismogram of event 4-173 gives a better constraint to the velocity structure within the transition zone because of its larger epicentral distance. The records of NE04 and NE15 show a better fit with the synthetics for a model which has nearly the same velocity structure to the 400-km discontinuity as the model for event 3-082 (stations NE04, NE05, NE06), but has higher velocities below the 400-km discontinuity (see Fig. 12b). This model had earlier been obtained by matching the travel times of event 2-229 (Fig. 6). The data of NE01 and NE02 (Scandinavia) are not equally well matched by this model, which indicates that the velocity structure along the ray-paths to these two stations differs noticeably from that of the two stations in the Netherlands (NE04, NE15).

A smaller gradient in the transition zone than given by model 1066B due to higher velocities below the 400-km discontinuity are also supported by the data of event 5-270.



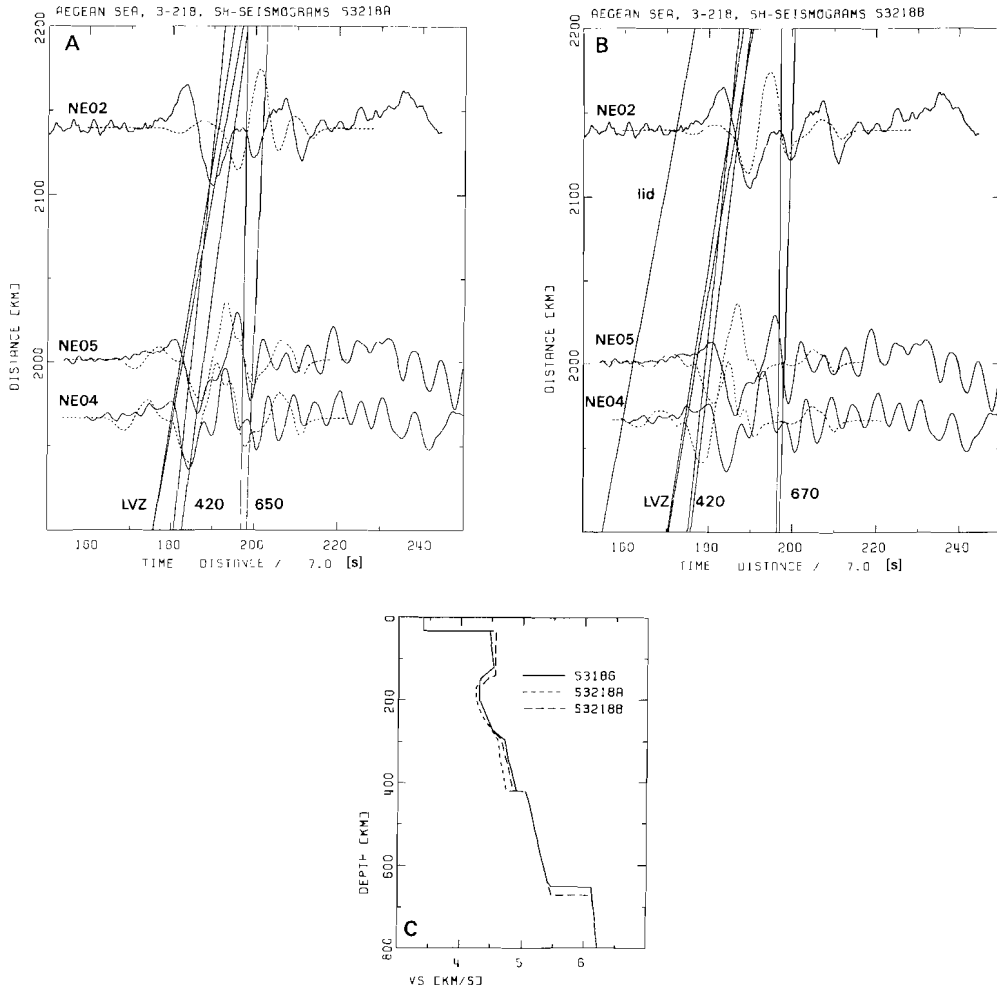


**Figure 11.** (a) *SH*-wave data of event 3-218 (solid line) and synthetics for model S3218A (dashed). (b) Data and synthetics for model S3218B. (c) Velocity models S3186, shown for reference, S3218A, and S3218B.

Fig. 13(a) shows the data and synthetics for a model that matches the data of event 3-218 for station NE02. A model with the same velocity structure in the transition region as for the previous event improves the fit of the first arrival, while a decrease of the velocities in the lid by 5 per cent improves the fit of the later arriving wavetrain. The synthetics for this model are shown in Fig. 13(b).

INTERPRETATION OF THE S-WAVE MODELLING RESULTS

Although the previous observations are indicative of distinct lateral heterogeneity, all upper mantle shear wave models show the same features: a high velocity lid ( $4.4\text{--}4.7\text{ km s}^{-1}$ ), a low-velocity zone with minimum velocities of  $4.20\text{--}4.38\text{ km s}^{-1}$  extending from 120 to 300 km, and two discontinuities at about 420 and 650 km depth with velocity jumps from  $4.80$  to  $5.20\text{ km s}^{-1}$  and  $5.48$  to  $6.1\text{ km s}^{-1}$ , respectively. However, there are practically no

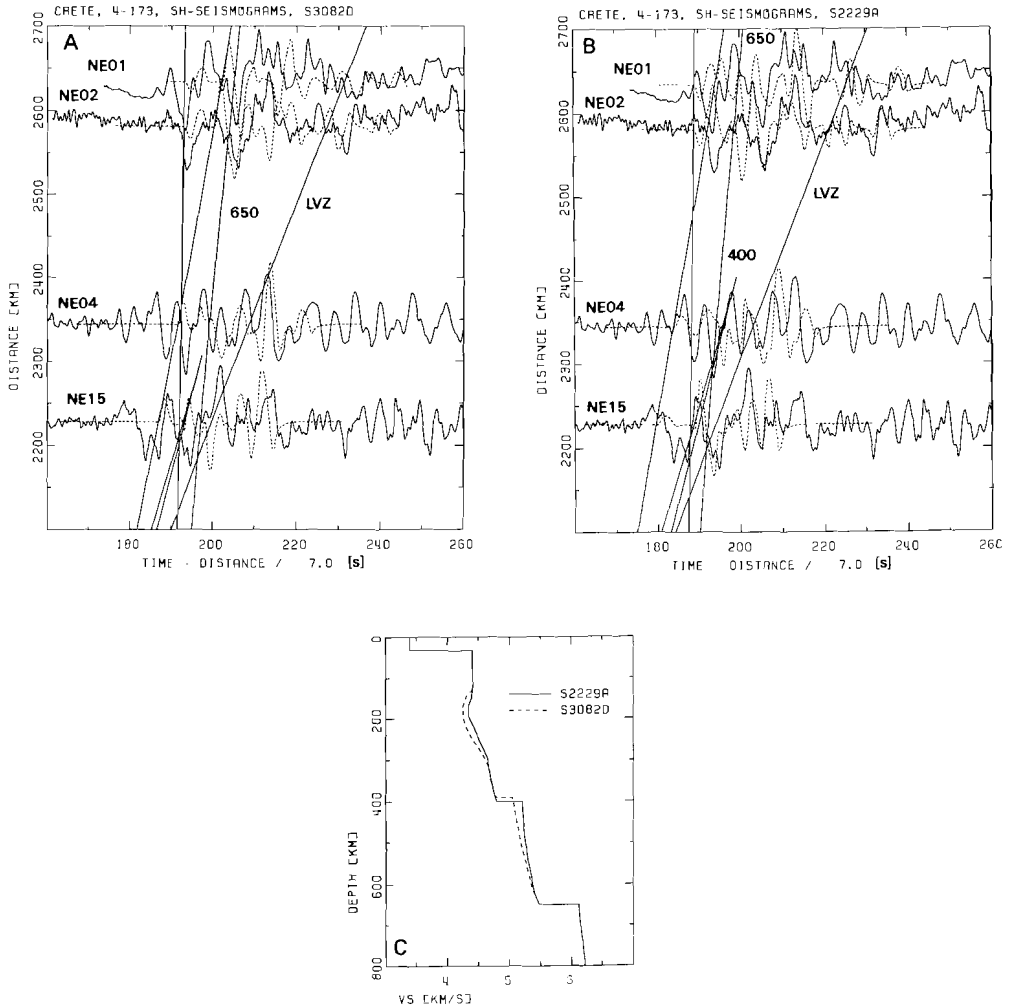


**Figure 12.** (a) *SH*-wave data of event 4-173 (solid line) and synthetics for model S3082D (dashed). (b) Data and synthetics for model S2229A. (c) Velocity models S2229A and S3082D.

phases which give a constraint to the structure below the 650-km discontinuity, so this part of the model is not well resolved. This average structure is in many respects compatible with previous shear wave models obtained for Europe. Model M7 (Nolet 1977), which is inferred from higher mode Rayleigh wave data of Scandinavia and the western European Platform, shows a high-velocity lid and a low-velocity zone which are similar but less distinct than most of the models of this study. The 400-km discontinuity of this model is located at a shallower depth (380 km). Dost (1986), using data of the NARS array, showed that higher mode Rayleigh wave data for the western European Platform require a more pronounced low-velocity zone than that of the M7 model. Dost's model (WEPL1) is remarkably similar to the average structure of the models obtained in this study to a depth of 300 km. The resolution of the surface wave data is not high enough at greater depths to allow a detailed comparison with the models from this study. Mayer-Rosa & Mueller (1973) were the first to present both *P*- and *S*-wave velocity models of the upper mantle beneath Europe. They

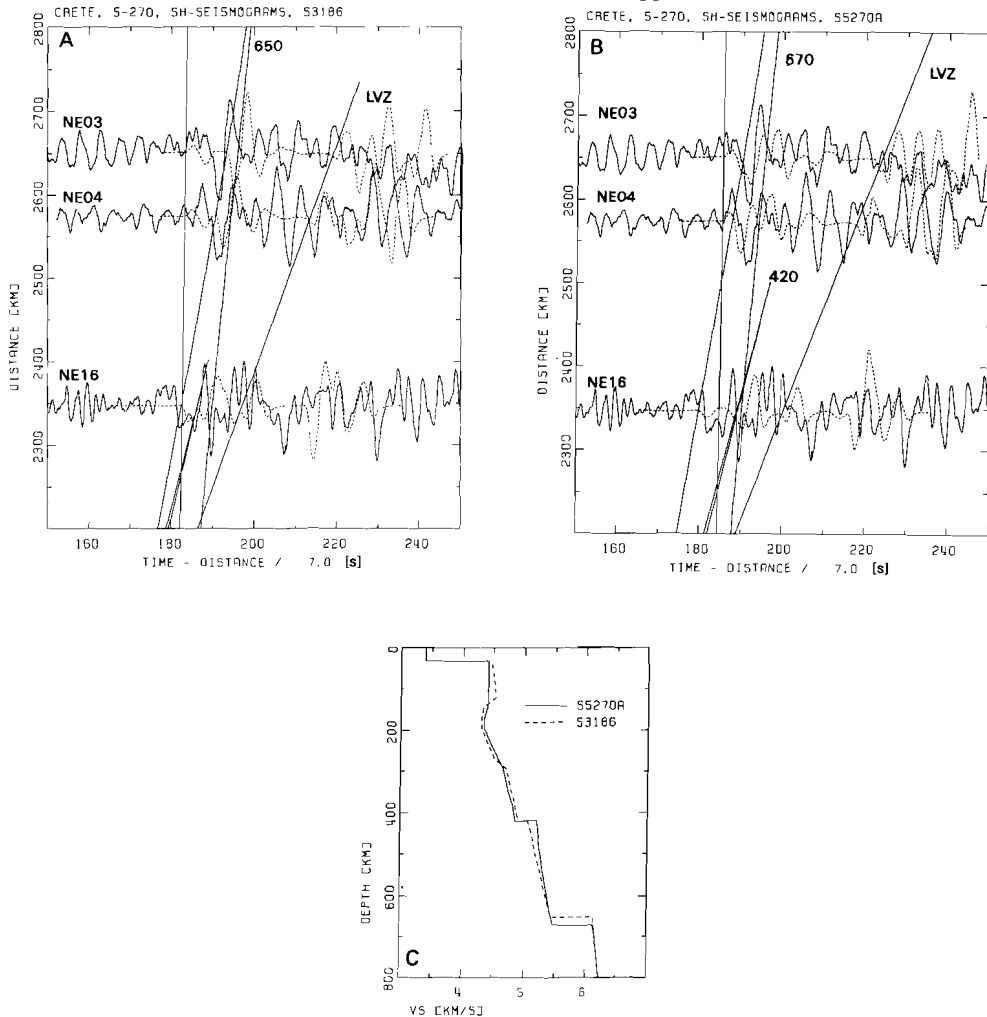


**Figure 13.** (a) *SH*-wave data of event 5-270 (solid line) and synthetics for model S3186 (dashed). (b) Data and synthetics for model S5270A. (c) Velocity models S3186A and S5270A.

recognized changes in the velocity structure beneath south-east and south-west Europe, but explained the variations in the travel times for the two regions by models which include three low-velocity zones to a depth of 300 km. Although many of these travel-time variations could also be interpreted by heterogeneity on a smaller scale, the most pronounced low-velocity zone in their models, at 200 km, seems to be a real feature.

In contrast to previous studies, this analysis of broad band data presents a rough estimate of the degree of lateral heterogeneity in the shear wave structure between the eastern Mediterranean and north-west Europe to a depth of about 400 km. Unfortunately, there are not many seismograms which give us information about the structure in and below the transition zone, but these records do not indicate as much heterogeneity as is observed for shallower depths. One might have expected severe heterogeneity below the Mediterranean region, because of its tectonic complexity (McKenzie 1972). However, the modelling results show that heterogeneity at the receiver part of the ray-paths is also resolved: it is frequently

observed that one model cannot explain the features of all seismograms for one event. Although one should keep in mind that these models can only represent the average structure between source and receiver, many of these variations can be correlated with the tectonic setting along the ray-paths or with results of other studies. For example, 2–4 per cent higher velocities in lid and LVZ are needed to explain the *S*-wave data of station NE02, when compared with the velocity structure determined for the seismograms of the other stations on the western European Platform (see the models for the events 3-218 and 4-042). This can be interpreted as a shield-like structure below northern Denmark, which is part of the Baltic Shield. Another remarkable observation is that, except for station NE03, the seismograms of event 3-082 and 3-017 in the Ionian Sea which have ray-paths beneath the Adriatic Sea require lower velocities in and below the LVZ, than the seismograms of 4-042 in Greece. This observation is consistent with tomographic inversion results for the Mediterranean (Spakman 1986b) which show low *P*-wave velocities in the depth range from 110 to 420 km beneath the Adriatic Sea when compared to the velocity structure east of the Adriatic and Ionian Sea. Nolet, Panza & Wortel (1978) determined a model for the shear wave velocity in the lithosphere of the Adriatic subplate from surface waves. Their model shows an increase in velocity from 4.27 to 4.80 km s<sup>-1</sup> between depths of 35 and 80 km. The gradient is larger, but the average velocity of the lid is equivalent with the model which is determined in this study. The depth to the LVZ is not well resolved by the study of Nolet *et al.* Another striking feature in the results of this study is the low value of the velocities in and below the LVZ obtained for the seismograms of event 3-218. There are presently no other studies which support this observation, but we will see that the same feature can be recognized in the *P*-wave velocity structure.

It should be emphasized that the discontinuities have been modelled by a step in velocity only because the thickness of the discontinuities cannot be determined by this analysis. The reason for this is that amplitude and frequency information cannot be used due to the simplifications which are made with respect to attenuation. Only when attenuation can be modelled with a high accuracy, is it possible to determine the thickness of the discontinuities by waveform analysis of the reflected phases in studies of this kind. Furthermore, due to the trade-off between the velocity structure above the discontinuity and the depth of the discontinuity, it is not possible to determine the depth of the discontinuities with an accuracy greater than about 10 km. The depth of the discontinuities could be determined more precisely if the velocity structure above the discontinuities were known accurately, but, because of the heterogeneity to the 400-km discontinuity which is recognized in this study, a higher accuracy in a 1-D model would be meaningless.

## 6 Determination of the *P*-wave velocity structure

Much of the information given in the previous section concerning the *S*-wave observations can also be related to the *P*-wave observations. Most of the seismograms which are used for *S*-wave modelling are also used for *P*-wave modelling. The data set is only different for those seismograms for which triggering occurred on the *S*-waves (no *P*-phases), or for which (one of the) horizontal seismographs were unstable (no *S*-wave modelling). Vertical-component seismograms were used to model the *P*-, *pP*-, and *sP*-phases. Similar to the result obtained for *S*-wave modelling, it appeared to be impossible to find one model that would fit all *P*-wave data. The *P*-wave structure of model 1066B could not be used as a starting model, since large travel-time differences between data and synthetics are observed (delays up to 8 s), especially for seismograms with a small epicentral distance. The *P*-wave velocity structure of 1066B has a constant gradient from the crust to the 420-km discontinuity with an average

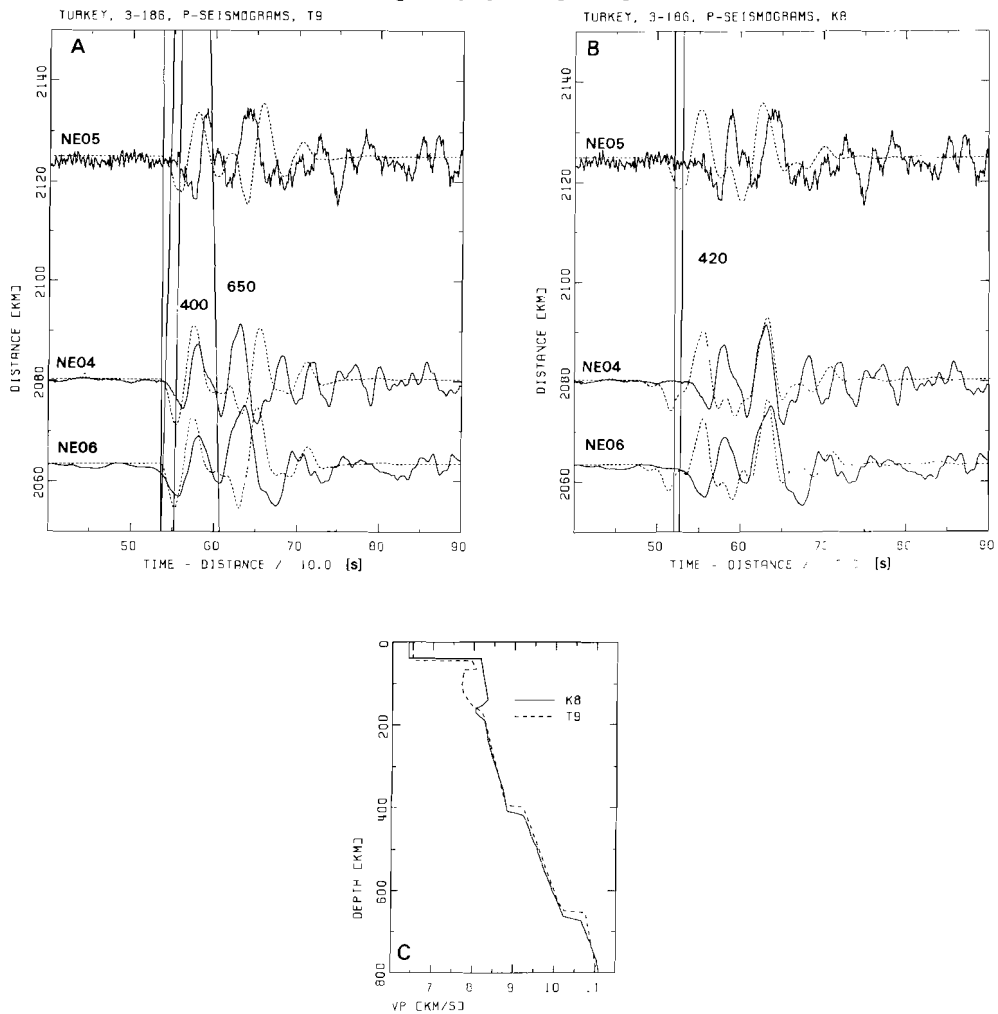


**Figure 14.** (a) *P*-wave data of event 3-186 (solid line) and synthetics for model T9 (dashed), (b) Data and synthetics for model K8. (c) Velocity models K8 and T9.

velocity which is obviously too high for central Europe, particularly at shallow depths. Nor do reference earth model PREM (Dziewonski & Anderson 1981) or other regional models fit the data well enough to be representative of the average velocity structure between south-east and north-west Europe.

#### SEISMOGRAMS WITH EPICENTRAL DISTANCES LESS THAN $20^\circ$

The *P*-wave structure to a depth of 400 km can be inferred from seismograms with an epicentral distance less than  $20^\circ$ . For models with a LVZ *P<sub>n</sub>*-phases may be observed to an epicentral distance which depends on the velocity structure and depth extent of the lid. The first arrival for larger epicentral distances is the phase from the bottom of the LVZ. For velocity distributions without a LVZ phases refracted above the 400-km discontinuity arrive first. Phases reflected from the 400- and 650-km discontinuity may be recognized as later arrivals on seismograms with an epicentral distance less than  $20^\circ$ .

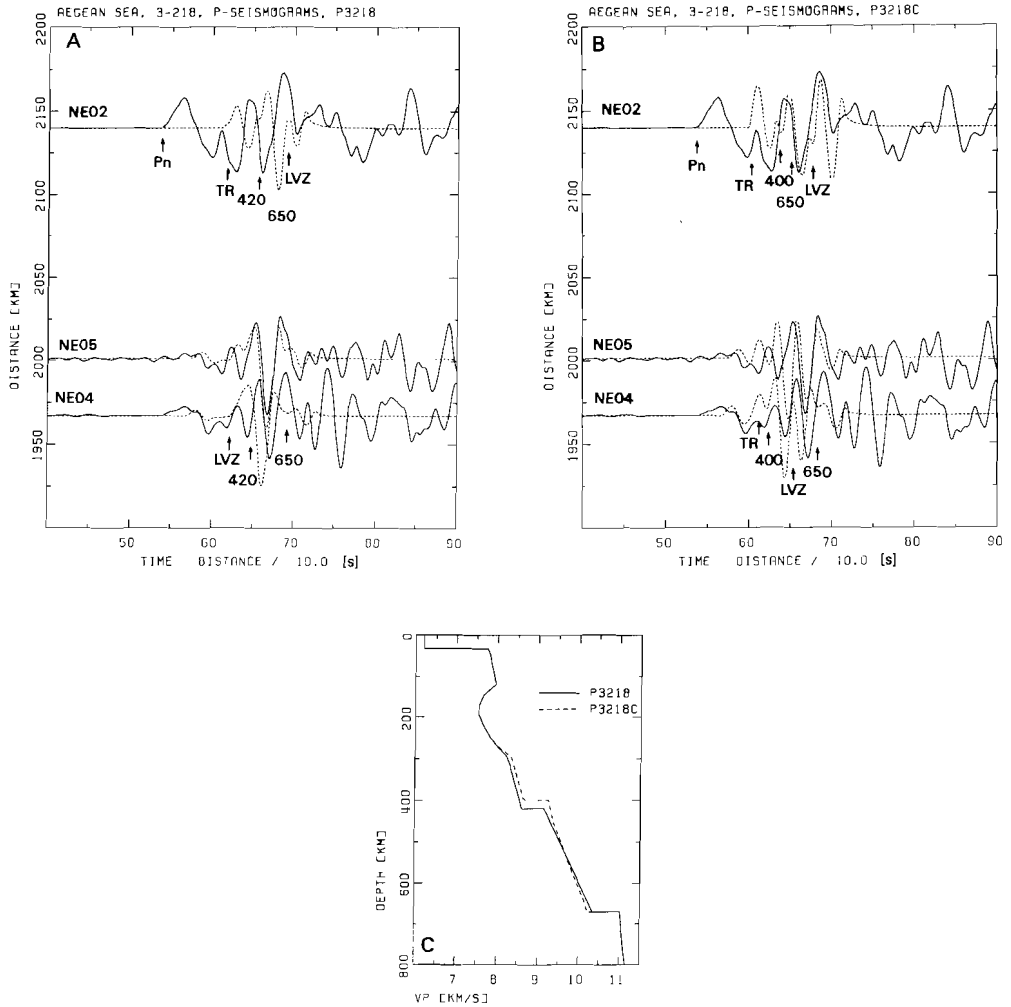


**Figure 15.** (a) *P*-wave data of event 3-218 (solid line) and synthetics for model P3218; arrows indicate the arrival times of the phases; TR represents the phase from the transition zone. (b) Data and synthetics for model P3218C. (c) Velocity models P3218 and P3218C.

The *P*-wave data of this study do not show clear *P<sub>n</sub>*-phases similar to the *S<sub>n</sub>*-phases except for the data of one event. This could be an indication for the absence of a *P*-wave LVZ beneath the larger part of the region. However, there is evidence for an increase in the velocity gradient at approximately 200 km depth, which can be inferred from phases coming from this gradient zone. Moreover, it is observed that travel times of phases which bottom above the 400-km discontinuity are relatively slow.

Fig. 14 shows the data of event 3-186 together with the synthetics for the tectonic model T9 (Burdick 1981), and for the model which is thought representative for the continental structure of north-west Eurasia, model K8 (Given & Helmberger 1980). The two models differ mainly in the velocity structure to a depth of 250 km. The tectonic model predicts a correct arrival time of the first phase, while the continental model gives a better fit to the 670-km reflection (diffracted). It is observed that changes in the velocity structure below

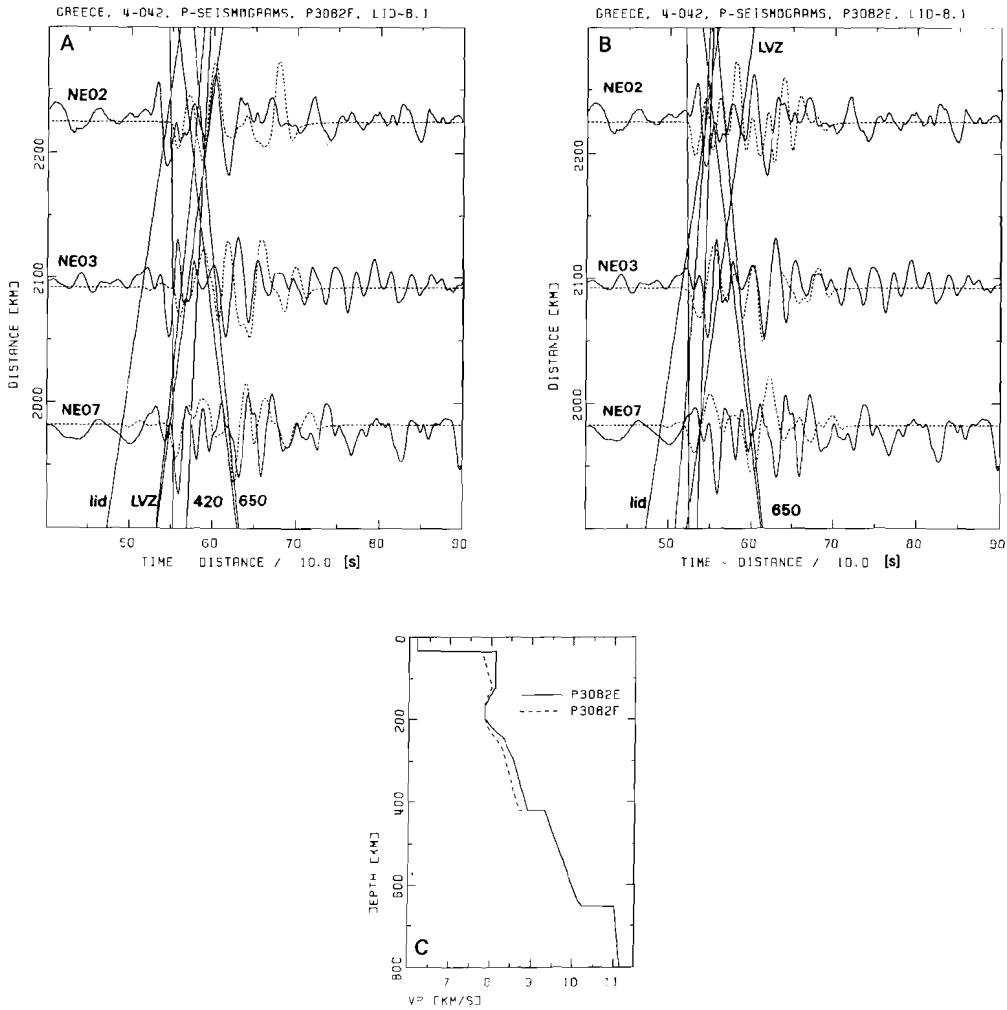


**Figure 16.** (a) *P*-wave data of event 4-042 (solid line) and synthetics for model P3082F with a lid velocity of  $8.1 \text{ km s}^{-1}$ . (b) Data and synthetics for model P3082E with a lid velocity of  $8.1 \text{ km s}^{-1}$ . (c) Velocity models P3082E and P3082F with lid velocities of  $8.1 \text{ km s}^{-1}$ .

250 km are needed to match the complete waveform. A model with a LVZ at the same depth interval as for the *S*-wave velocity model gives a better, although not optimal, fit to the data.

Evidence for a *P*-wave LVZ comes from a precursory arrival on the seismograms of event 3-218. This arrival has a high amplitude on the seismogram of NE02 for this event, and is much smaller on the data of the other two stations. The later arrivals of the seismograms can very well be explained by phases which bottom at depths greater than 200 km, assuming a pronounced LVZ (see Fig. 15a, b). However, the first arrival can only be explained as a phase which has travelled through a high-velocity lid, or, equivalently, the *P<sub>n</sub>*-phase. The WKB method cannot model this whispering gallery phase with the correct amplitude and frequency content without including a lot of internally reflected phases. The velocity structure that matches the data of NE05 does not fit the data of NE04 equally well (only

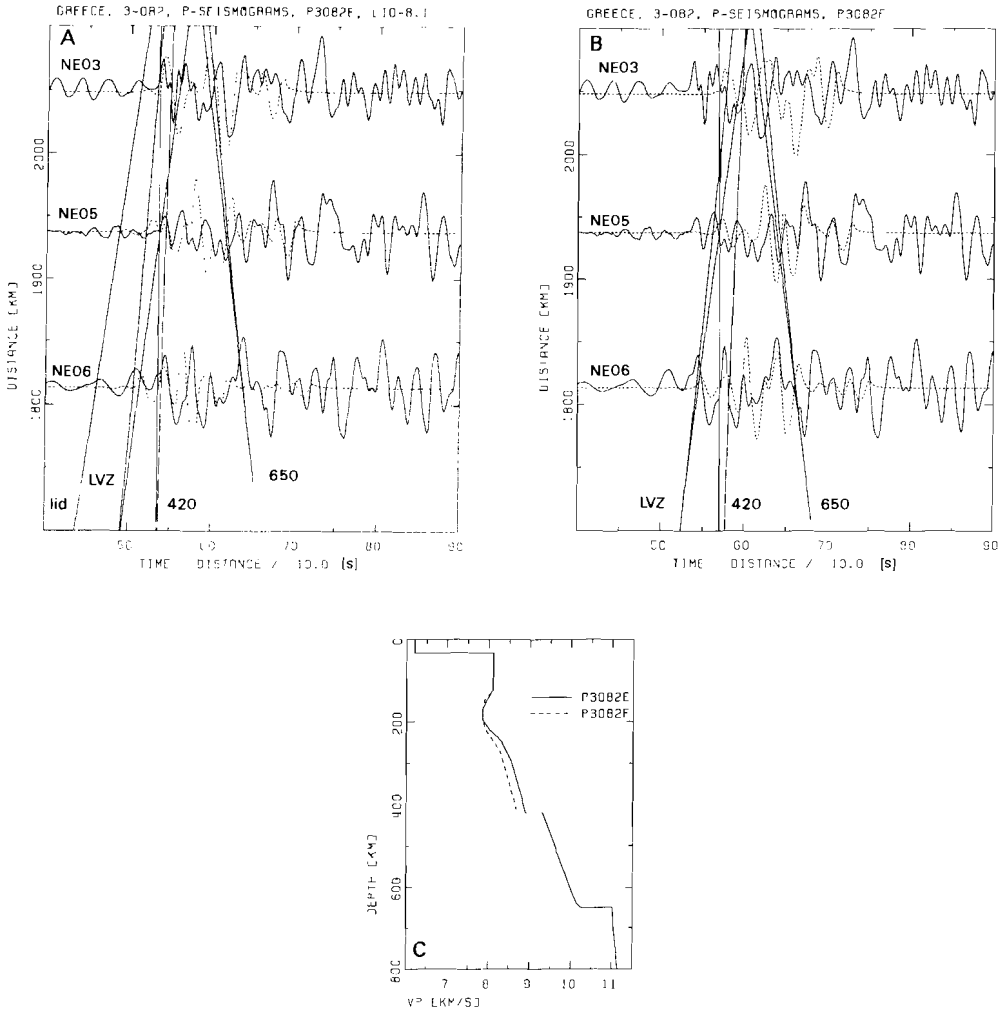


**Figure 17.** (a)  $P$ -wave data of event 3-082 (solid line) and synthetics for model P3082E with a lid velocity of  $8.1 \text{ km s}^{-1}$ . (b) Data and synthetics for model P3082F. (c) Velocity models P3082E with a lid velocity of  $8.1 \text{ km s}^{-1}$  and P3082F.

36 km difference in epicentral distance), and a bad fit is obtained for station NE02 (see Fig. 15a). A velocity distribution with a slightly higher velocities above the 400-km discontinuity and a 20 km shallower discontinuity fits the data of NE02 well, but does not match the data of station NE05. Again it should be emphasized that in matching travel times there is a trade-off between the depth of a discontinuity and the velocity structure above the discontinuity. In this case it is clear that reflections from the 400-km discontinuity arrive earlier for a ray-path to a station in the north than for a ray-path to a more southerly station. Notice that the same result was obtained for the shear-wave velocity structure. The seismograms of this event require the most pronounced LVZ of the  $P$ -wave dataset, and this can be the reason why the  $Pn$ -phase is only observed for this event.

$P$ -wave data of event 4-042 are recorded in two stations in Scandinavia (NE02 and NE03), and one in France (NE07). The  $P$ -wavetrain of the seismogram of NE07 is matched



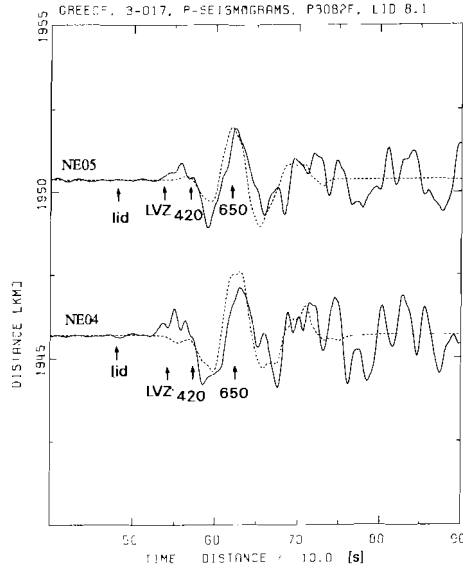


**Figure 18.** *P*-wave data of event 3-017 (solid line) and synthetics for model P3082F with a lid velocity of  $8.1 \text{ km s}^{-1}$ .

adequately by a model that has a high-velocity lid ( $8.1 \text{ km s}^{-1}$ ), a LVZ ( $120\text{--}300 \text{ km}$ ,  $\min, \nu_p = 7.85 \text{ km s}^{-1}$ ), velocities below the LVZ which are 2.5 per cent lower than the model for event 3-186 (or models K8 and T9), and two discontinuities at 420 and 650 km (see Fig. 16a). This model does not give a good agreement between data and synthetics of the other two stations. A better fit to the seismogram of NE03 is obtained by higher velocities below the lid (see Fig. 16b), but this velocity distribution still does not model the data of NE02 adequately. The velocity structure below the LVZ of the model for NE03 corresponds to that of event 3-186.

The *P*-wavetrain of event 3-082 recorded by station NE03 is reasonably well matched by the model which was determined for event 4-042 for this station (Fig. 17a). The data of station NE06, however, are better modelled by the velocity structure that was obtained for the seismogram of NE07 for event 4-042 but with a slightly lower velocity lid (see Fig. 17b).

The two seismograms of event 3-017, which has approximately the same hypocentre as event 3-082, are also well modelled by the velocity distribution of event 4-042 to station NE07 (Fig. 18). As for the *S*-wave modelling, the fault plane solution has been used instead of the centroid moment tensor. The take-off angles of the *P*-phases are close to one of the nodal planes, which is not resolved accurately enough to model the first onset of station NE05 with the correct sign. The travel times, however, are satisfactorily matched, suggesting that the velocity model is adequate.

#### SEISMOGRAMS WITH EPICENTRAL DISTANCES LARGER THAN $20^\circ$

The seismograms with an epicentral distance greater than  $20^\circ$  have been used to investigate the structure below the 400-km discontinuity. The model which was determined for the data of station NE03 for the events 3-082 and 4-042 gives a good fit to the seismograms of NE04

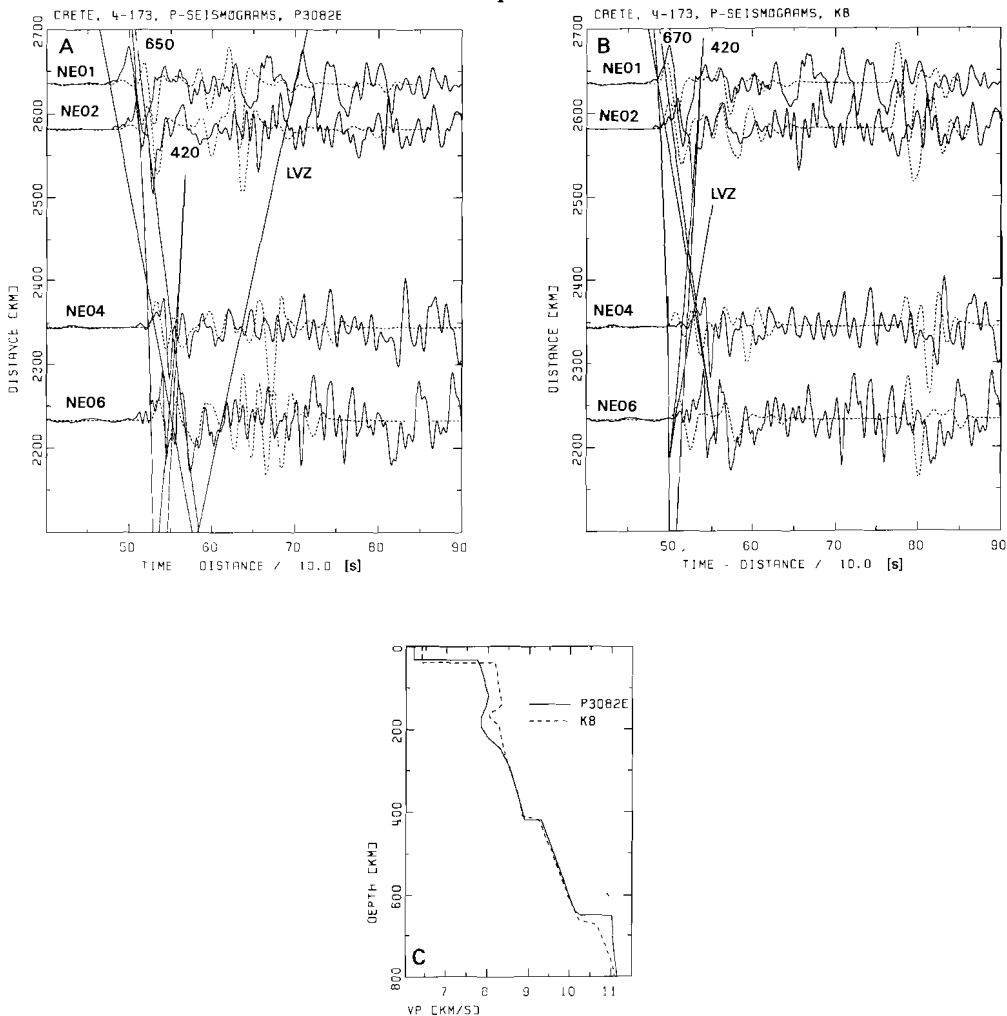


**Figure 19.** (a) *P*-wave data of event 4-173 (solid line) and synthetics for model P3082E. (b) Data and synthetics for model K8. (c) Velocity models P3082E and K8.

and NE06 of events 4-173 (see Fig. 19a). The travel times of the seismograms of event 2-229 of these two stations are also reasonably well matched by this model (see Fig. 20). The records of the stations NE01 and NE02 of event 4-173, however, are clearly better modelled by model K8 (Fig. 19b). This could be an indication for higher average velocities in the upper 250 km of the mantle along the ray-paths to the stations NE01 and NE02.

The model which gives a reasonable fit to most of the waveforms of the events 3-082, 4-042, and 4-173 does not match the data of event 5-270 (see Fig. 21a). One way to improve the fit is to assume higher velocities in the lid and LVZ without changing the velocity distribution at greater depths (Fig. 21b).

These results show that it is possible to match the *P*-wave arrival times by changes in the velocity structure above the 400-km discontinuity only. However, it should be emphasized that the resolution of the velocity structure below the 400-km discontinuity is not very high.

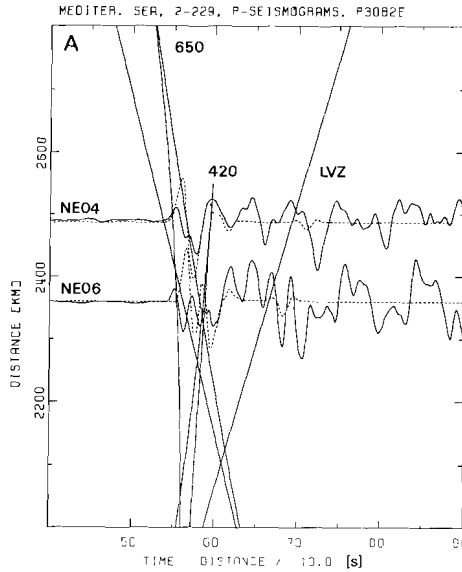
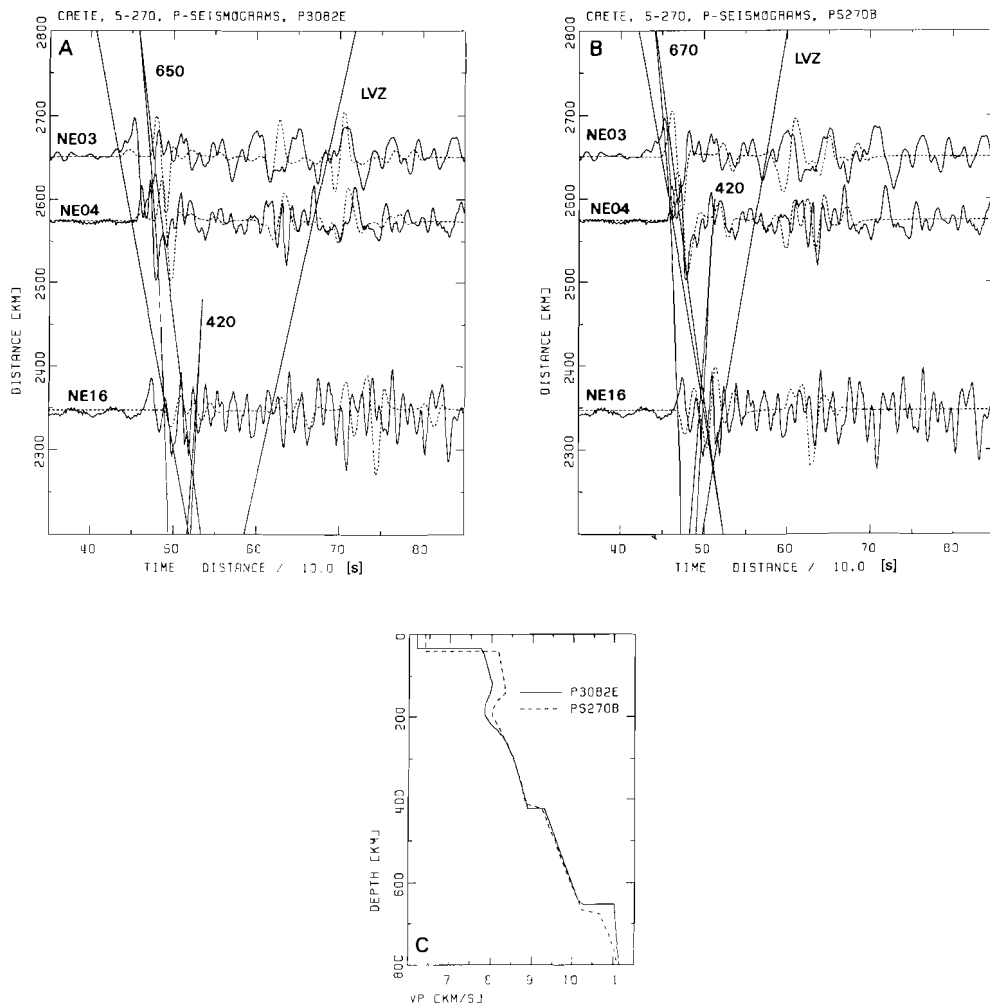


Figure 20. *P*-wave data of event 2-229 (solid line) and synthetics for model P3082E.

#### INTERPRETATION OF THE *P*-WAVE MODELLING RESULTS

The *P*-wave velocity structure for the region between the eastern Mediterranean and north-west Europe shows the same characteristics as the shear wave velocity distribution: a high-velocity lid ( $7.7\text{--}8.3\text{ km s}^{-1}$ ), a low-velocity zone (120–300 km) with minimum velocities varying between  $7.55$  and  $7.90\text{ km s}^{-1}$ , and two discontinuities at approximately 420 and 650 km depth. The average velocity model below 300 km is similar to the models K8 (Given & Helmberger 1980) and T9 (Burdick 1981), which are thought representative for a shield-like and a tectonic province, respectively. The velocity structure of the lid and the minimum velocity in the low-velocity zone show some variations, but the average values come close to those obtained by Mayer-Rosa & Mueller (1973): lid velocities ranging between  $8.1$  and  $8.2\text{ km s}^{-1}$ , and a minimum velocity of  $7.9\text{ km s}^{-1}$  at 200 km depth. Model EWK for Eurasia, which is determined by England, Worthington & King (1977) from travel-time and slowness measurements of earthquakes in the eastern Mediterranean and Adriatic regions, does not show a low-velocity zone. These authors note the low amplitudes of later arrivals between  $15^\circ$  and  $32^\circ$  and observe much more scatter in the travel times of the phases when compared with data from Russian events, but these elements are not reflected in their model.

This body wave analysis of broad band *P*-wave data presents evidence for heterogeneity in the *P*-wave velocity distribution of at least 2.5 per cent above the 400-km discontinuity. Several of the velocity variations which are inferred from the data are very well explained by the tectonic setting of the region which the phases cross. For example, the data of NE01 and NE02 are modelled by a velocity distribution with high velocities in lid and LVZ (event 4-173). These high velocities are obviously related to the structure of the Baltic Shield (see e.g. Husebye & Hovland 1982). Another striking observation is that low velocities between the lid and 400-km discontinuity are required to model the phases of events 3-017, 3-082, and 4-042 which cross the Adriatic Sea (paths to NE04, NE05, NE06, and NE07). The same observation was made for the shear wave structure and this feature is also recognized in a



**Figure 21.** (a) *P*-wave data of event 5-270 (solid line) and synthetics for model P3082E. (b) Data and synthetics for model P5270B. (c) Velocity models P3082E and P5270B.

tomographic inversion by Spakman (1986b). Undoubtedly, the high velocities in the upper 300 km which are obtained for the seismograms of event 5-270 are correlated with the cold subducted oceanic lithosphere beneath Crete. A profile of upper mantle *P*-wave velocity anomalies of this region shows this feature very clearly (Spakman 1986a, fig. 2). It is not possible to determine heterogeneity to depths greater than 400 km with this dataset due to its sparseness and the magnitude of the heterogeneity at shallower depths.

As for the *S*-wave velocity models, the *P*-wave velocity models show first-order discontinuities. This is because amplitude and frequency information have not been used in the modelling to constrain the thickness of the discontinuity. Moreover, it is not possible to determine the depths of the discontinuities with high accuracy due to the trade-off between the velocity structure above the discontinuity and the depth of the discontinuity itself. However, depths of 420 and 650 km generally give the best fit to the data for representative values of the velocity distribution below the low-velocity zone.

## 8 Conclusion

The upper mantle velocity structure beneath Europe has been investigated by modelling of body waves on broad-band seismograms. The data which have been used are *P*- and *SH*-waves of earthquakes in the eastern Mediterranean recorded by stations of the NARS array in north-west Europe. The seismograms have epicentral distances between 15° and 25°, and the phases sample the upper mantle to the 650-km discontinuity. It is not possible to model the *P*- and *S*-wavetrains of the seismograms adequately by a single *P*- or *S*-wave velocity distribution. However, some features are consistent for the different *P*- and *S*-wave velocity models: a high-velocity lid, a LVZ and two discontinuities at depths of approximately 420 and 650 km. The maximum depth of the lid is about 120 km and the velocities vary between 4.4 and 4.7 km s<sup>-1</sup>, and 7.7 and 8.3 km s<sup>-1</sup> for *P* and *S*, respectively. Minimum values of the velocities within the low-velocity zone range from 4.20 to 4.38 km s<sup>-1</sup>, and 7.55 to 7.90 km s<sup>-1</sup>, respectively. The data show evidence for velocity variations of at least a few per cent in the depth range from 300 to 400 km, but do not require large velocity anomalies at greater depths. Although one might question the validity of each of the 1-D models, it is observed that many of the inferred velocity variations are related to the tectonics of the region between source and receiver. The depths of the discontinuities are not resolved very accurately (> 10 km), due to the trade-off between the depth of the discontinuity and the velocity structure above the discontinuity, which is clearly heterogeneous. Small scale undulations of the 650-km discontinuity, such as suggested by Paulssen (1985), can therefore not be inferred by this kind of study.

Broad-band seismograms are essential for a detailed study of the upper mantle by body wave analysis. Separate arrivals within the wavetrain of phases generally cannot be identified on long-period seismograms, which reduces the resolution which can be obtained for the upper mantle structure. Short-period seismograms lack the low-frequency information which is needed for *S*-wave modelling, and contain a high amount of high-frequency signals which are not related to the average upper mantle structure. The results of this study show that it is possible to resolve upper-mantle lateral heterogeneity on a regional scale by a detailed analysis of body wave phases. In principle, it would even be possible to apply tomographic techniques to the wavetrains of upper mantle phases. Unfortunately, the number of broad-band seismograms is presently too small to allow such a 3-D inversion. However, when combined with other information, the data can help to improve the resolution of the 3-D upper mantle structure.

## Acknowledgments

I thank Professor C. Chapman for providing a version of his WKBJ program. I am also grateful to Guust Nolet for advice during this research and comments on a preliminary version of this paper. The Network of Autonomously Registering Seismographs (NARS) is the Dutch contribution to the European Geotraverse Project. It has been financed by AWON, the Earth Science branch of the Netherlands Organization for the Advancement of Pure Research (ZWO).

## References

- Anderson, D. L., 1979. The deep structure of continents, *J. geophys. Res.*, **84**, 7555–7560.
- Anderson, D. L., 1984. The Earth as a planet: paradigms and paradoxes, *Science*, **223**, 347–355.
- Burdick, L. B., 1981. A comparison of the upper mantle structure beneath North America and Europe, *J. geophys. Res.*, **86**, 5926–5936.

- Burdick, L. B. & Helmlberger, D. V., 1978. The upper mantle  $P$ -velocity structure of the western United States, *J. geophys. Res.*, **83**, 1699–1712.
- Cara, M., Necessian, A. & Nolet, G., 1980. New inferences from higher mode data in western Europe and northern Eurasia, *Geophys. J. R. astr. Soc.*, **61**, 459–478.
- Chapman, C. H., 1978. A new method for computing synthetic seismograms, *Geophys. J. R. astr. Soc.*, **54**, 481–518.
- Chapman, C. H. & Orcutt, J. A., 1985. The computation of body wave synthetic seismograms in laterally homogeneous media, *Rev. Geophys.*, **23**, 105–163.
- Dost, B., 1986. Preliminary results from higher mode surface wave measurements in western Europe under the NARS array, *Tectonophys.*, **128**, 289–301.
- Dost, B., van Wettum, A. & Nolet, G., 1984. The NARS array, *Geologie Mijnb.*, **63**, 381–386.
- Dziewonski, A. M. & Anderson, D. L., 1981. Preliminary reference Earth model, *Phys. Earth planet. Int.*, **25**, 297–356.
- England, P. C., Wortlington, M. H. & King, D. W., 1977. Lateral variations in the structure of the upper mantle beneath Eurasia, *Geophys. J. R. astr. Soc.*, **48**, 71–79.
- Gilbert, F. & Dziewonski, A. M., 1975. An application of normal mode theory to the retrieval of structural parameters and source mechanisms from seismic spectra, *Phil. Trans. R. Soc. A*, **278**, 187–269.
- Given, J. W. & Helmlberger, D. V., 1980. Upper mantle structure of northwestern Eurasia, *J. geophys. Res.*, **85**, 7183–7194.
- Grand, S. P. & Helmlberger, D. V., 1984. Upper mantle shear structure of North America, *Geophys. J. R. astr. Soc.*, **76**, 399–438.
- Grand, S. P. & Helmlberger, D. V., 1985. Upper mantle shear structure beneath Asia from multi-bounce  $S$  waves, *Phys. Earth planet. Int.*, **41**, 154–169.
- Helmlberger, D. V. & Engen, G. R., 1974. Upper mantle shear structure, *J. geophys. Res.*, **79**, 4017–4028.
- Husebye, J. & Hovland, E. S., 1982. On upper mantle seismic heterogeneities beneath Fennoscandia, *Tectonophys.*, **90**, 1–17.
- Ingate, S. F., Ha, J. & Muirhead, K. J., 1986. Limitations of waveform modelling of long-period seismograms, *Geophys. J. R. astr. Soc.*, **86**, 57–61.
- Jordan, T. H., 1978. Composition and development of the continental tectosphere, *Nature*, **274**, 544–548.
- Leven, J. H., 1985. The application of synthetic seismograms to the interpretation of the upper mantle  $P$ -wave velocity structure in northern Australia, *Phys. Earth planet. Int.*, **38**, 9–27.
- Lyon-Caen, H., 1986. Comparison of the upper mantle shear wave velocity structure of the Indian Shield and the Tibetan Plateau and tectonic implications, *Geophys. J. R. astr. Soc.*, **86**, 727–749.
- Mayer-Rosa, D. & Mueller, St., 1973. The gross velocity–depth distribution of  $P$ - and  $S$ -waves in the upper mantle of Europe from earthquake observations, *J. Geophys.*, **39**, 395–410.
- McKenzie, D., 1972. Active tectonics of the Mediterranean region, *Geophys. J. R. astr. Soc.*, **30**, 109–185.
- Nolet, G., 1977. The upper mantle under western Europe inferred from the dispersion of Rayleigh modes, *J. Geophys.*, **43**, 265–285.
- Nolet, G. & Vlaar, N. J., 1982. The NARS project: probing the Earth's interior with a large seismic antenna, *Terra Cognita*, **2**, 17–25.
- Nolet, G., Panza, G. F. & Wortel, R., 1978. An averaged model for the Adriatic Subplate, *Pageoph*, **116**, 1284–1298.
- Nolet, G., Dost, B. & Paulssen, H., 1986. The upper mantle under Europe: an interpretation of some preliminary results from the NARS project, *Geologie Mijnb.*, **65**, 155–165.
- Paulssen, H., 1985. Upper mantle converted waves beneath the NARS array, *Geophys. Res. Lett.*, **12**, 709–712.
- Ringwood, A., 1975. *Composition and Petrology of the Earth's Mantle*, McGraw-Hill, New York.
- Spakman, W., 1986a. Subduction beneath Eurasia in connection with the Mesozoic Tethys., *Geologie Mijnb.*, **65**, 145–153.
- Spakman, W., 1986b. The upper mantle structure in the Central European–Mediterranean region, in *European Geotraverse (EGT) Project, the central segment*, pp. 215–222, eds Freeman, R., Mueller, St & Giese, P.
- Vlaar, N. J., 1983. Thermal anomalies and magmatism due to lithospheric doubling and shifting, *Earth planet. Sci. Lett.*, **65**, 322–330.
- Walck, M. C., 1984. The  $P$ -wave upper mantle structure beneath an active spreading centre: the Gulf of California, *Geophys. J. R. astr. Soc.*, **76**, 697–723.

- Walck, M. C., 1985. The upper mantle beneath the north-east Pacific rim: a comparison with the Gulf of California, *Geophys. J. R. astr. Soc.*, **81**, 243–276.
- Woodhouse, J. H. & Dziewonski, A. M., 1984. Mapping the upper mantle: three-dimensional modeling of Earth structure by inversion of seismic waveforms, *J. geophys. Res.*, **89**, 5953–5986.

## Chapter 5

# Seismological evidence on the upper mantle discontinuities

Direct information of the upper mantle discontinuities can be derived from seismological data. The seismic velocity and density contrasts across the transitions, as well as the depth and width of discontinuities are properties that are valuable to constrain models of the Earth's upper mantle.

In this chapter an overview is given of the seismological observations that have contributed to our present knowledge of the two upper mantle discontinuities (section 5.1). This chapter further presents the results of a study of upper mantle P-to-S converted waves that provides unambiguous evidence for a locally sharp 670-km discontinuity (section 5.2).

### 5.1 AN OVERVIEW

Seismological data that provide information about the upper mantle discontinuities can be classified in essentially two categories: seismograms with phases that sample the transitions by near-grazing incidence (regional data), and seismograms with waves that sample the transitions locally under near-vertical incidence. Section 5.1.1 presents a summary of the evidence inferred from regional P and S body wave studies, and section 5.1.2 gives an outline of the information obtained from studies of upper mantle reflected and converted waves.

---

Apart from a few minor additions sections 5.1.2 and 5.2 of this chapter are accepted for publication as:

Paulssen, H., Evidence for a sharp 670-km discontinuity as inferred from P-to-S converted waves, *J. Geophys. Res.*, *in press*, 1988.



### 5.1.1 Travel time and waveform analyses

All regional velocity-depth models published in the two last decades, which are derived from travel time data or by waveform modelling, show two sharp velocity increases that are commonly referred to as the 400- and 670-km discontinuity. For simplicity, these transitions are generally displayed as first order discontinuities, but it should be emphasized that the data do not constrain these features with more resolution than 10 or 20 km (see e.g. Walck, 1984; Ingate et al., 1986). Variations in the depth of the discontinuities among these different (regional) models (see Nolet & Wortel, 1988 for a review) could reflect some genuine topography of these boundaries. On the other hand, there are substantial uncertainties in the depths of these transitions in the different velocity models. The velocity structure above the transition very must be known with a high accuracy in order to constrain the depth of the discontinuity with a high precision from travel times. As this is often not the case (it requires a large amount of data with phases that have their turning point just above the transition), it is likely that at least part of the depth variations among these models are artefacts of the interpretation.

The inferred velocity (and density) contrasts across the transitions are of particular relevance for comparison with the values determined from high pressure and temperature mineral phases measured in the laboratory. The increase in compressional velocity across the 400-km and 670-km discontinuity is generally estimated to be in the range of 0.4 to 0.5 km/s. There are fewer models of the upper mantle shear velocity, but these models indicate that the shear-velocity increase across the 400-km discontinuity is about 0.25 km/s, and that of the 670-km discontinuity is approximately 0.40 km/s.

### 5.1.2 Reflected and converted phases

Other evidence of the upper mantle discontinuities has been inferred from phases reflected or converted (from P to S, or S to P) at the transitions.

Precursors of PKPPKP ( $P'P'$ ) phases have been explained as underside reflections from the 400- or 670-km discontinuity, and they are generally denoted as  $P'400P'$  or  $P'670P'$  (in this notation  $P'P'$  would be  $P'0P'$ ). A sharp 670-km transition has been suggested from observations of  $P'670P'$  phases on short-period seismograms (Engdahl & Flinn, 1969; Whitcomb & Anderson, 1970; Adams, 1971; Bolt & Qamar, 1972; Teng & Tung, 1973; Fukao, 1977; Husebye et al., 1977; Nakanishi, 1986). Cleary (1981) questioned this interpretation and showed that such early precursors are also adequately explained by scattering of the PKKKP phase at the inside of the core-mantle boundary. More recently, Nakanishi (1986) argued that slowness estimates of the  $P'670P'$  phases of several studies are not in agreement with those expected for PKKKP scattered phases. The small width of the transition has been inferred from the fact that short-period  $P'670P'$  phases are indeed observed (assuming they are correctly interpreted). Richards (1972)

demonstrated that, to produce observable P'670P' phases on short-period seismograms, the thickness of the transition must be less than 4 km (for a horizontally layered medium). This value has often been adopted in studies of this kind, and similar theoretical results were obtained by Teng & Tung (1973), and Fukao (1977). However, Richards (1972) also pointed to the importance of (even a slight) curvature of the reflector on the amplitude of the P'670P' phase. In this regard, it is important to mention that P'670P' phases are not consistently observed (Husebye et al., 1977; Nakanishi, 1986). Furthermore, P'670P'/P'P' amplitude ratios vary among different studies (Teng & Tung, 1973). These observations can easily be explained in terms of focussing and defocussing effects of the discontinuity, although variations in the P'670P'/P'P' amplitude ratio may also occur when one phase is nearer to a caustic than the other. In both cases it is likely that predominantly high-amplitude P'670P' phases are observed, resulting in an overestimate of the reflectivity in the frequency band of short-period instruments, and, consequently, in an overestimate of the sharpness of the discontinuity (for acceptable values of the velocity contrast).

Observations of P'400P' phases on short-period seismograms have also been made, but they are relatively weak and appear less consistent than P'670P' phases (e.g. Nakanishi, 1988), which could indicate that the 400-km discontinuity is less sharp than the 670-km transition.

First-order multiple reflections ('reverberations') in the mantle of ScS phases (multiple ScS phases reflected once at one of the upper mantle discontinuities) have been used to determine the reflection coefficient (in the frequency band of long-period instruments) of the 670-km discontinuity for SH waves and the two-way (SH) travel time between the 400- and 670-km discontinuity beneath the western Pacific (Revenaugh & Jordan, 1987). However, these data do not constrain the fine structure of the discontinuities.

Finally, studies of S-to-P and P-to-S converted phases have been carried out to investigate the nature of the discontinuities. Most of these studies have made use of long-period seismograms (P-to-S converted phases: Vinnik, 1977; Kosarev et al., 1984; Souriau, 1986; Kind & Vinnik, 1988; S-to-P converted phases: Faber & Müller, 1980, 1984; Baumgardt & Alexander, 1984) that not only demonstrated the presence of converted phases from the 400- and 670-km discontinuity, but also showed that large amplitude variations exist among these phases. These long-period data lack the high frequency information needed to obtain a high (spatial) resolution of the discontinuities, and only a few studies of short-period near source S-to-P converted phases have been made (Barley et al., 1982; Bock & Ha, 1984; Richards & Wicks, 1987). These data suggest that the 670-km discontinuity is locally sharp beneath Tonga and Izu-Bonin, but also indicate that regional variations exist as systematic differences in the signal duration of the converted phases are recognized. However, these observations are not necessarily representative for an undisturbed upper mantle, since Tonga and Izu-Bonin are active regions of subduction, and the phases may even have converted at the subducted lithosphere itself.

Summarizing the results of these studies, we must conclude that phases reflected or converted at the upper mantle discontinuities are often, but only intermittently observed.

The observations on short-period seismograms could be suggestive of a locally sharp 670-km discontinuity, but this inference has been disputed by Muirhead (1985) who argued that none of the interpretations is without ambiguity. The results of our study of P-to-S converted phases on short-period and broad-band data (section 5.2) gives to this date the most global and unambiguous evidence for a locally sharp 670-km discontinuity. From these data it furthermore appears that the 670-km discontinuity is more pronounced than the 400-km discontinuity. These results have recently been confirmed in a study of P-to-S converted phases beneath the Gräfenberg array (Kind & Vinnik, 1988), a study of upper mantle  $P'dP'$  phases by Nakanishi (1988), and observations of ScS mantle reverberations (Revenaugh & Jordan, 1987).

## 5.2 EVIDENCE FOR A SHARP 670-KM DISCONTINUITY

This section presents the results of a study of P-to-S converted waves from the two upper mantle discontinuities. Several aspects are of relevance to such a study and some of this 'background' is presented in the following.

It is well-known that (for a laterally homogeneous medium) a P wave incident on an interface not only generates transmitted and reflected P waves, but also transmitted and reflected S waves (see fig. 5.1).

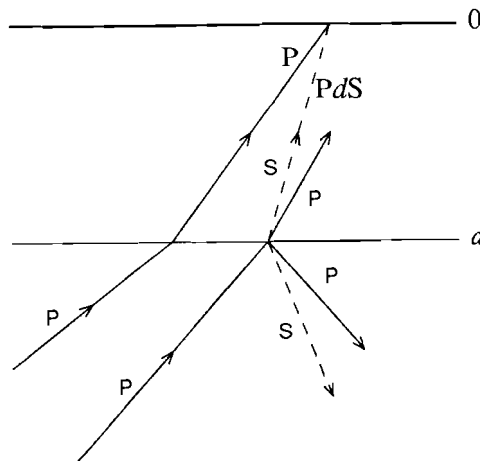


*Figure 5.1.* Ray geometry and notation of reflected, refracted, and converted waves generated by P waves incident on an interface at depth  $d$ . P waves are indicated by solid lines, S waves are dashed.

The P wave reflection coefficient and the conversion coefficients for the transmitted and reflected S waves are small for the velocity and density contrasts of the upper mantle discontinuities. Nevertheless, observations of upper mantle reflected and converted phases have been reported (see section 5.1.2). The transmitted phase which is converted at depth  $d$  and denoted  $Pds$  (see fig. 5.1), may be identified unambiguously by its SV polarization and travel time. Actually, any S wave arriving before the *direct* S phase must have been converted from P to S somewhere along its raypath. The time delay  $\tau$  between the direct P wave and the (slower) converted phase can be used to estimate the location of conversion (for a given velocity model). Furthermore, the P wave and the converted  $Pds$  wave arriving at the same location at the surface will have slightly different slownesses (see fig. 5.1). The values of the travel time difference  $\tau$ , the slowness difference  $\Delta p$ , and the ratio between the horizontal amplitude of the converted phase and the vertical amplitude of the P wave at  $72^\circ$ , are given in table 5.1 for conversions at the 400- and 670-km discontinuity (for reference Earth models PREM, Dziewonski & Anderson 1981, and 1066B, Gilbert & Dziewonski 1975).

Table 5.1: P-to-S converted phases ( $\Delta=72^\circ$ )			
400-km discontinuity			
model	$\tau$ (s)	$\Delta p$ (s/km)	$A_{rad}^P/A_{vert}^{P400s}$ (%)
PREM	42	-0.0007	2.3
1066B	44	-0.0005	2.7
670-km discontinuity			
model	$\tau$ (s)	$\Delta p$ (s/km)	$A_{rad}^P/A_{vert}^{P670s}$ (%)
PREM	68	-0.0013	5.2
1066B	69	-0.0013	8.2

Table 5.1 shows that the amplitudes of the upper mantle converted phases are small. Identification of the conversions is further hampered by the signal related 'noise' (the 'coda') of the P phase. It can be expected that stacking of the data for the appropriate slowness may enhance the signal-to-noise ratio of the  $Pds$  phase, whereas less coherent 'coda noise' is suppressed. Such a technique (more accurately described in section 5.2.2) has therefore been applied to the data selected for this study.

### 5.2.1 Introduction

The 400- and 670-km discontinuity mark the upper and lower boundary of the transition zone between upper and lower mantle. It should be kept in mind that the actual

depths of the discontinuities, generally not very well constrained, may differ from the values suggested by their names. In spite of the large number of studies on the upper mantle velocity structure, there is still no consensus about the nature of these two discontinuities. They can be related to phase transformations in olivine-rich mineral assemblages as well as to a change in chemical composition. Accurate seismological data are required in order to discriminate between these two possibilities, and to constrain petrological models of the upper mantle. So far, the (depth) resolution inferred from *refracted* seismic waves in the 15° to 30° epicentral distance range has proven insufficient to distinguish between a (presumably gradual) phase transformation and a (sharp) change in chemical composition. Detailed information on the sharpness of the discontinuities, which is the most important parameter to discriminate between the two, can be obtained from upper mantle reflected and converted waves, because they sample the discontinuities locally with relatively short wavelengths. A serious drawback of these phases is that they are generally of low amplitude.

In this study the upper mantle discontinuities are investigated with near-station P-to-S converted waves from teleseismic events. These phases arrive in the coda of the direct P wave and have the polarization of teleseismic SV waves. Since the travel time of these waves is much less than that of the direct S wave, any SV-polarized wave in the coda must have been converted. Thus, contrary to other waves that have been studied, such as S-to-P conversions or underside reflections like P'670P', their identification is not in doubt. The locality of conversion (the depth of the discontinuity) is constrained by the time delay with respect to P. In this study, the signal-to-noise ratio of the low amplitude converted phases is increased by stacking the seismograms of different events for a single station, which not only enhances the near-receiver phases 'generated' near the station, but also allows an estimate of the coherence of the signal.

It is shown that coherent energy, originating from the upper mantle beneath the station, arrives in the time interval of 40 to 80 s after the P phase. Arrivals with an SV polarization, and a delay and slowness consistent with an interpretation of a P-to-S converted wave from the 670-km discontinuity (P670s phase), can be identified for several of the stations used in this study. These include five of the broad-band stations of the NARS array, the five short-period RSTN (Regional Seismic Test Network) stations in the U.S., and the short-period SRO station CHTO (Thailand). The results of this study not only confirm the results of previous investigations (Vinnik, 1977; Kosarev et al., 1984), but also complement these with high frequency information, presenting evidence for a locally sharp 670-km discontinuity. The P670s arrivals observed for the stations of the NARS array are variable in signature, which may reflect a complex nature of the 670-km transition or a high degree of lateral heterogeneity beneath the stations. Upper mantle P-to-S converted waves from the 400-km discontinuity (P400s) are less consistently observed, and the data of this study suggest that this transition is less sharp or of smaller velocity contrast than the 670-km discontinuity.

### 5.2.2 Data selection and method of analysis

The data which have been used for this study are obtained from GDSN event tapes covering the period January 1985 - May 1986, and from NARS event tapes of the interval January 1983 - April 1987. The data have been selected according to the following criteria:

1. Only short-period and broad-band data are considered. Long-period seismograms are discarded because of the inherent limitations in attainable resolution.
2. No primary phases must arrive in the time interval of interest. This interval starts at about 40 s after the direct P wave when the amplitude of the crustal phases is negligible. To avoid interference with phases such as PP and PcP only teleseismic events are analysed ( $65^\circ < \Delta < 90^\circ$ ), and to prevent interference with pP and sP arrivals, only shallow ( $< 80$  km) and deep ( $> 400$  km) events have been used.
3. The available length of the seismograms must extend to a least 80 s after the P arrival to allow a possible identification of P-to-S converted phases from the 670-km discontinuity (P670s).
4. The data must have a high signal-to-noise ratio and a clear P onset, which are checked by visual inspection.

Furthermore, the number of seismograms per station must be sufficient to guarantee a reliable interpretation of the near-receiver phases of the P wave coda. This is the case for the short-period data of the 5 RSTN stations and SRO station CHTO (Thailand) with 15-47 seismograms per station, and for the broad-band data of 5 NARS stations with 17-48 seismograms per station (stations NE04, NE05, NE06, NE15, and NE16).

To allow an unambiguous interpretation of the near-receiver phases the data have been stacked. The stacking technique is essentially a  $\tau$ - $\Delta p$ -stack, where  $\tau$  in this case is the differential time with respect to the P phase and  $\Delta p$  the slowness difference with the direct P wave. The three components (vertical, radial, and transverse) of each seismogram are crosscorrelated with the waveform of the P phase on the vertical. The data are then normalized with respect to the autocorrelation of the P phase to give each seismogram equal weight. After that, the data are stacked using reference values of  $\tau$  and  $\Delta p$  appropriate for a P wave arriving at an epicentral distance of  $72^\circ$  for the data of the RSTN stations and station CHTO, and at  $80^\circ$  for the NARS data. These two values are approximately the mean values of the distribution of epicentral distances per station, and yield an optimum slowness resolution. The mean and standard deviation ( $\sigma$ ) of the stack (as a function of time) are calculated to obtain an estimate of the coherence in the stacked signal. Assuming a Gaussian distribution, the 95% confidence level of the signal (mean  $\pm 2\sigma$ ) can then be determined, allowing for an easy interpretation of the statistical significance of the stacked data. As an example, the  $\tau$ - $\Delta p$ -diagram of the radial component of station RSCP with an indication of the 95% confidence interval (reflected in the width of the trace) is shown in fig. 5.2. Similar diagrams have been used to analyse the vertical, radial, and transverse component of the P wave coda of the stations.

Phases for which the mean stacked amplitude is larger than twice the standard

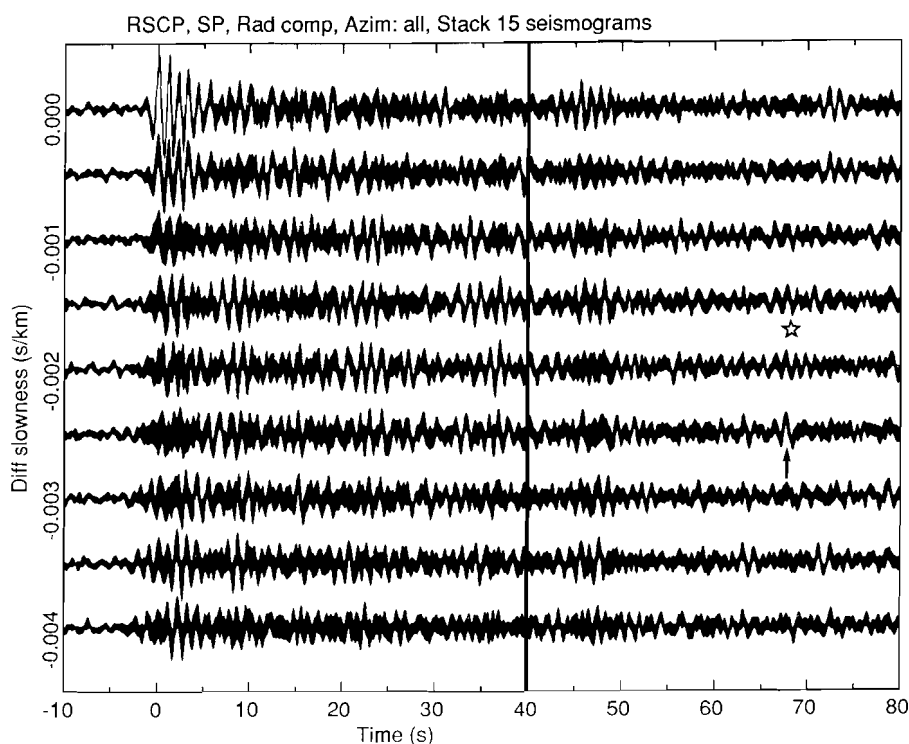


*Figure 5.2.*  $\tau$ - $\Delta p$ -stack of the radial component of the (correlated and normalized) seismograms of station RSCP (for an epicentral distance of  $72^\circ$ ). Indicated by the width of the trace is the mean  $\pm 2$  times the standard deviation (95% confidence interval) for each differential slowness relative to that of the direct P wave. The arrow points to a clear SV-arrival, and the star to the theoretical arrival of the P670s phase according to model 1066B. No primary phases arrive in the interval between 40 and 80 s the beginning of which is marked by the vertical line.

deviation at that time are interpreted as 'significant'. In this respect, it is important to know that the standard deviation of the short-period and broad-band stacks generally is 1.5-3% of the amplitude of the P phase on the vertical in the 40-80 s interval. Arrivals with an amplitude smaller than about 3-6% of the direct P wave are therefore not expected to be resolved using the 95% confidence criterion. Phases have been interpreted as P-to-S conversions when 'arrivals' on the radial component are not in phase with the signal on the vertical component, i.e. do not have a longitudinal polarization.

The technique enhances all signals, on each of the three components, that are similar to the waveform of the P wave, and may therefore be used to investigate all phases that correlate strongly with the P-pulse. In most cases, the P-pulse has been defined by the first 'sine-like' waveform, usually about 2-3 s long. The method has been found to be quite

robust with respect to the selected signal provided that its duration is not too long (about 5-6 s). This is probably due to the fact that crustal phases contaminate the P-waveform. The technique differs in this respect from the 'spectral ratio method' often used to study the crustal structure beneath a station (e.g. Phinney, 1964; Langston, 1979; Owens et al. 1987). In the spectral ratio method, 'receiver functions' for steeply incident P waves are obtained by the deconvolution of the radial component with the vertical component. It is then implicitly assumed that the vertical component contains the direct arrival (including source effects), but also most of the unwanted receiver crustal reverberations. The receiver function is therefore most sensitive to the crustal P-to-S converted phases, whereas reverberations are suppressed. This is an adequate technique for determining the crustal structure, but it is less satisfactory for the identification of (deep) upper mantle converted phases, because the incoming S (converted) phases are not affected in the same way by the crustal structure as the P wave. Hence, crustal multiples should preferably not be included in the 'source term' as they degrade the deconvolution for the upper mantle converted phase. Using the technique described above, crustal multiples are enhanced instead of suppressed because of their similarity with the P-pulse. This explains the large amplitude of the 'ringing' after the first P arrival as seen in fig. 5.2 for  $\Delta p = 0$  km/s. (This information could be useful to further constrain the crustal P-wave models inferred from station receiver functions that are most sensitive to the S-velocity structure.)

### 5.2.3 Observations of P-to-S converted phases from the 670-km discontinuity

Several 'arrivals' of coherent energy can be recognized on the stack of fig. 5.2, but most interesting is the wavelet at  $\tau=68$  s,  $\Delta p=-0.0025$  s/km that is the only prominent arrival with the character of a near-vertical incident SV-wave in the time interval of interest (see fig. 5.3(a)). The phase at 63 s for a differential slowness of  $-0.035$  s/km is clearly not an SV-arrival (see fig. 5.3(c)), whereas the phase at 71 s for the same differential slowness might be interpreted as a P-to-S conversion, although its polarization is more consistent with that of a P wave. The signal at  $\tau = 68$  s and  $\Delta p = -.0025$  s/km has a duration equal to that of the stacked P phase (at  $\Delta p=0$  s/km) and its amplitude is 15% of that of the P wave on the vertical. To investigate the significance of the phase in more detail, the data set of this station is divided into two sets with different backazimuth (azimuth from the station). Although more noisy, both subsets show the same SV-arrival (see fig. 5.3(b)), indicating that there is no (or little) azimuthal dependence of the signal.

Timing, amplitude, and polarization eliminate the possibility of a crustal origin of the phase. Furthermore, the arrival has a slowness smaller than that of the direct P wave, making an explanation as a crustal multiple more unlikely, as multiples have larger slownesses than the direct phase in a radially symmetric Earth. The polarization (near-vertical incident SV), and timing (coda of P wave) can only be explained by a phase converted from P to SV in the upper mantle beneath the station. Reference Earth models



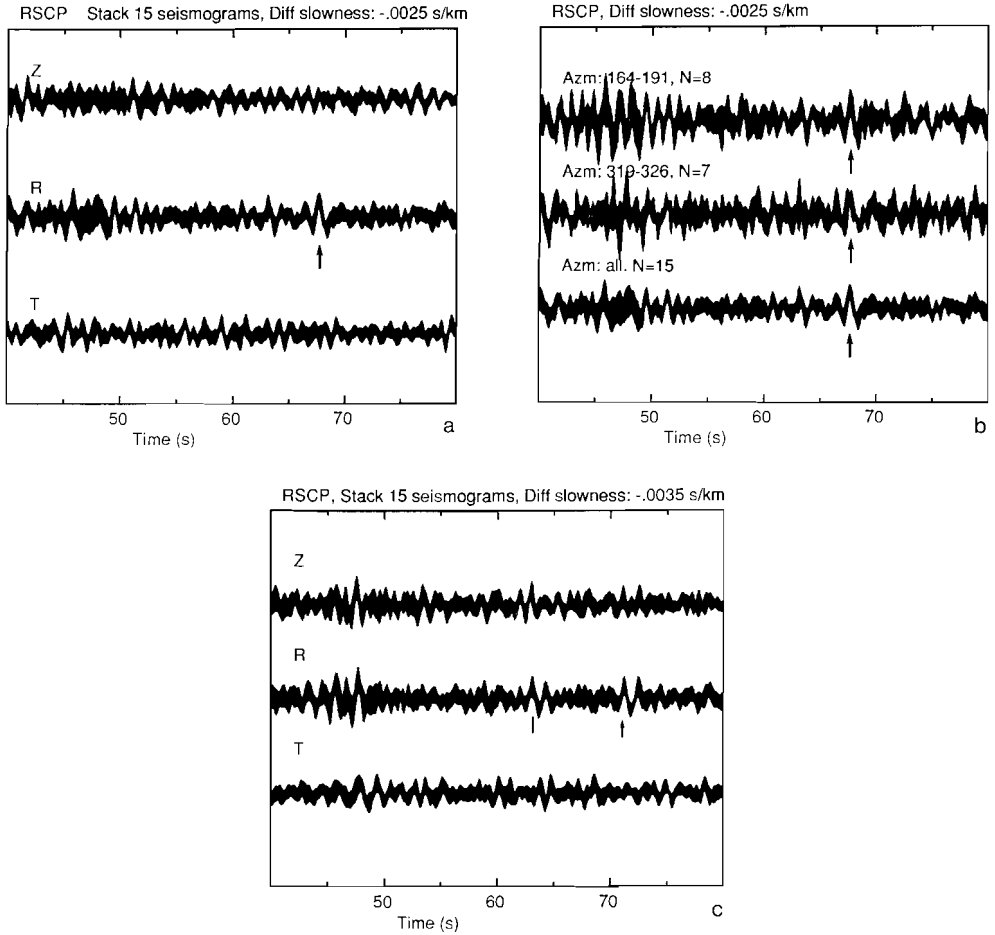


*Figure 5.3.* (a) 95% confidence interval of the stacked (correlated and normalized) seismograms of the vertical (Z), radial (R), and transverse (T) component of station RSCP for a differential slowness of  $-0.0025$  s/km.

(b) 95% confidence levels of the radial component of the stacked seismograms of station RSCP with a backazimuth of  $164-191^\circ$  (upper trace, 8 seismograms), with a backazimuth of  $319-326^\circ$  (middle trace, 7 seismograms), and of total dataset (lower trace).

(c) 95% confidence interval of the stacked (correlated and normalized) seismograms of the vertical (Z), radial (R), and transverse (T) component of station RSCP for a differential slowness of  $-0.0035$  s/km.

such as 1066B and PREM predict a delay of 68-69 s for a P-to-S conversion from the 670-km discontinuity (see table 5.1), suggesting that the phase is generated by the 670-km discontinuity. Its theoretical slowness is approximately  $0.0013$  s/km smaller than that of the P phase according to these models, a value slightly lower than estimated from the  $\tau$ -

$\Delta p$ -stack, but the arrival clearly has a negative differential slowness as is predicted for a P-to-S converted phase. The reference models do not explain the high amplitude (15% of direct P wave on the vertical) of the P670s phase as observed on the stack of station RSCP. Calculated by the WKB method (for perfectly elastic, radially symmetric media), PREM predicts an amplitude of 5.2% of that of the P phase. Model 1066B, with a relatively high velocity (10%) and density (7%) contrast across the 670-km discontinuity (see Nolet & Wortel, 1988, for an overview of upper mantle velocity models), gives an amplitude of 8.2% of that of the P phase. Obviously, the cause of the observed high amplitude must, at least partially, be sought in the structure beneath the station.

Conjectures that local effects contribute to a strong P670s phase at RSCP (Cumberland Plateau, Tennessee) are confirmed by inspection of the individual seismograms. Fig. 5.4 shows examples of seismograms with arrivals identified as P670s. Enlargements of the relevant portions of the data of fig. 5.4(b-d) can be found in fig. 5.5(a-c). The amplitudes of the phases on the (short-period or broad-band) radial component reach values as high as 45-65% of that of the P phase on the vertical, but are, except for the example of fig. 5.4(a), still at about noise level which makes them difficult to identify. A notable feature of these seismograms is that the energy on the radial component is generally nearly as high as that on the vertical, even for the *teleseismic* P waves. The cause of this high amplitude signal on the radial component is not yet clear, but it might be related to location of the station on a sedimentary layer (see Owens et al., 1984, for the crustal structure beneath RSCP; this model predicts a radial/vertical amplitude ratio of about 25% for a teleseismic P wave with  $\Delta = 72^\circ$ , which is clearly not consistent with the observations). Bouchon & Aki (1977) modeled the response of a sedimentary basin to a local earthquake for wavelengths which are close to the dimension of the geological structure and a strong amplification of the horizontal motions is their main result. Although the cause of the high amplitudes on the radial component is not yet fully understood, it is evident that the amplitudes of the P-to-S converted phases at RSCP may not simply be interpreted by an exceptionally high P-to-S conversion coefficient.

Another noteworthy feature of the high amplitude P670s phases is the similarity between the waveforms of the converted and the non-converted wave as shown in fig. 5.5(a-c). The resemblance of the P and P670s waveforms is striking, given the noise level of the data (judged by the differences in the vertical and radial component for the P phase). The similarity between the P and P670s phase is also made clear by comparison of the amplitude spectra of the phases of fig. 5.4(c) (seen in fig. 5.5(d)). The wavelet of the converted phase resembles that of the direct P phase at least up to frequencies of 2 Hz (station noise dominates at higher frequencies).

The short-period data of the other RSTN stations and station CHTO were analysed in detail to investigate whether the P670s phase could also be observed for these stations. However, the stacked seismograms of these stations did not yield equally conclusive results. There is some evidence for the presence of a P670s phase on the stacks of the stations RSON (Red Lake, Ontario), RSNT (Yellowknife, Northwest Territory), and RSSD

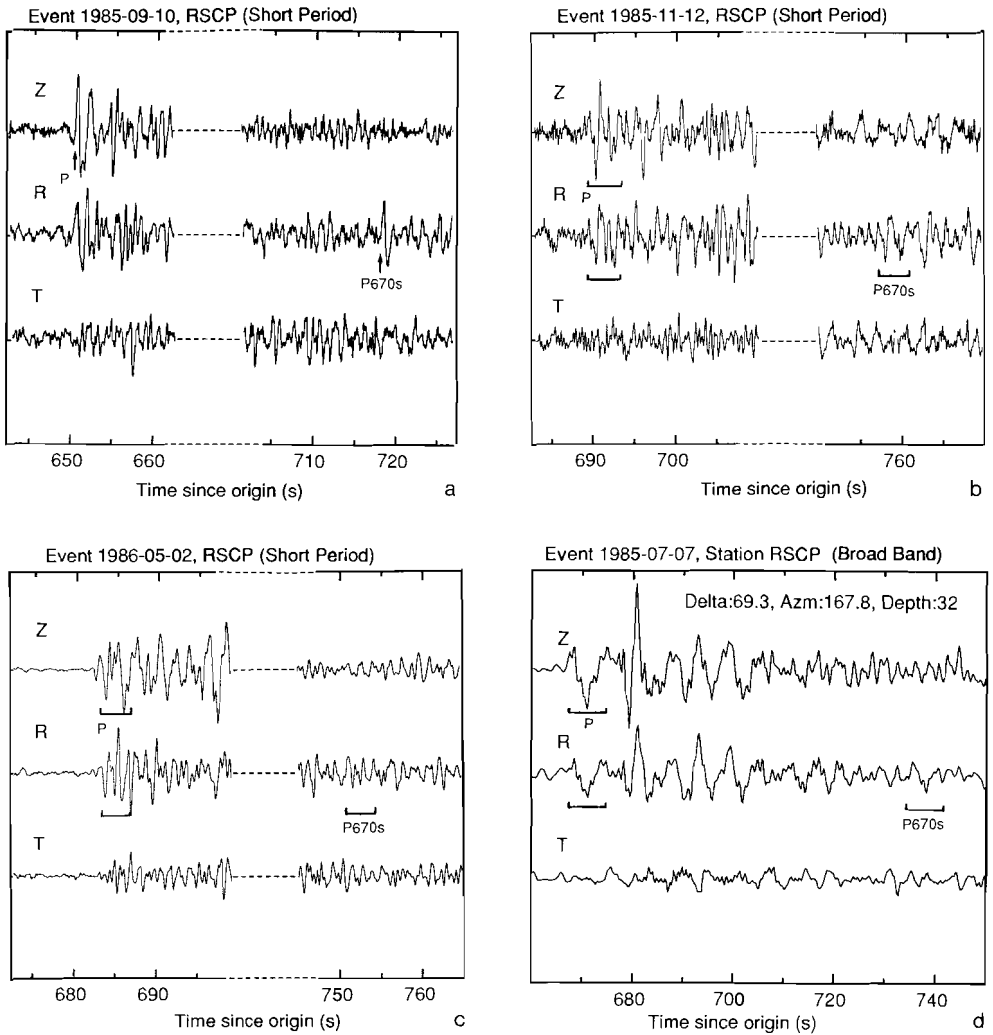


**Figure 5.4.** Vertical (Z), radial (R), and transverse (T) component of the short-period seismograms of stations RSCP of event

(a) 1985-09-10: Depth: 33 km, Back azimuth: 329°, Delta: 66.8°,

(b) 1985-11-12: Depth: 10 km, Back azimuth: 191°, Delta: 72.4°,

(c) 1986-05-02: Depth: 33 km, Back azimuth: 325°, Delta: 89.9°, and

(d) of the broad-band seismogram of event 1985-07-07: Depth: 32 km, Back azimuth: 167.8°, Delta: 69.3°.

(Black Hills, South Dakota), where the signal is just statistically significant within the 95% confidence level (see fig. 5.6(a-c)). At  $\tau = 70, 72,$  and  $69$  s the amplitudes of the stacked signal are 4.3, 4.5, and 5.0% of that of the P phase for RSON, RSNT, and RSSD,

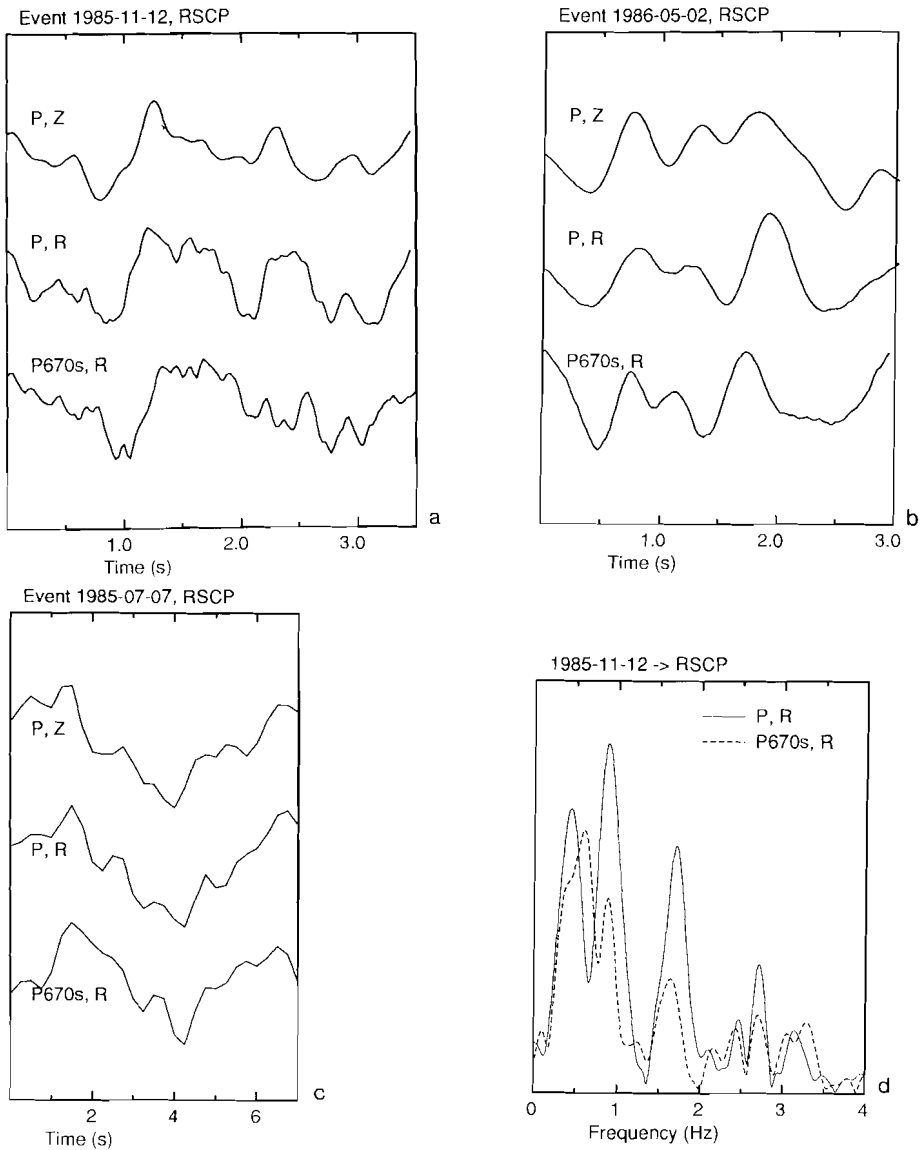


**Figure 5.5.** Waveforms of the direct P phase on the vertical and radial component (upper and middle trace), and of the P670s phase on the radial component (lower trace, 68 s shifted in time) of (a) event 1985-11-12 (cf. fig. 5.4b), (b) event 1986-05-02 (cf. fig. 5.4c), (c) event 1985-07-07 (cf. fig. 5.4d).

(d) Frequency content of the P waveform on radial component (solid line), and of the P670s phase on the radial (dashed) of event 1985-11-12. (Vertical scale is linear).

respectively, values that are in accordance with a PREM velocity contrast at 670 km. The interpretation of the data at RSSD is complicated by coherent signal on the vertical

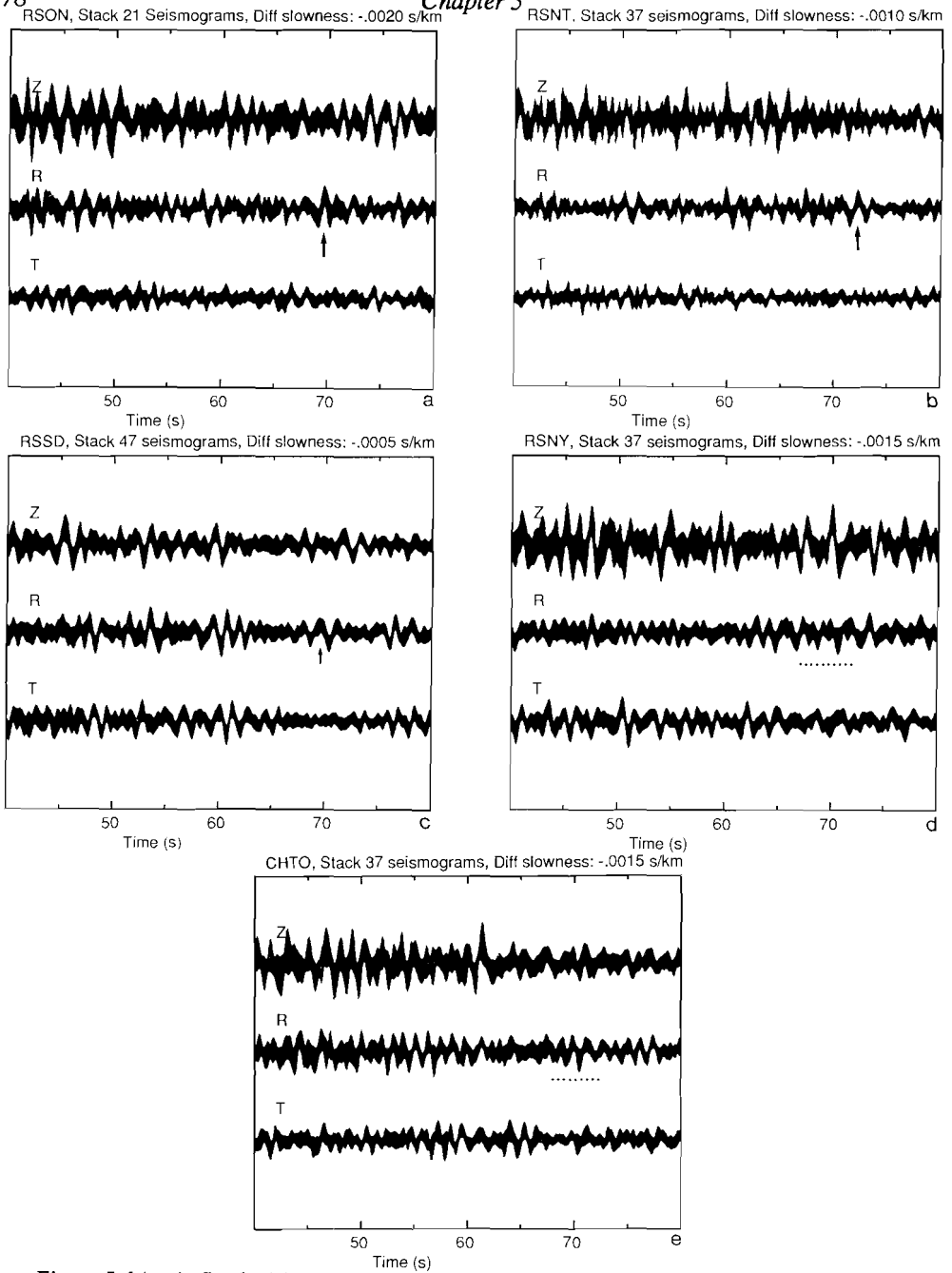


Figure 5.6 (a-e). Stacked (correlated and normalized) seismograms of the vertical (Z), radial (R), and transverse (T) component of the stations RSON, RSNT, RSSD, RSNY, CHTO, respectively. The number of seismograms, and differential slowness used for these stacks are indicated at the top of each diagram.

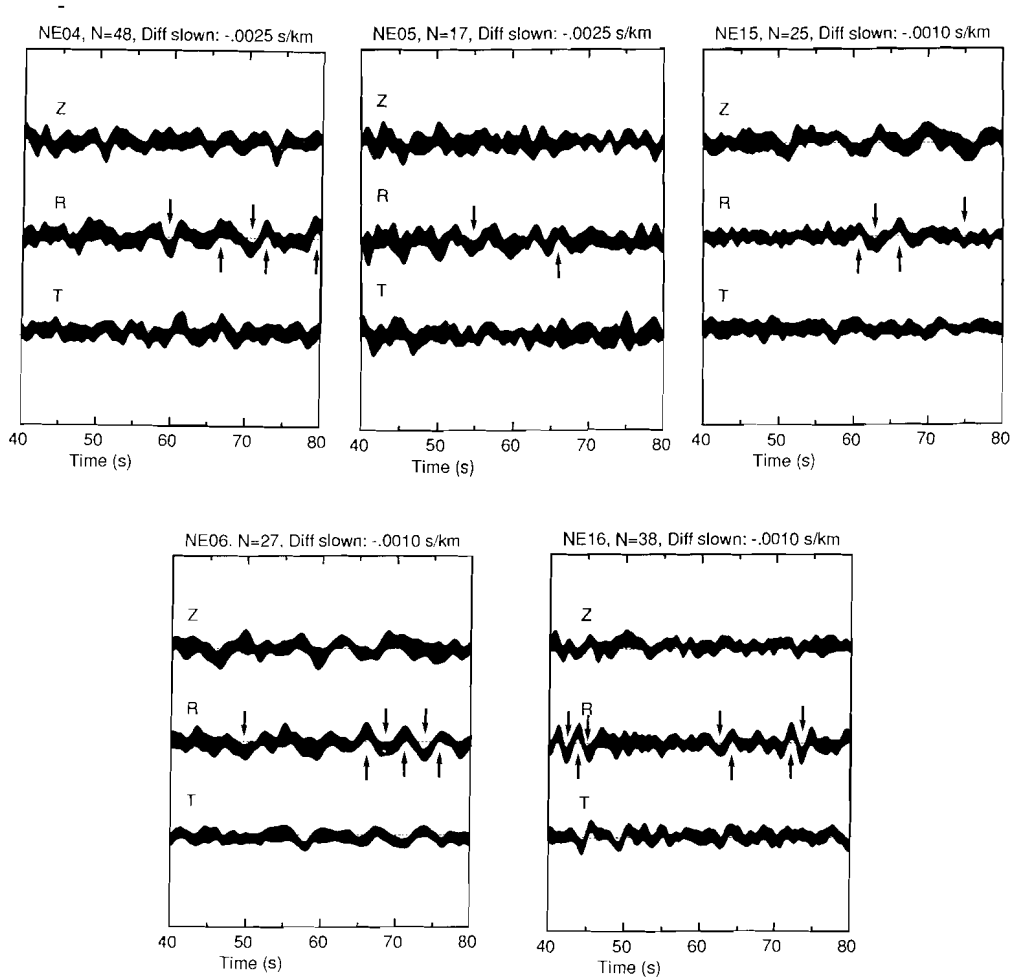
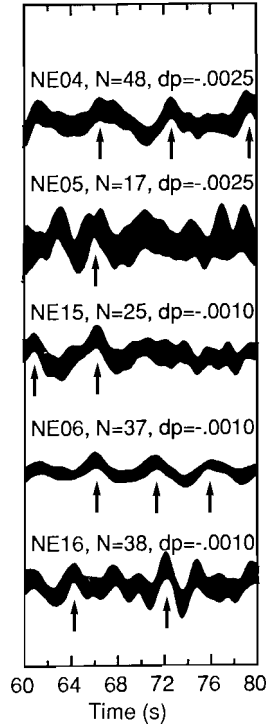


Figure 5.7. As figure 5.5 for the broad-band NARS stations NE04, NE05, NE15, NE06, and NE16. Arrows point to 'arrivals' on the radial component according to the 95% confidence criterion.

component just before and after the possible P670s arrival. Note also that there are high amplitude signals on the transverse component of this station, which is probably due to the pronounced lateral variations in the crustal structure beneath this station (Owens et al., 1987). There is no conclusive evidence for the presence of a P-to-S converted phase from the 670-km discontinuity on the stacked seismograms of station RSNY (Adirondacks, New York) and CHTO (Chiang Mai, Thailand), as can be seen from fig. 5.6(d-e).

Similar to the short-period data, the broad-band data of the NARS array give varying results regarding possible P670s arrivals. Fig. 5.7 presents diagrams of the stacked



*Figure 5.8.* 95% confidence intervals of the stacked signal on radial component for the NARS stations of this study. Station name, number of seismograms used for the stack, and differential slowness are indicated at the top of each trace. Arrows point to positive 'arrivals'.

seismograms of these stations, where the arrows point to '95% confidence arrivals' on the radial component. The data show a high degree of variability in the arrival times of possible SV phases, and in their 'signal-to-noise ratio' (the radial components have been drawn to the same scale in fig. 5.8). The most consistent arrival is observed for  $\tau = 66$  s, while another less coherent SV arrival might be recognized at a delay of approximately 72 s. In the following, we will therefore concentrate on these wavelets.

The stacked seismograms of station NE15 (Valkenburg, The Netherlands) show a clear SV arrival at  $\tau = 66$  s, with an estimated slowness of  $\Delta p = -0.0010$  s/km, and an amplitude which is 7.3% of the amplitude of the direct P phase on the vertical with a standard deviation of 2.4% ( $7.3 \pm 2.4$  %, this notation will be used in the following). The phase has a duration equal to that of the stacked P phase and is observed on different substacks of the data. It therefore seems to be a coherent phase, but it is difficult to identify on the individual seismograms. Apparently, the phase is generally not of high amplitude, except perhaps for the one shown in fig. 5.9(a) with a delay of 65 s. The other two stations

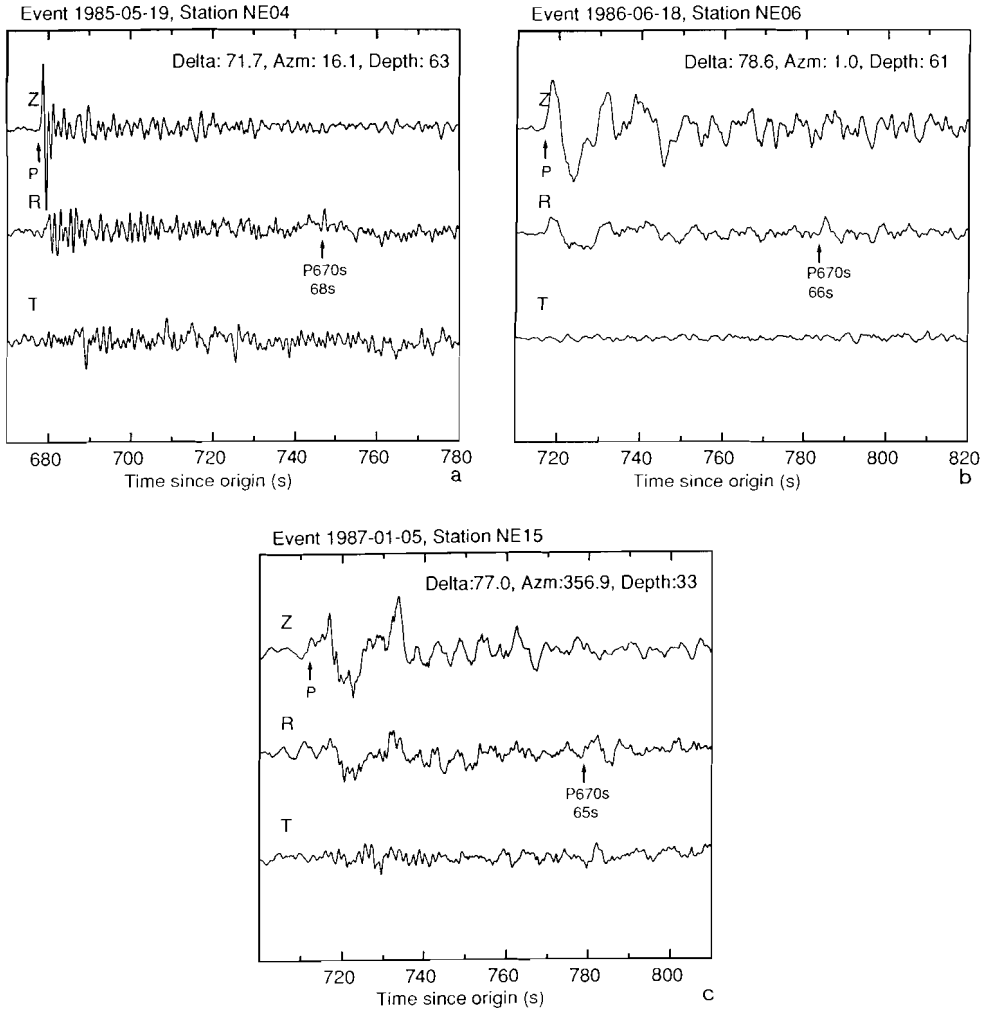


Figure 5.9 (a-c). Examples of P670s phases for different NARS stations in northwest Europe.

in the Netherlands (NE04 Witteveen, NE05 Utrecht) and station NE06 (Dourbes, Belgium) show at best poorly resolved SV waves at 66 s with amplitudes of about  $5.0 \pm 2.3\%$ . Examination of subsets of the data reveals that the arrival at 66 s is not consistently observed at NE04 and NE05 (see also Paulssen, 1985), but, although with smaller amplitude, appears more coherent at NE06. Inspection of the individual seismograms shows that clear arrivals with a consistent delay of approximately 66 s can be identified on some of the records. Fig. 5.9 shows examples of phases that have been interpreted as P-to-S conversions from the 670-km discontinuity for different NARS stations in northwest



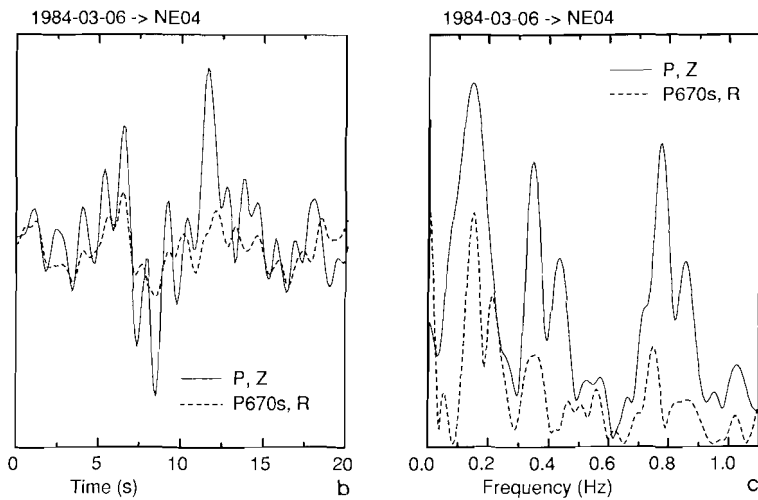
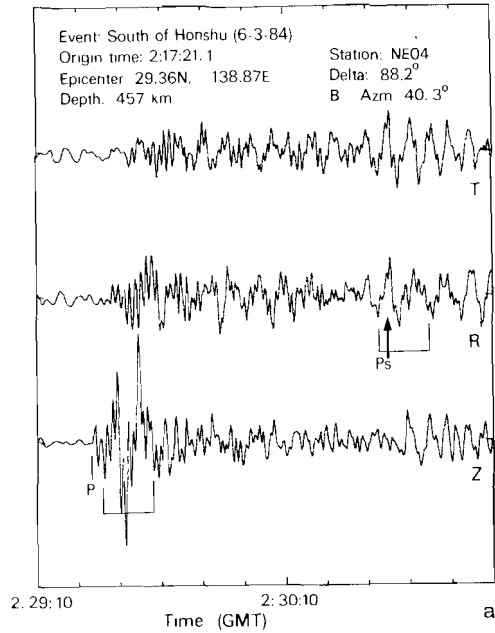


Figure 5.10. (a) Example of a P670s phase for station NE04.

(b) Waveform of the P phase on the vertical component (solid line) and the P670s phase on the radial component shifted by 66 s (dashed).

(c) Amplitude spectra of the P and P670s waveforms.

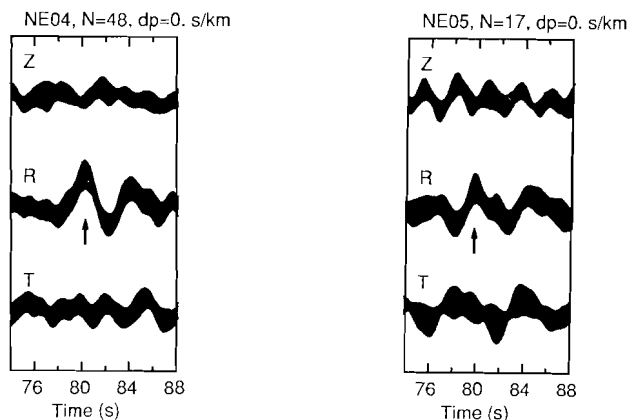
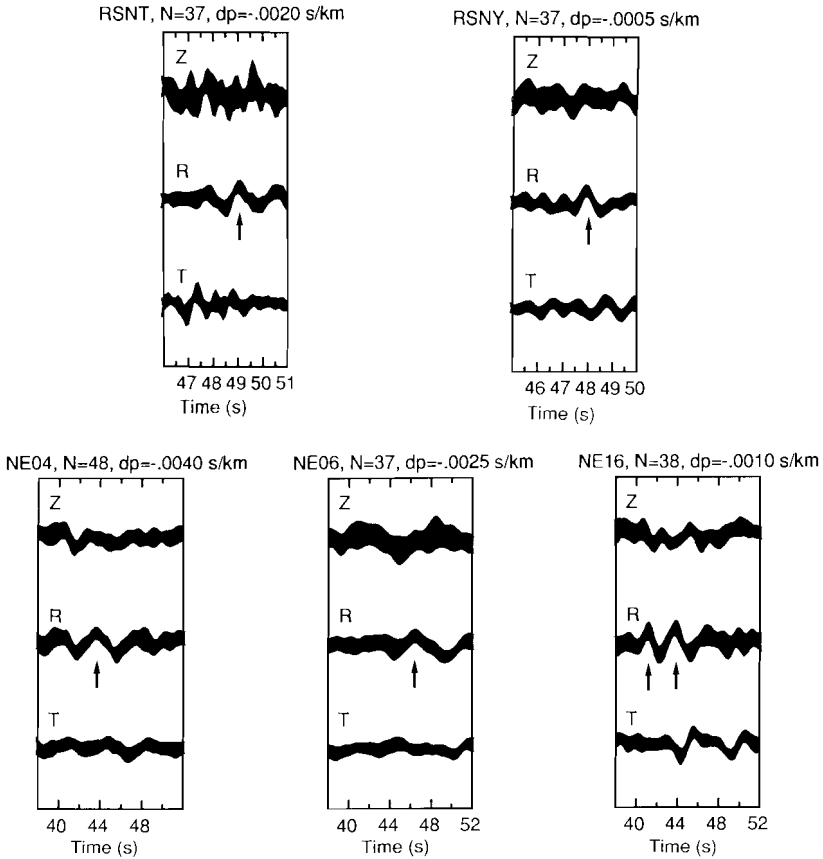


Figure 5.11. Stacked seismograms of NE04 and NE05 for  $\Delta p = 0$  s/km showing an SV arrival at  $\tau = 80$  s.

Europe. Fig. 5.10(a) has been taken from Paulssen (1985) to show the similarity (fig. 5.10(b)) for a long and high-frequency source time function. The converted and non-converted phase resemble each other up to a frequency of about 1 Hz, the cutoff-frequency of the NARS instrument response (see fig. 5.10(c)).

The most coherent signal with an SV character observed for station NE16 (Clermont Ferrand, France) is at the arrival at 72 s ( $\Delta p = -0.0010$  s/km,  $\text{ampl.} = 8.7 \pm 2.7$  %). However, the phase is not recognized on any of the individual seismograms due to the generally high amplitude ('noisy') coda of the data. A similar remark could be made for the arrival at 73 s for station NE04, although the 'coda noise' of this station is smaller in amplitude. The wavelet at 70-76 s observed for station NE06 is a feature of seismograms with a northeast backazimuth only. Although some of the seismograms of these stations show a high amplitude signal on the radial component at about 72-74 s after the P arrival, these cannot unambiguously be interpreted as upper mantle converted phases.

Another interesting feature, shown in fig. 5.11, is a very clear SV arrival at 80 s in the coda of NE04 for data with a backazimuth of about  $345^\circ$  to  $41^\circ$  ( $\Delta p = 0$  s/km,  $\text{ampl.} = 11.4 \pm 3.1$  %), and a similar but less clear phase for NE05 ( $\Delta p = 0$  s/km,  $\text{ampl.} = 10.1 \pm 4.6$  %) for which the available seismograms have a predominantly northeast backazimuth. The phase is not observed for any of the other stations, and is recognized on the seismograms of NE04 and NE05 by an increase in amplitude. Waveform comparisons with the direct P are not as convincing as for phases arriving at approximately 66 s, the phase generally being recognized by an increase of energy on the radial component. This, together with the estimated differential slowness of 0.0 s/km, and the limited number of stations and azimuthal range for which these observations are made, hampers the interpretation as simple upper mantle P-to-S converted waves.



*Figure 5.12.* Stacked seismograms with possible P-to-S conversions from the 400-km discontinuity.

#### 5.2.4 Observations of P-to-S converted phases from the 400-km discontinuity

The observations of the P670s phase stimulated a detailed investigation into the presence of other converted phases from the upper mantle. Although there is some evidence for the existence of other SV arrivals in the time window of 40 to 80 s after the P phase, none of these phases is very systematically observed. Most coherent and clear are the phases with a delay of 43–49 s. Two RSTN stations show an SV arrival at 48–49 s after the P phase (RSNY:  $\tau = 48$  s,  $\Delta p = -0.0005$  s/km,  $\text{ampl.} = 5.0 \pm 1.3\%$ ; RSNT:  $\tau = 49$  s,  $\Delta p = -0.0020$  s/km,  $\text{ampl.} = 4.5 \pm 1.2\%$ ), and three NARS stations show an SV phase with a delay of 44–46 s (NE04:  $\tau = 44$  s,  $\Delta p = -0.0040$  s/km,  $\text{ampl.} = 6.3 \pm 1.9\%$ ; NE06:  $\tau = 46$  s,  $\Delta p = -0.0025$  s/km,  $\text{ampl.} = 2.8 \pm 1.4\%$ ; NE16:  $\tau = 44$  s,  $\Delta p = -0.0005$  s/km,  $\text{ampl.} = 9.0 \pm 2.7\%$ ). Fig. 5.12 shows the 95% confidence intervals of these data. If these phases are

interpreted as P-to-S converted phases from the upper mantle they must be related to the 400-km discontinuity. Model PREM and 1066B predict delays of 42 and 44 s for discontinuities at depths of 400 and 420 km, respectively, and delays of 43 and 46 s if a more acceptable continental crust is incorporated. The differential slowness is -0.0007 s/km according to PREM and -0.0005 s/km for 1066B, and theoretical amplitudes are approximately 2.5% of the P wave. The amplitudes of the P400s phases are smaller than those of P670s phases, mainly because of a smaller velocity contrast in the two reference models at the 400-km discontinuity. Observations of P400s phases are indeed smaller in number than those of P670s phases, but the stacked amplitudes range from 2.8 to 9.0 %, values that are comparable to those of P670s phases. These variations in estimated amplitude, travel time, and slowness, point to lateral heterogeneity at or above the 400-km discontinuity. No clear P400s phases have been identified on individual seismograms, which could imply that there are no high-amplitude P400s phases, or that there is more waveform distortion than for the P670s phases. More data are needed to resolve this question, and to allow an interpretation in terms of the width and velocity contrast of the discontinuity.

### 5.2.5 Interpretation

In the previous section I showed that the stacked seismograms allow an identification of the upper mantle P-to-S converted phases beneath the seismic station if the signal-to-noise ratio is sufficiently increased by stacking. The amplitude estimates as obtained from the stacks should be interpreted as lower bounds of the 'true' mean amplitudes, since small travel time differences due to crustal and upper mantle heterogeneity beneath the station will reduce the amplitude of the stacked signal, especially for the short-period data. Furthermore, it should be kept in mind that the inferred differential slownesses are only estimates of which the resolution depends on the distribution of epicentral distances. The visually determined 'slowness resolution' of the  $\tau$ - $\Delta p$ -stacks is for all stations approximately 0.0005 s/km, except for RSON ( $\pm 0.0010$  s/km).

The results of this study show clear P-to-S converted phases from the 670-km discontinuity for the short-period data of station RSCP ( $\tau = 68$  s,  $\text{ampl.} = 13.7 \pm 3.6\%$ ,  $\Delta p = -0.0025$  s/km), and for the broad-band data of station NE15 ( $\tau = 66$  s,  $\text{ampl.} = 7.3 \pm 2.4\%$ ,  $\Delta p = -0.0010$  s/km) and NE16 ( $\tau = 72$  s,  $\text{ampl.} = 8.7 \pm 2.7\%$ ,  $\Delta p = -0.0010$  s/km).

Less clear are the P670s phases on the short-period stacks of RSON ( $\tau = 70$  s,  $\text{ampl.} = 4.3 \pm 1.7\%$ ,  $\Delta p = -0.0020$  s/km), RSNT ( $\tau = 72$  s,  $\text{ampl.} = 4.5 \pm 2.1\%$ ,  $\Delta p = -0.0010$  s/km), RSSD ( $\tau = 69$  s,  $\text{ampl.} = 5.1 \pm 2.5\%$ ,  $\Delta p = -0.0005$  s/km), and possibly the phase at RSCP ( $\tau = 71$  s,  $\text{ampl.} = 11.0 \pm 4.9\%$ ,  $\Delta p = -0.0035$  s/km). The other broad-band NARS stations present a picture of signals with an SV wave character between 66 and 76 s. These signals are just statistically significant within the 95% confidence limit, but it is difficult to trace their origin. The arrivals can be interpreted as conversions from interfaces at different

depths, but they can also be explained by lateral heterogeneity beneath the station, resulting in variations of the arrival times for phases generated by the 670-km discontinuity. The data of station NE06 seem to point in this direction as the wavelet between 70 and 76 s is a feature of data with a northeast backazimuth only. However, most clear P670s arrivals have been identified on seismograms of different NARS stations in northwest Europe with a delay of  $66 \pm 2$  s, and this arrival is more or less consistently observed on the stacks of these stations (NE04, NE05, NE15, and NE06) for different azimuths. The question of whether the later arrivals are due to different interfaces or to lateral heterogeneity cannot be resolved with this data set. The intermittent nature of observations of P-to-S converted phases from the 670-km discontinuity is further inferred from the short-period stacks of station RSNY and CHTO which do not show any evidence for such a phase exceeding the standard deviation of 1.3% and 1.9% respectively.

The identified P670s phases on the short-period and broad-band seismograms of station RSCP and on the broad-band seismograms of NARS stations show extremely high amplitudes that cannot be explained by (acceptable) radially symmetric upper mantle models. It is believed that the high amplitudes are at least partly caused by amplification effects in the local structure beneath the station. Supporting this view is the observation that clear P670s phases on individual seismograms are predominantly identified for stations located on sediments, which might imply that focussing effects of the sediment-basement interface play an important role. However, high-amplitude P670s phases can also result from focussing effects of other structures in the crust or upper mantle. In particular, focussing by warping of the 670-km discontinuity is very effective due to its large impedance contrast for P-to-S converted waves. The travel time and slowness variations as observed for the P670s phases are further suggestive for topography of the 670-km discontinuity, although effects of upper mantle heterogeneity may not be neglected. Since a large degree of upper mantle lateral heterogeneity is likely to be present beneath different regions (particularly for western Europe: Spakman et al., 1988; see also chapter 4), it is not appropriate to interpret the observed travel times, slownesses, and amplitudes in a quantitative way. Nevertheless, to get an idea of the magnitudes of the parameters involved, it is simply calculated that for a lens-shaped topography of the 670-km discontinuity a radius of curvature of about 1300 km is needed to double the amplitude of the converted phase (in an otherwise homogeneous upper mantle). This value corresponds to a change in depth of the transition of 15 km over a horizontal distance of 200 km, or, equivalently, to a travel time variation of about 1.5 s for the P670s phase.

More important for an interpretation of the nature of the 670-km discontinuity is the waveform similarity of the converted phases to the direct P wave. The waveforms of the converted phases resemble those of the P wave signal up to 1 Hz for the broad-band data (see figures 5.4(d), 5.9, and 5.10), and for the short-period data in one particular case even up to 2 Hz (fig. 5.5(d)). This implies that the 670-km discontinuity is, at least locally, extremely sharp. The transfer functions shown in fig. 5.13 display the frequency-dependent amplitude behaviour of converted phases for different widths of the discontinuity. They

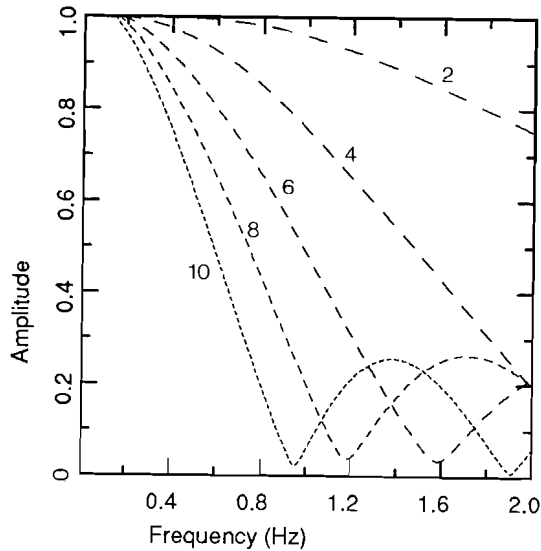


*Figure 5.13.* Transfer functions, of the frequency dependence of P670s phases for different widths of the discontinuity. The curves represent the (frequency dependent) amplitude ratio of phases converted at a transition of finite width compared to those converted at a first order discontinuity. Indicated for each curve is the width of the transition in km.

are calculated by the propagator matrix method, assuming a 'linear gradient' within the transition which is approximated by a sequence of layers with a thickness of 1 km each. Assuming that the high-frequency content has decayed by 40 to 50% relative to the low frequencies, it can be inferred that the width must be less than 5 to 6 km for waveform 'similarity' up to 1 Hz (beneath station NE04, fig. 5.10(c)), or less than 2.5 to 3 km for waveform 'similarity' up to 2 Hz (beneath station RSCP, fig. 5.5(d)). This observation has important implications for petrological and geodynamical models of the mantle (see discussion and chapter 6).

Observations of P-to-S converted waves from the 400-km discontinuity on the stacked seismograms are smaller in number, and no clear P400s phases have been identified on individual seismograms. This may indicate that there are no high amplitude P400s phases, or that there is more waveform distortion for the P400s phases than for the P670s phases. This last interpretation could imply that the 400-km discontinuity is less sharp than the 670-km discontinuity. However, to produce an amplitude of 4-5 % of the P wave on a stack of short-period data, the 400-km discontinuity must be both sufficiently sharp ( $\leq 10$  km) and define a reasonable velocity contrast ( $> 5\%$  if no focussing effects are included).

### 5.2.6 Discussion

The most important result of this study is the evidence for a locally sharp 670-km discontinuity from identifications of P670s phases on seismograms. A sharp 670-km discontinuity has previously been suggested from observations of precursors to P'P' phases and near source S-to-P converted phases, but these results were not without ambiguity (see section 5.1.2). In this respect, the waveform comparisons of P and P-to-S converted phases (Paulssen, 1985; this study) leave no doubt. The number of observations of upper mantle reflected and converted phases, and the estimated locations of reflection or conversion indicate that the discontinuity is a world wide feature present under continents and oceans, subduction zones and ridges. There is growing evidence that the transition is locally sharp

These seismological observations have important geodynamical implications. Lees et al. (1983) have shown that, for plausible mantle mineralogies, models that invoke phase transitions alone produce a reflectivity in the short-period frequency band that is an order of magnitude smaller than inferred from P'670P'. The reflectivity for short periods critically depends on the width of the phase transformation. Using the high pressure and temperature data compiled by Jeanloz & Thompson (1983), Lees et al. calculate that phase transitions occur over a 10 to 40 km depth interval, depending on the mineral assemblage. The values in this width range are too high to explain the seismic observations. Recent experimental work by Ito & Takahashi (1987) shows that the dissociation of  $\gamma$ -spinel into perovskite plus magnesiowüstite, probably the most important phase transition at a depth of 650 km, is completed within a pressure interval of 1 GPa ( $\approx$  25 km). Although this is sharp in a petrological sense (for a divariant phase transformation), it should be resolved with an accuracy of less than 0.2 GPa (5 km) to be able to compare the petrological results with the seismic observations. The dissociation of majorite, a garnet solid solution, evidently cannot explain the seismic 670-km discontinuity, because it occurs over a relatively wide pressure interval of about 4 GPa (Ito & Takahashi, 1987). A chemical transition, or a combination of a chemical and phase transition, can easily explain the sharpness of the 670-km discontinuity (see also Lees et al., 1983). A compositional change across the discontinuity would most naturally imply a chemically distinct upper and lower mantle, possibly involving 2-layered convection (Richter & Johnson, 1974; Christensen & Yuen, 1984). An alternative model is proposed by Ringwood & Irifune (1988). In this model, the upper and lower mantle are assumed to be of similar bulk composition separated by a chemical boundary layer at a depth of 600 to 700 km, which is supposed to have formed by effects of phase changes and differentiation in subducted slabs. The phase transformation of  $\gamma$ -spinel to perovskite plus magnesiowüstite together with the chemical change of (lenses of) former basaltic crust on top of ancient oceanic lithosphere could account for the sharp 670-km discontinuity and the variability of the (seismic) observations.

At present it is not clear whether the upper and lower mantle are chemically distinct or not. More seismological studies are required to improve our knowledge of seismological aspects of the 670-km discontinuity to be able to answer some basic questions: Is the 670-

km discontinuity only locally sharp, or is its sharpness a worldwide feature? Is topography of the 670-km discontinuity, as suggested by Richards & Wicks (1987), only locally significant or also on a global scale? What is the origin of the multiple SV-arrivals in the 66-72 s interval (this study)? What is the 'exact' velocity and density contrast across the 670-km discontinuity?

Short-period and broad-band body wave studies of converted and reflected phases now provide the most detailed information about the sharpness and depth of the 670-km discontinuity, but they could be complemented with those of long-period (or low-passed broad-band) data to investigate the frequency dependence of the variations among the observations. On the other hand, upper mantle refracted phases are more adequate to determine the velocity contrast across the transition. Although we are still far from 'global mapping' of the upper mantle discontinuities, an increased station density combined with a sufficient quantity of broad-band digital data would contribute to solve many of the ambiguities that still exist in detailed upper mantle studies.

Apart from seismological information, major advances in our understanding of the 670-km discontinuity are expected from other fields, especially from experimental petrological studies under high pressure and temperature conditions (see chapter 6).

## References

- Adams, R. D., Reflections from discontinuities beneath Antarctica, *Bull. Seismol. Soc. Am.*, *61*, 1441-1451, 1971.
- Barley, B.J., J.A. Hudson, and A. Douglas, S to P scattering at the 650-km discontinuity, *Geophys. J. R. astr. Soc.*, *69*, 159-172, 1982.
- Baumgardt, D. R., and S.S. Alexander, Structure of the mantle beneath Montana LISA from analysis of long-period, mode-converted phases, *Bull. Seismol. Soc. Am.*, *74*, 1683-1702, 1984.
- Bock, G., and J. Ha, Short-period S-P conversion in the mantle at a depth near 700 km, *Geophys. J. R. astr. Soc.*, *77*, 593-615, 1984.
- Bolt, B. A., and A. Qamar, Observations of pseudo-aftershocks from underground nuclear explosions, *Phys. Earth Planet. Inter.*, *5*, 400-402, 1972.
- Bouchon, M., and K. Aki, Near-field of a seismic source in a layered medium with irregular interfaces, *Geophys. J. R. astr. Soc.*, *50*, 669-684, 1977.
- Christensen, U.R., and D. Yuen, The interaction of a subducting lithospheric slab with a chemical or phase boundary, *J. Geophys. Res.*, *89*, 4389-4402, 1984.
- Cleary, J., Seismic wave scattering on underside reflection at the core-mantle boundary, *Phys. Earth Planet. Inter.*, *26*, 266-267, 1981.
- Dziewonski, A.M., and D.L. Anderson, Preliminary reference Earth model, *Phys. Earth Planet. Inter.*, *25*, 297-356, 1981.
- Engdahl, E.R., and E.A. Flinn, Seismic waves reflected from discontinuities within the Earth's upper mantle, *Science*, *163*, 177-179, 1969.
- Faber, S., and G. Müller, Sp phases from the transition zone between upper and lower mantle, *Bull. Seismol. Soc. Am.*, *70*, 487-508, 1980.
- Faber, S., and G. Müller, Converted phases from the mantle transition zone observed at European stations, *J. Geophys.*, *54*, 183-194, 1984.



- Fukao, Y., Upper mantle P-structure and the 650-km discontinuity, in *High Pressure Research*, edited by M.H. Manghnani and S. Akimoto, pp. 151-161, 1977.
- Gilbert, F., and A.M. Dziewonski, An application of normal mode theory to the retrieval of structural parameters and source mechanisms from seismic spectra, *Philos. Trans. R. Soc. London, Ser. A*, 278, 187-269, 1975.
- Husebye, E.S., R.A. Haddon, and D.W. King, Precursors to P'P' and upper mantle discontinuities, *J. Geophys.*, 43, 535-543, 1977.
- Ingate, S.F., J. Ha, and K.J. Muirhead, Limitations of waveform modelling of long-period seismograms, *Geophys. J. R. astr. Soc.*, 86, 57-61, 1986.
- Ito, E., and H. Takahashi, Ultrahigh-pressure phase transformations and the constitution of the deep mantle, in *High-pressure research in mineral physics*, edited by M.H. Manghnani and Y. Syono, pp. 221-229, Terra Scientific Publishing Company, Tokyo / American Geophysical Union, Washington, D.C., 1987.
- Jeanloz, R., and A.B. Thompson, Phase transitions and mantle discontinuities, *Rev. Geophys. Space Phys.*, 21, 51-74, 1983.
- Kind, R., and L.P. Vinnik, The upper-mantle discontinuities underneath the GRF array from P-to-S converted phases, *J. Geophys.*, in press, 1988.
- Kosarev, G.L., L.I. Makeyeva, and L.P. Vinnik, Anisotropy of the mantle inferred from observations of P to S converted waves, *Geophys. J. R. astr. Soc.*, 76, 209-220, 1977.
- Langston, C.A., Structure under Mount Rainier, Washington, inferred from teleseismic body waves, *J. Geophys. Res.*, 84, 4749-4762, 1979.
- Lees, A.C., Bukowinski M.S.T., and R. Jeanloz, Reflection properties of phase transitions and compositional change models of the 670-km discontinuity, *J. Geophys. Res.*, 88, 8145-8159, 1983.
- Muirhead, K., Comments on "Reflection properties of phase transition and compositional change models of the 670-km discontinuity" by Alison C. Lees, M.S.T. Bukowinski and Raymond Jeanloz, *J. Geophys. Res.*, 90, 2057-2059, 1985.
- Nakanishi, I., Seismic reflections from the upper mantle discontinuities beneath the Mid-Atlantic ridge observed by a seismic array in Hokkaido region, Japan, *Geophys. Res. Lett.*, 13, 1458-1461, 1986.
- Nakanishi, I., Reflections of P'P' from upper mantle mantle discontinuities beneath the Mid-Atlantic ridge, *Geophys. J.*, in press, 1988.
- Nolet, G., and Wortel M.J.R., Structure of the upper mantle, acc. for publ. in *Encyclopedia of Geophysics*, edited by D. James, Van Nostrand Reinhold, 1988.
- Owens, T.J., G. Zandt, and S.R. Taylor, Seismic evidence for an ancient rift beneath the Cumberland Plateau, Tennessee: a detailed analysis of broadband teleseismic P waveforms, *J. Geophys. Res.*, 89, 7783-7795, 1984.
- Owens, T.J., S.R. Taylor, and G. Zandt, Crustal structure at Regional Seismic Test Network stations determined from inversion of broadband teleseismic P waveforms, *Bull. Seismol. Soc. Am.*, 77, 631-662, 1987.
- Paulssen, H., Upper mantle converted waves beneath the NARS array, *Geophys. Res. Lett.*, 12, 709-712, 1985.
- Phinney, R.A., Structure of the Earth's crust from spectral behavior of long-period body waves, *J. Geophys. Res.*, 69, 2997-3017, 1964.
- Revenaugh, J., and T.H. Jordan, Observations of first-order mantle reverberations, *Bull. Seism. Soc. Am.*, 77, 1704-1717, 1987.
- Richards, M.A., and C.H. Wicks, Topography of the '650 km' discontinuity beneath Tonga from S-P conversion (abstract), *Eos Trans. AGU*, 68, 1379, 1987.
- Richards, P.G., Seismic waves reflected from velocity gradient anomalies within the Earth's upper mantle, *Z. Geophys.*, 38, 517-527, 1972.

- Richter, F.M., and C.E. Johnson, Stability of a chemically layered mantle, *J. Geophys. Res.*, *79*, 1635-1639, 1974.
- Ringwood, A.E., and T. Irifune, The nature of the 650-km discontinuity: implications for mantle dynamics, *Nature*, *331*, 131-136, 1988.
- Souriau, A., First analyses of broadband records on the GEOSCOPE network: potential for detailed studies of mantle discontinuities, *Geophys. Res. Lett.*, *13*, 1011-1014, 1986.
- Spakman, W., M.J.R. Wortel, and N.J. Vlaar, The Hellenic subduction zone: a tomographic image and its geodynamic implications, *Geophys. Res. Lett.*, *15*, 60-63, 1988.
- Teng, T.-L., and Tung J.P., Upper-mantle discontinuity from amplitude data of P'P' and its precursors, *Bull. Seismol. Soc. Am.*, *63*, 587-597, 1973.
- Vinnik, L.P., Detection of waves converted from P to SV in the mantle, *Phys. Earth Planet. Inter.*, *15*, 39-45, 1977.
- Walck, M.C., The P-wave upper mantle structure beneath an active spreading centre: the Gulf of California, *Geophys. J. R. astr. Soc.*, *76*, 697-723, 1984.
- Whitcomb, J.H., and D.L. Anderson, Reflections of P'P' seismic waves from discontinuities in the mantle, *J. Geophys. Res.*, *75*, 5713-5728 1970.

## *Chapter 6*

# **The upper mantle**

Not only seismology has contributed to present insights into the constitution of the Earth's upper mantle. Other geophysical data, as well as geochemical and geological observations, have provided valuable information about the structure of the upper mantle. The observations are widely varying in character, yielding information about different aspects of the upper mantle. In this chapter, a summary is given of some of this evidence and several of the models that have been proposed for the upper mantle. It is not meant to present a 'complete' picture of our knowledge of the upper mantle, but it intends to give some insight into phenomena that are well established and controversies that to this date still exist.

### **6.1 PETROLOGY OF THE UPPER MANTLE**

Petrological models can be seen as essential concepts of the mantle because they have implicit bearings on thermal and geodynamical aspects of the mantle and on aspects of the Earth's early evolution. Thus, a uniform mantle composition would suggest no chemical differentiation after, or concurrent with, the Earth's accretion, and would permit a regime of mass transport that encompasses the entire mantle. Petrological data from laboratory experiments have been used to investigate the viability of compositional models of the mantle and several aspects of this discussion will be presented in section 6.1.3. But first, in sections 6.1.1 and 6.1.2, a brief overview of the presently available petrological information of the upper mantle is given.

#### **6.1.1 Important phase transformations**

It is generally accepted that the most important upper mantle constituents are olivine

$(\text{Mg,Fe})_2\text{SiO}_4$ ), pyroxene  $(\text{Mg,Fe})\text{SiO}_3$ , and garnet  $(\text{Mg,Fe,Ca})_3\text{Al}_2\text{Si}_3\text{O}_{12}$ ). Major phase transformations in these components occur in the 10-30 GPa pressure interval, and this interval corresponds well with the 300-800 km depth range over which the seismic discontinuities and gradients are observed. Since phase changes in these systems could possibly account for *all* density and velocity transitions in the mantle, they have extensively been investigated, particularly in the last 10 to 15 years. Thus, it is known that  $(\text{Mg}_{0.9}\text{Fe}_{0.1})_2\text{SiO}_4$ -olivine converts to the  $\beta$ -spinel structure at a pressure of about 13 GPa (400 km), which subsequently transforms to the  $\gamma$ -spinel phase (at about 15 GPa, 440 km), and to an assemblage of  $(\text{Mg,Fe})\text{SiO}_3$ -perovskite and  $(\text{Mg,Fe})\text{O}$ -magnesiowüstite (at about 23 GPa, or 650 km).  $(\text{Mg}_{0.9}\text{Fe}_{0.1})\text{SiO}_3$ -enstatite transforms to an assemblage of  $\beta$ - $(\text{Mg,Fe})_2\text{SiO}_4$  plus stishovite, to  $\gamma$ - $(\text{Mg,Fe})_2\text{SiO}_4$  plus stishovite, to  $(\text{Mg,Fe})\text{SiO}_3$ -ilmenite, and to  $(\text{Mg,Fe})\text{SiO}_3$ -perovskite with increasing pressure. Most of the phase transformations in the pyroxene system occur at approximately the same pressures as in the olivine system, except that little is known of the stability field of ilmenite (for a review see Jeanloz & Thompson, 1983). In the presence of garnet, pyroxene will gradually dissolve in the garnet structure with increasing pressure, giving rise to a garnet-majorite solid solution. Irifune (1987) recently reexamined this pyroxene-garnet transition, because there was no general agreement on the details of this transformation. He showed that pyroxene gradually dissolves in the garnet structure up to pressures of 13-14 GPa, forming a single phase garnetite at 16 GPa (570 km). Ito & Takahashi (1987) showed that majorite-garnet further dissociates into Ca- and Mg-rich perovskites (and possibly garnet) over a broad (2-4 GPa) pressure interval starting at temperature and pressure conditions corresponding to a depth of about 600 km. Such a broad phase loop is in contrast to the transformation of  $\gamma$ - $(\text{Mg,Fe})_2\text{SiO}_4$  to perovskite which is completed over a pressure interval of less than 1 GPa (Ito & Takahashi, 1987).

### 6.1.2 Are the upper and lower mantle chemically distinct?

Although compositional changes across the 670-km discontinuity had been proposed earlier, Liu (1979a,b) was the first to suggest this on the basis of results from high pressure and temperature laboratory experiments. He argued that the change in density and bulk sound velocity  $(v_p^2 - 4/3v_s^2)^{1/2}$  across this transition must be the consequence of a change in composition from an olivine-rich upper mantle to a predominantly perovskitic lower mantle. However, uncertainties in the thermal expansion coefficient ( $\alpha$ ) and bulk modulus (K) of the perovskite phase affect the reliability of his interpretation (see e.g. Jackson, 1983). Knittle et al. (1986) and Knittle & Jeanloz (1987) recognized the importance of well constrained physical properties of the perovskite phase for the petrological interpretation of the lower mantle, and carried out diamond-anvil laboratory experiments to determine  $\alpha$ , K, and  $K'$  (the pressure derivative of K) of  $(\text{Mg}_{0.9}\text{Fe}_{0.1})\text{SiO}_3$ -perovskite. They showed that the zero-pressure density of the lower mantle is adequately explained by a pure

perovskitic composition, whereas a pyrolytic material in a lower mantle mineralogy yields a (zero-pressure) density that is 2% smaller than that of the lower mantle. These results would be in support of chemical stratification of the mantle, for instance by iron or silica enrichment in the lower mantle. Although these data provide at present the most compelling petrological arguments in support of a chemically distinct upper and lower mantle, there may be uncertainties, especially in the extrapolation of the data to zero pressure.

Lees et al. (1983) have addressed the subject from a different point of view. These authors compared the reflection properties obtained from the  $P'670P'/P'P'$  amplitude ratio with those calculated for phase transition and compositional change models. Phase transitions in the olivine, pyroxene, and garnet systems are predicted to occur over a depth interval of 10 to 40 km (on the basis of the available data at that time). A transition over such an interval is too wide to explain the high amplitudes of the the observed  $P'670P'$  phases, or the observations of P-to-S converted phases presented in chapter 5. Lees et al. further showed that acceptable quantities of iron or silica enrichment across the 670-km phase transformation (or in the high-pressure phase regime) would produce a 'discontinuous' transition of which the calculated reflection coefficient is consistent with the seismic data. However, it should be noted that the amplitude of a seismic phase may be affected significantly by focussing effects along an individual raypath, and this may invalidate a simple petrological interpretation of the seismological amplitude information.

In this regard, it is important to note that unambiguous evidence for a locally sharp 670-km discontinuity is presented in chapter 5. It is clear that the observations of P-to-S converted phases are readily reconciled with a change in chemical composition. The important question still to be answered is whether a phase transition can occur over a depth interval of a few kilometers only. Recent results of Ito & Takahashi (1987) showed that the  $\gamma$ -spinel to perovskite plus magnesiowüstite phase transformation at high temperatures (1600°C) occurs over a small pressure interval, and this could alter the conclusions of Lees et al. (1983). They constrained the width of this phase loop to a pressure interval of less than 1 GPa. This is still 5 times larger than the thickness implied by the seismic data. At present, it seems unlikely that the transformation occurs over an interval of less than 0.2 GPa (~ 5 km) (see also Jeanloz & Thompson, 1983). The majorite-perovskite phase transition must be excluded as a possible explanation of the sharp seismic 670-km discontinuity because it occurs over a wide pressure interval of about 2 to 4 GPa (Ito & Takahashi, 1987).

The only way to reconcile a sharp 670-km discontinuity with a broader divariant phase transformation may be to invoke nonequilibrium effects caused by large vertical motion, as suggested by Loper (1985). Material moving fast through a phase boundary may then not immediately form new crystals at equilibrium conditions. 'Overstepping' will occur when the pressure and temperature conditions are such that the threshold energy for the phase reaction in the dynamic situation is reached (Schuiling, pers comm., 1988). However, the importance of this effect for the  $\gamma$ -spinel to perovskite plus magnesiowüstite phase

transition at mantle conditions is not yet known. We conclude that, the most straightforward interpretation of the seismic 670-km discontinuity presently is a transition of a (at least partially) compositional nature.

### 6.1.3 Compositional models of the upper mantle

#### PYROLITE MODEL

Ringwood (1975) presented a review of the experimental petrological data at that time available, and related these to upper mantle petrological, mineralogical, geochemical data, and cosmochemical and seismic evidence. Ringwood suggested that the main constituent of both upper and lower mantle is a theoretical mineral assemblage called 'pyrolite'. It has the composition of what is thought to be an undifferentiated primitive mantle, consisting of about 57% olivine, 17% orthopyroxene, 12% clinopyroxene, and 14% garnet. In this model new oceanic lithosphere is formed by the uprise of pyrolite from the low velocity layer. It yields a basaltic crust upon partial melting, and leaves a mineralogically differentiated and chemically stratified peridotitic lithosphere. The 400- and 650-km discontinuity are attributed to phase transformations in the MgO–FeO–SiO<sub>2</sub> system: the 400-km discontinuity is explained by the divariant phase transformation of olivine to  $\beta$ -spinel, and the 670-km discontinuity (originally) by the 'spinel-postspinel' phase change, where the postspinel phase was later experimentally determined as an assemblage of perovskite and magnesiowüstite.

The essence of this pyrolite model has not changed, but significantly more detail has been suggested concerning the fate of the subducting slab and its role in mantle convection. On the basis of the petrology of subducted lithosphere and evidence of phase transformations and associated density variations, Ringwood (1982) and Ringwood & Irifune (1988) suggest that the harzburgitic and basaltic components of young slabs may become trapped on top of the 670-km discontinuity, whereas relatively old slabs penetrate into the lower mantle. The 670-km discontinuity is, in this view, a combination of a phase transformation with the chemical transition of lenses of buoyantly trapped basaltic crust on top of a lower mantle of perovskite and magnesiowüstite.

#### PICLOGITE MODEL

Anderson (1979a, 1984) proposes a chemically stratified upper mantle in which eclogite is an important assemblage. He assumes that during the accretional differentiation of the Earth heavy eclogite accumulated at the base of the upper mantle, while low-density olivine concentrated in the shallow mantle in the form of peridotite. The region of accumulated eclogite was originally thought to start at a depth of about 220 km, the Lehmann discontinuity (Anderson, 1979a,b), but later (Anderson & Bass, 1984, 1986) it

was suggested that this region would coincide with the transition region (between the 400- and 670-km discontinuity). Anderson presents several arguments in favour of his model. He argues that at an early stage of the history of the Earth melt separation must have occurred at initially low pressures. From the melt layer garnet crystallized to a clinopyroxene-garnet-rich mixture with some olivine, called piclogite (a mixture of eclogite and olivine). This assemblage accumulated at the base of the upper mantle, where it is gravitationally stable, and thereby created the transition region. The high seismic velocity gradient in the transition region is readily explained by the gradual transformation of clinopyroxene to garnet-majorite. The 400- and 670-km discontinuity are in this model of chemical nature, the 400-km discontinuity being the transition from olivine and orthopyroxene to piclogite, and the 670-km discontinuity the transition from piclogite to  $(\text{Mg,Fe})\text{SiO}_3$ -perovskite.

#### ACCEPTABILITY OF COMPOSITIONAL MANTLE MODELS

Attempts have been made to 'prove' the (im)possibility to reconcile these compositional models with phenomena of the upper mantle seismic structure. Aspects that are of concern in this respect are (1) the general velocity structure in the upper 400 km, in the transition zone, and in the lower mantle, (2) the magnitude of the velocity (and density) increase at the 400- and 670-km discontinuity, and (3) the width of these discontinuities.

Although Ringwoods pyrolite model has achieved wide acceptance, there are also controversies. Bass & Anderson (1984) and Anderson & Bass (1984, 1986) argued that neither the (small) width of the discontinuities, nor the velocity structure within the transition zone could be satisfied with the phase transformations in the pyrolitic composition. Except for the sharpness of the 670-km discontinuity (originally proposed to be the spinel-postspinel phase transformation), these arguments have been attacked by Weidner (1985, 1986) and Bina & Wood (1987). In the more recent model (Ringwood & Irifune, 1988), the 670-km discontinuity is envisaged as the result of complex interaction of subducted lithosphere with the surrounding mantle. The chemical transition of lenses of buoyantly trapped basaltic crust on top of the lower mantle could account for the local sharpness of the 670-km discontinuity and for the variability of the reflected and converted phases as discussed in chapter 5.

The 'piclogite' model proposed by Bass & Anderson (1984) and Anderson & Bass (1986) has generally been regarded as the counterpart of the essentially uniform pyrolite model. The chemical transitions at depths of about 400 and 670 km easily explain the sharpness of the discontinuities, although it may be more difficult to explain why converted and reflected phases from the 400-km discontinuity are less frequently observed than from the 670-km discontinuity (chapter 5). The strong seismic velocity gradient in the transition zone is in this model accounted for by the eclogite-majorite transformation.

Although the laboratory measurements of Knittle et al. (1986) and Knittle & Jeanloz (1987) suggest that  $\text{Mg}_{0.9}\text{Fe}_{0.1}\text{SiO}_3$ -perovskite is more likely as a lower mantle composition

(in agreement with the piclogite model) than pyrolite, it is presently not possible to exclude either *upper* mantle model on petrological grounds. A further discussion of the many petrological arguments in favour (or against) these compositional models will therefore not be given here.

In conclusion, it should be noted that these upper mantle models should be regarded as possible 'simple' representations of reality: the models are essentially laterally homogeneous beneath the low velocity zone (except for regions of subduction or uprising), but seismological data, for instance of the European subcontinental mantle, indicate that significant small scale lateral heterogeneity is present to a depth of at least 400 km (see chapter 4; Spakman et al., 1988).

## 6.2 GEODYNAMICS OF THE UPPER MANTLE

### 6.2.1 Whole-mantle or layered convection?

The depth and regime of mantle convection has been a subject of controversy since it is accepted that there is mass transport in the mantle. The discussion on this field has primarily concentrated on the viability of two extreme models: 'whole-mantle' or (two-) 'layered' convection. In the layered convection model mass transport is confined to two separate systems corresponding to the upper and lower mantle, whereas in the whole-mantle convection model the system of flow affects the entire mantle. An outline of aspects that have contributed to the discussion of whole-mantle or layered convection is presented in the following. The observation of a sharp 670-km discontinuity is in this view of large relevance, because it indicates that a well-mixed 'whole mantle' is unlikely.

#### INITIAL ARGUMENTS: VISCOSITY OR DENSITY CONTRAST BETWEEN UPPER AND LOWER MANTLE?

Early arguments in favour of 'layered' (or actually upper mantle) convection were based on the assumption of a strong viscosity increase across the transition zone. In initial models (e.g. McKenzie, 1967; McConnell, 1968), all mass transport was therefore restricted to the upper mantle, while the lower mantle was thought to behave rigidly. However, from analysis of postglacial rebound data, it was recognized that there is most likely only a modest viscosity increase (at most one order of magnitude) between upper and lower mantle (e.g. Cathles, 1975; Peltier, 1976), and this observation has subsequently been taken as strong evidence in support of whole-mantle convection (e.g. Davies, 1977; Peltier & Jarvis, 1982).

The notion that the *nature* of the upper mantle discontinuities may be of relevance to possible regimes of mass transport has led several authors to investigate the influence of mineralogical phase transformations and compositional density variations on mantle



convection. Schubert & Turcotte (1971) and Richter (1973) showed that an exothermic phase transition with properties characteristic of the olivine-spinel phase transition (associated with the 400-km discontinuity) would not affect the structure of flow, but would only increase the flow velocity. An endothermic phase reaction with a Clapeyron slope of about -2 MPa/K, as proposed for the spinel-postspinel (670-km) transition (Ito & Yamada, 1982), would only have a mildly stabilizing effect (Schubert et al., 1975) and would most likely not inhibit whole-mantle convection. This result was later (numerically) confirmed by Christensen & Yuen (1985) who estimated that the critical Clapeyron slope to force two-layered convection would be in the range of -4 to -8 MPa/K (depending mainly on the Rayleigh number of flow). In contrast to the findings for phase transformations, Richter & Johnson (1974) showed that if the upper and lower mantle are chemically distinct, layered convection would be most probable.

Another (early) argument for layered convection was therefore based on the inference of compositional stratification of the mantle. It was observed that the (seismologically determined) density increase across the transition zone was larger than expected from phase changes alone (e.g. Anderson, 1968; Press, 1968). However, the empirical relationship between density and mean atomic weight on which this argument was based, has been found unreliable for high pressure and temperature mineral phases (Ringwood, 1975). Thus, the question of whether the 670-km discontinuity constitutes a chemical transition remained unanswered.

#### SLAB PENETRATION INTO THE LOWER MANTLE OR NOT?

In this respect, evidence from deep focus earthquakes should also be mentioned. Studies of seismicity showed that no earthquakes occur below a depth of about 700 km, after an increase in seismic energy release between 500 and 700 km (e.g. Isacks & Molnar, 1971; Vassiliou et al., 1984; Giardini & Woodhouse, 1984). In addition, it was found that most deep earthquakes exhibit downdip compressional focal mechanisms (Isacks & Molnar, 1971; Giardini & Woodhouse, 1984). These observations have been taken as arguments that the lower mantle would act as a barrier to the subducted lithosphere either by a strong viscosity increase or a density gradient, which would prevent the slab to penetrate into the lower mantle (e.g. Richter, 1979; Vassiliou et al., 1984). The inability of slab penetration into the lower mantle would imply two separate mass transport systems in upper and lower mantle.

However, Wortel (1986) showed that the increase in compressional seismic energy release between 500 and 700 km and the cessation of seismicity at about 700 km depth can also be explained by the thermal assimilation of the subducted plate. He demonstrated that no barrier is required to explain the seismicity observations, and this would imply that these data may not be invoked as evidence in support of layered convection.

In fact, there are indications that some subducted slabs do penetrate into the lower mantle. Residual sphere analyses (i.e. studies of travel time anomalies that are corrected

for all known delays apart from those near the source) of deep earthquakes (Jordan, 1977; Creager & Jordan, 1984, 1986; Fischer et al., 1987) and observations of multipathing (Silver & Chan, 1986; Beck & Lay, 1986) seem to require aseismic, lower mantle extensions of the slabs along the northwestern Pacific of several hundred kilometers. Tomographic studies by Grand (1987) and VanderHilst (pers. comm., 1987) show a lower mantle S- and P-wave velocity anomaly extending from the eastern Caribbean to the northern U.S. This anomaly may be associated with past subduction of the Farallon plate beneath North America. Although the interpretations of all these studies may be questioned, it should be noted that the data are suggestive of mass transport between upper and lower mantle in some regions of subduction.

Thus, if we assume that slab penetration into the lower mantle occurs, does this then necessarily imply that the upper and lower mantle are uniform in composition, and is mass circulation then 'inevitably' that of whole-mantle convection? Christensen & Yuen (1984) have investigated this aspect by numerical modelling of convection. They showed that, in absence of a phase transition, a compositional density contrast of over 5% between upper and lower mantle will prevent slabs to descend into the lower mantle. However, if this density difference is smaller than 5%, then subducted lithosphere will be able to plunge into the lower mantle for several hundred km, and some limited degree of mixing between upper and lower mantle will be possible. For an even smaller chemical density contrast, less than 2%, the slab will sink to the core-mantle boundary, and the resulting convective regime will be essentially that of whole-mantle convection.

#### DENSITY CONTRAST BETWEEN UPPER AND LOWER MANTLE

The density contrast between upper and lower mantle as given by reference Earth models is 6% (1066B) to 9% (PREM). As is generally accepted, at least a part of the total density increase is due to phase changes. The question is, whether a part of density contrast must be contributed to a chemical transition or not.

Recent experimental work on the thermal expansion coefficient of  $\text{Mg}_{0.9}\text{Fe}_{0.1}\text{SiO}_4$ -perovskite by Knittle et al. (1986) allowed an estimate of the zero-pressure density of the perovskite phase. These authors conclude that the (extrapolated) zero-pressure density of a pyrolyte at lower mantle conditions is 2% smaller than that estimated for the (seismological) lower mantle by adiabatic decompression. Although this does suggest that the upper and lower mantle are chemically distinct (assuming a pyrolytic upper mantle), this inference may also be questioned, especially concerning to the extrapolation to zero-pressure. In this respect, it should be noted that the sharpness of the 670-km discontinuity, implied by the observations of P-to-S conversions, is also suggestive of a chemical transition between upper and lower mantle. This observations substantiate the (weak) petrological argument for a chemical density difference between upper and lower mantle.

The magnitude of a chemical contribution to the density contrast across the transition is not known. If we take, as an example, 2% for the chemical density difference at 670 km,

and if we assume that the transition to a predominantly perovskitic phase has a negative Clapeyron slope of  $-2$  MPa/K (Ito & Takahashi, 1987), then the modelling results of Christensen & Yuen (1984) indicate that slab penetration is possible and that some degree of mixing between upper and lower mantle may occur. The style of convection for this situation may certainly not be interpreted as whole-mantle convection, but may also not be referred to as strict layered convection because of the mass transport between upper and lower mantle. Although small variations in the (unknown) compositional density contrast or (badly constrained) Clapeyron slope may drastically alter the results, this example indicates that the convective regime of the mantle may be that of 'layered convection' with some mass transport between upper and lower mantle. Such a convective regime is presently a very acceptable model, because it incorporates phenomena such as a sharp 670-km discontinuity, a chemical density contrast, and slab penetration.

#### GEOCHEMICAL EVIDENCE

Geochemical contributions to the 'geodynamical discussion' cannot be excluded in this overview, because geochemical data have provided strong arguments in favour of a chemically stratified mantle and two-layered convection.

From analyses of isotope ratios, it was recognized that mid-ocean ridge basalts (MORBs) are strongly depleted in incompatible elements, whereas the continental crust appeared enriched in these elements. In geochemical models of the mantle this has been explained by the 'plate-tectonic process', which would serve as a mechanism that transports incompatible elements from the ridge to the trench, where they are then supplied to the continental crust by island-arc volcanism. In this model, the source of MORB and the enriched continental crust can be seen as complementary geochemical reservoirs. This observation of distinct geochemical reservoirs has led several investigators to estimate the size of the depleted reservoir by estimating the mass of the continental crust and assuming that the combination of the two must yield an undepleted, primitive mantle composition consistent with that of chondrites. Following this approach, Jacobsen & Wasserburg (1979), O'Nions et al. (1979), and Turcotte & Kellogg (1986) have reached similar conclusions, implying that the depleted reservoir more or less coincides with the upper mantle, and that the lower mantle is an undepleted reservoir. If the assumptions are correct, this geochemical evidence is a strong argument in support of a chemically stratified mantle and two-layered convection.

There are several uncertainties, however, which may drastically alter the conclusions. They concern the way in which early and later differentiation or fractionation has occurred in the mantle, the average bulk Earth isotope concentrations, the isotope concentrations and volume of the enriched reservoir. Davies (1981) and Allègre et al. (1983) showed that the volume of the enriched reservoir may be anywhere between 30 and 90% of the total volume of the mantle depending on the assumptions made. Moreover, apart from the 'conventional model' described above, widely varying convective models have been

proposed that may also explain the geochemical observations (e.g. Spohn & Schubert, 1982; Davies, 1981, 1984; Loper, 1985).

The observation of a sharp 670-km discontinuity is not consistent with a well-mixed uniform mantle. Models with geochemical heterogeneities in the form of distinct 'blobs' moving in a uniform mantle matrix (Davies, 1984) must therefore be excluded. In addition, Hoffmann & McKenzie (1985) showed by numerical modelling that only layered convection can explain the spatial distribution of geochemical heterogeneities.

Although it is evident that there are still many controversies regarding the interpretation of the geochemical data, Silver et al. (1988) reached a similar conclusion as stated in the previous section. They showed that geochemical observations are consistent with a model of predominantly layered convection which also includes mass transport between upper and lower mantle.

### 6.2.2 Geodynamical models of the upper mantle

In the previous section, we have concentrated on large scale features of the mantle. However, the observations of chapter 4 imply that there is significant small scale lateral heterogeneity in the subcontinental mantle beneath Europe. In this section geodynamical models of the upper mantle will be discussed that include features of upper mantle heterogeneity.

The key elements of Jordan's 'tectosphere model' (Jordan, 1975, 1978) are distinct continental roots. These roots consist of mineral assemblages that are less dense than those of the suboceanic upper mantle. They serve to stabilize the density variations that arise from differences between the oceanic and continental geotherms. These chemical variations are thought to be induced by basalt depletion, and this may have caused the so-called 'tectosphere' to extend from less than 100 km (for unstable continents) to 400 km depth (beneath stable shields). Seismological data are in support of such a model, as long-wavelength regional variations in the seismic velocity structure (extending to a depth of 300 to 400 km) show a correlation with surface tectonics. The seismic velocity distributions of chapter 4 show a high velocity lid that could be interpreted as the 'tectosphere' of Jordan's model. However, our data are also indicative of small scale heterogeneity in the upper mantle beneath Europe, and such elements are not incorporated in the tectosphere model.

Vlaar (1983) considers the subhorizontal subduction of a young, buoyant oceanic lithosphere underneath an old, strong oceanic or continental plate, a mechanism that can also be envisaged as the obduction of an old plate over the younger one. In this mechanism, ocean ridges are eventually also overridden, a process that presently is occurring at the northwestern margin of the U.S., for instance. Vlaar suggests that this process of 'lithospheric doubling' has been important throughout geological history. It would induce a strongly layered upper mantle with large (linear) thermal anomalies, and

could therefore account for upper mantle thermal anomalies, and for much of the observed heterogeneity in magmas. Such a scenario, which is proposed as a mechanism for the Alpine orogeny (Vlaar & Cloetingh, 1984), could provide an explanation for the small scale lateral heterogeneity inferred from the data presented in chapter 4. However, it is not clear to what lateral extent this process may have been important for the upper mantle beneath Europe. Although compatible with the heterogeneity predicted with Vlaar's model, the results of chapter 4 lack the horizontal resolution to firmly support or disprove the hypothesis of lithospheric doubling.

### **6.3 IN CONCLUSION**

Having reviewed the petrological evidence and current theories of mantle dynamics, we are able to put the conclusions of chapters 4 and 5 in a somewhat broader perspective.

Small-scale heterogeneity in the P- and S-wave velocity of the upper mantle beneath Europe has been inferred from the analysis of broad-band NARS data. These results indicate that the upper mantle is less homogeneous than was generally assumed, and make it evident that the classical petrological model for the upper mantle is unsatisfactory. Unfortunately, the seismograms from which these results are obtained are too sparse to map the three-dimensional P- and S-wave anomalies. A better resolution will be obtained from a larger data set that will become available if a much denser network of broad-band stations starts operating, as is expected in the next decade. We will then be able to image the detailed upper mantle P- and S-wave velocity structure with tomographic techniques using waveform information. The research on upper mantle lateral heterogeneity described in this thesis can thus be seen as a first step in this direction. Moreover, with the aid of a dense network of broad-band stations, we may even be able to map the topography of the 670-km discontinuity.

However, further progress in finding more definite answers on questions regarding the petrology and geodynamics of the upper mantle should also come from fields outside seismology. This is especially pertinent for laboratory investigations of phase transformations at conditions such as expected at about 670 km depth. The seismological evidence for sharpness of the 670-km discontinuity is now firm, but the absence of hard petrological constraints hamper the interpretation.

The results of this thesis have shown that a detailed analysis of high-quality seismological data may contribute new insights into structure of the upper mantle. Small scale lateral (seismic velocity) heterogeneity in the European subcontinental upper mantle and a (at least locally) sharp 670-km discontinuity are features that must be incorporated in petrological or geodynamical representations of the Earth's upper mantle.

## References

- Allegre, C.J., S.R. Hart, and J.F. Minster, Chemical structure and evolution of the mantle and continents determined by inversion of Nd and Sr isotopic data, II, Numerical results and discussion, *Earth Planet. Sci. Lett.*, *66*, 191-213, 1983.
- Anderson, D.L., Chemical inhomogeneity of the mantle, *Earth Planet. Sci. Lett.*, *5*, 89-94, 1968.
- Anderson, D.L., The upper mantle transition region: eclogite?, *Geophys. Res. Lett.*, *6*, 433-436, 1979a.
- Anderson, D.L., The deep structure of continents, *J. Geophys. Res.*, *84*, 7555-7560, 1979b.
- Anderson, D.L., The Earth as a planet, paradigms and paradoxes, *Science*, *223*, 347-355, 1984.
- Anderson, D.L., and J.D. Bass, Mineralogy and composition of the upper mantle, *Geophys. Res. Lett.*, *11*, 637-640, 1984.
- Anderson, D.L., and J.D. Bass, Transition region of the Earth's upper mantle, *Nature*, *320*, 321-328, 1986.
- Bass, J.D., and D.L. Anderson, Composition of the upper mantle: geophysical tests of two petrological models, *Geophys. Res. Lett.*, *11*, 237-240, 1984.
- Beck, S.L., and T. Lay, Test of the lower mantle slab penetration hypothesis using broadband S waves, *Geophys. Res. Lett.*, *13*, 1007-1010, 1986.
- Bina, C.R., and B.J. Wood, Olivine-spinel transitions: experimental and thermodynamic constraints and implications for the nature of the 400-km discontinuity, *J. Geophys. Res.*, *92*, 4853-4866, 1987.
- Cathles, L.M., *The viscosity of the Earth's mantle*, 386 pp., Princeton University Press, Princeton, New Jersey, 1975.
- Christensen, U.R., and D. Yuen, The interaction of a subducting lithospheric slab with a chemical or phase boundary, *J. Geophys. Res.*, *89*, 4389-4402, 1984.
- Christensen, U.R., and D. Yuen, Layered convection induced by phase transitions, *J. Geophys. Res.*, *90*, 10,291-10,300, 1985.
- Creager, K.C., and T.H. Jordan, Slab penetration into the lower mantle, *J. Geophys. Res.*, *89*, 3031-3050, 1984.
- Creager, K.C., and T.H. Jordan, Slab penetration into the lower mantle beneath the Mariana and other island arcs of the Northwest Pacific, *J. Geophys. Res.*, *91*, 3573-3589, 1986.
- Davies, G.F., Whole mantle convection and plate tectonics, *Geophys. J. R. astr. Soc.*, *49*, 459-486, 1977.
- Davies, G.F., Earth's neodymium budget and structure and evolution of the mantle, *Nature*, *290*, 208-213, 1981.
- Davies, G.F., Geophysical and isotopic constraints on mantle convection: an interim synthesis, *J. Geophys. Res.*, *89*, 6017-6040, 1984.
- Fischer, K. M., T.H. Jordan, and K.C. Creager, Seismic constraints on the morphology of deep slabs, *J. Geophys. Res.*, *in press*, 1987.
- Giardini, D., and J.H. Woodhouse, Deep seismicity and modes of deformation in Tonga subduction zone, *Nature*, *307*, 505-509, 1984.
- Grand, S.P., Tomographic inversion for the shear wave velocity beneath the North American plate, *J. Geophys. Res.*, *92*, 14,065-14,090, 1987.
- Hoffmann, N.R.A., D.P. McKenzie, The destruction of geochemical heterogeneities by differential fluid motions during mantle convection, *Geophys. J. R. astr. Soc.*, *82*, 163-206, 1985.
- Irfune, T., An experimental investigation of the pyroxene-garnet transformation in a pyrolite composition and its bearing on the constitution of the mantle, *Phys. Earth Planet. Inter.*, *45*, 324-336, 1987.

- Isacks, B., and P. Molnar, Distribution of stresses in the descending lithosphere from a global survey of focal-mechanism solutions of mantle earthquakes, *Rev. Geophys. Space Phys.*, *9*, 103-174, 1971.
- Ito, E., and H. Takahashi, Ultrahigh-pressure phase transformations and the constitution of the deep mantle, in *High-pressure research in mineral physics*, edited by M.H. Manghnani and Y. Syono, pp. 221-229, Terra Scientific Publishing Company, Tokyo / American Geophysical Union, Washington, D.C., 1987.
- Ito, E., and H. Yamada, Stability relations of silicate spinels, ilmenites, and perovskites, in *High Pressure Research in Geophysics*, edited by S. Akimoto and M.H. Manghnani, pp. 405-419, Center for Academic Publishing, Tokyo, 1982.
- Jackson, I., Some geophysical constraints on the chemical composition of the Earth's lower mantle, *Earth Planet. Sci. Lett.*, *62*, 91-103, 1983.
- Jacobsen, S.B., and G.J. Wasserburg, The mean age of the mantle and crustal reservoirs, *J. Geophys. Res.*, *84*, 7411-7427, 1979.
- Jeanloz, R., and A.B. Thompson, Phase transitions and mantle discontinuities, *Rev. Geophys. Space Phys.*, *21*, 51-74, 1983.
- Jordan, T.H., The continental tectosphere, *Rev. Geophys. Space Phys.*, *13*, 1-12, 1975.
- Jordan, T.H., Lithospheric slab penetration into the lower mantle beneath the Sea of Okhotsk, *J. Geophys.*, *43*, 473-496, 1977.
- Jordan, T.H., Composition and development of the continental tectosphere, *Nature*, *274*, 544-548, 1978.
- Knittle, E., and R. Jeanloz, Synthesis and equation of state of (Mg,Fe)SiO<sub>3</sub> perovskite to over 100 Gigapascals, *Science*, *235*, 668-670, 1987.
- Knittle, E., R. Jeanloz, and G.L. Smith, Thermal expansion of silicate perovskite and stratification of the Earth's mantle, *Nature*, *319*, 214-216, 1986.
- Lees, A.C., M.S.T. Bukowinski, and R. Jeanloz, Reflection properties of phase transition and compositional change models of the 670-km discontinuity, *J. Geophys. Res.*, *88*, 8145-8159, 1983.
- Liu, L.-G., Calculations of high-pressure phase transitions in the system MgO-SiO<sub>2</sub> and implications for mantle discontinuities, *Phys. Earth Planet. Inter.*, *19*, 319-330, 1979a.
- Liu, L.-G., On the 650 km seismic discontinuity, *Earth Planet. Sci. Lett.*, *42*, 202-208, 1979b.
- Loper, D.E., A simple model of whole-mantle convection, *J. Geophys. Res.*, *90*, 1809-1836, 1985.
- McConnell, R.K., Viscosity of the mantle from relaxation time spectra of isostatic adjustment, *J. Geophys. Res.*, *73*, 7089-7105, 1968.
- McKenzie, D.P., The viscosity of the mantle, *Geophys. J. R. astr. Soc.*, *14*, 297-305, 1967.
- O'Nions, R.K., N.M. Evensen, and P.J. Hamilton, Geochemical modelling of mantle differentiation and crustal growth, *J. Geophys. Res.*, *84*, 6091-6101, 1979.
- Peltier, W.R., Glacial isostatic adjustment. II. The inverse problem, *Geophys. J. R. astr. Soc.*, *46*, 669-706, 1976.
- Peltier, W.R., and G.T. Jarvis, Whole mantle convection and the thermal evolution of the Earth, *Phys. Earth Planet. Inter.*, *29*, 281-304, 1982.
- Press, F., Density distribution in the Earth, *Science*, *160*, 1218-1221, 1968.
- Richter, F.M., Finite amplitude convection through a phase boundary, *Geophys. J. R. astr. Soc.*, *35*, 265-276, 1973.
- Richter, F.M., Focal mechanisms and seismic energy release of deep and intermediate earthquakes in the Tonga-Kermadec region and their bearing on the depth extent of mantle flow, *J. Geophys. Res.*, *84*, 6783-6795, 1979.
- Richter, F.M., and C.E. Johnson, Stability of a chemically layered mantle, *J. Geophys. Res.*, *79*, 135-1639, 1974.
- Ringwood, A., *The composition of the Earth's mantle*, pp. 618, McGraw-Hill, New York, 1975.

- Ringwood, A.E., Phase transformations and differentiation in subducted lithosphere: implications for mantle dynamics, basalt petrogenesis, and crustal evolution, *J. Geology*, *90*, 611-643, 1982.
- Ringwood, A.E., and T. Irifune, Nature of the 650 km discontinuity: implications for mantle dynamics, *Nature*, *331*, 131-136, 1988.
- Schubert, G., and D.L. Turcotte, Phase changes and mantle convection, *J. Geophys. Res.*, *76*, 1424-1432, 1971.
- Schubert, G., D.A. Yuen, and D.L. Turcotte, Role of phase transitions in a dynamic mantle, *Geophys. J. R. astr. Soc.*, *42*, 705-735, 1975.
- Silver, P.G., and W.W. Chan, Observations of body wave multipathing from broadband seismograms: Evidence for lower mantle slab penetration beneath the Sea of Okhotsk, *J. Geophys. Res.*, *91*, 13,787-13,802, 1986.
- Silver, P.G., R.W. Carlson, and P. Olson, Deep slabs, geochemical heterogeneity and the large-scale structure of mantle convection: investigation of an enduring paradox, *Ann. Rev. Earth Planet. Sci.*, submitted, 1987.
- Spakman, W., M.J.R. Wortel, and N.J. Vlaar, The hellenic subduction zone: a tomographic image and its geodynamic implications, *Geophys. Res. Lett.*, *15*, 60-63, 1988.
- Spohn, T., and G. Schubert, Modes of mantle convection and the removal of heat from the Earth's interior, *J. Geophys. Res.*, *87*, 4682-4696, 1982.
- Turcotte, D.L., and L.H. Kellogg, Isotopic modeling of the evolution of the mantle and crust, *Rev. Geophys.*, *24*, 311-328, 1986.
- Vassiliou, M.S., B.H. Hager, and A. Raefsky, The distribution of earthquakes with depth and stress in subducting slabs, *J. Geodynamics*, *1*, 11-28, 1984.
- Vlaar, N.J., Thermal anomalies and magmatism due to lithospheric doubling, *Earth Planet. Sci. Lett.*, *65*, 322-330, 1983.
- Vlaar, N.J., and S.A.P.L. Cloetingh, Orogeny and ophiolites: plate tectonics revisited with reference to the Alps, *Geol. Mijnbouw*, *63*, 159-164, 1984.
- Weidner, D.J., A Mineral physics test of a pyrolite mantle, *Geophys. Res. Lett.*, *12*, 417-420, 1985.
- Weidner, D.J., Mantle model based on the measured physical properties of minerals, in *Advances in Physical Geochemistry, Vol 6, Chemistry and Physics of Terrestrial Planets*, edited by S.K. Saxena, pp. 251-274, Springer Verlag, New York, 1986.
- Wortel, R., Deep earthquakes and the thermal assimilation of subducting lithosphere, *Geophys. Res. Lett.*, *13*, 34-37, 1986.



## *Samenvatting*

Seismologisch onderzoek heeft een belangrijke bijdrage geleverd tot onze huidige kennis van de structuur van de aarde. De globale verdeling van de seismische snelheden was reeds bekend in de 30-er jaren, en op basis hiervan werd een onderverdeling gemaakt in verschillende regio's (korst, bovenmantel, transitie-zone, ondermantel, binnen- en buitenkern). De interpretatie van de seismologische gegevens naar de compositionele, thermische, en geodynamische opbouw van de aarde is sindsdien een belangrijk onderwerp in de geofysica van de vaste aarde. Momenteel staan er nog belangrijke vragen open op dit gebied, waarvoor seismologische gegevens met een hoge resolutie van belang kunnen zijn. Het onderzoek van dit proefschrift moet in deze context gezien worden, omdat het twee aspecten behandelt van de gedetailleerde structuur van de bovenmantel.

De seismische opbouw van de bovenmantel onder Europa is onderzocht m.b.v. ruimtegolven van bevingen uit het oostelijke Middellandse zeegebied die zijn geregistreerd in stations van het NARS array in west Europa. Uit analyse van deze gegevens blijkt dat de globale seismische structuur van de bovenmantel onder Europa beschreven kan worden door een hoge snelheidslaag tot op een diepte van ongeveer 120 km, een lage snelheidslaag, en twee discontinuïteiten op dieptes van circa 420 en 650 km. De seismische data wijzen echter ook op belangrijke laterale variaties in de snelheidsstructuur tot op een diepte van ongeveer 400 km op relatief kleine schaal. Deze resultaten impliceren dat de Europese subcontinentale bovenmantel heterogener is dan vaak werd verondersteld.

Een ander onderzoek is verricht naar de gedetailleerde structuur van de bovenmanteldiscontinuïteiten. M.b.v. golven die van P naar S zijn geconverteerd in de bovenmantel onder de seismische stations, kon worden afgeleid dat de zg. 670-km discontinuïteit lokaal bijzonder 'scherp' moet zijn. Deze observatie kan erop duiden dat de boven- en ondermantel chemisch van verschillende samenstelling zijn.

## *Acknowledgements*

Bij het voltooien van dit proefschrift wil ik een aantal personen bedanken die hebben bijgedragen tot het onderzoek of die tot steun zijn geweest.

In de eerste plaats dank ik mijn promotor, Prof. Guust Nolet. Hij is de initiator van het NARS-project, en door zijn actieve inzet heeft seismologie uit Utrecht internationale bekendheid opgebouwd. De vrijheid tijdens mijn onderzoek, alsmede de begeleiding op de juiste momenten heb ik zeer gewaardeerd.

Ook wil ik Bernard Dost en Arie van Wettum bedanken. Zij hebben het NARS-project zoals beschreven in dit proefschrift grotendeels gedragen. Met Bernard met zijn goede humeur is het altijd plezierig samenwerken. De 'zonnige' inzet van Arie van Wettum is nog steeds de spil van NARS.

Verder wil ik de student-assistenten bedanken die geholpen hebben bij de dataverwerking van het project.

Ik dank alle collega's van de afdeling geofysica voor de prettige samenwerking.

I thank Prof. C.H. Chapman for providing me a version of his WKBJ program.

I enjoyed working with Peter Cary in Cambridge, and thank him for his hospitality.

Ik dank mijn ouders voor alles wat zij mij meegegeven hebben.

Ruud, ook in drukke tijden ben je bij me.

The Network of Autonomously Recording Stations (NARS) was financed by AWON, the Earth Science branch of the Netherlands Organization for the Advancement of Pure Research (ZWO). AWON-ZWO also funded a major part of this research.

## *Curriculum Vitae*

De schrijfster van dit proefschrift behaalde in 1976 het diploma Atheneum-B aan de scholengemeenschap St. Montfort te Rotterdam. In dat zelfde jaar werd begonnen met de studie natuurkunde aan de Rijksuniversiteit te Utrecht. Het kandidaatsexamen N3 werd behaalde zij in 1979, en het doctoraal examen geofysica met bijvakken structurele geologie en medische fysica werd in 1983 afgelegd. Sinds 1984 is zij werkzaam als wetenschappelijk assistent bij de afdeling theoretische geofysica aan de Rijksuniversiteit Utrecht.